# OPTICAL COHERENCE MICROSCOPY AND FOCAL MODULATION MICROSCOPY FOR REAL-TIME DEEP TISSUE IMAGING

Liu Linbo
(M. Eng., B. Eng. and B. A, Tianjin University)

A THESIS SUBMITTED FOR THE DEGREE OF DOCTOR OF PHILOSOPHY
GRADUATE RPOGRAMME IN BIOENGINEERING
NATIONAL UNIVERSITY OF SINGAPORE

2008

# Contents

# List of Tables

# List of Figures

# List of Abbreviations

The following is a list of abbreviations in alphabetic order.

2D = two dimensional

3D = three dimensional

4D = four dimensional

BPSF = binary-phase spatial filter

CCD = charge coupled device

CFM = confocal fluorescence microscopy

CM = confocal micrcoscopy

DOF = depth of focus

DRPM = double-reflection parallel mirrors

FD-OCT = Fourier-domain OCT or spectral-domain OCT

FMM = focal modulation microscopy

NA = numerical aperture

NIR = near-infared

OCM = optical coherence microscopy

OCT = optical coherence tomography

PSF = point spread function

RMA = rotary mirror array

SLED = superluminescent light emitting diode

SLM = spatial light modulator

SMF = single-mode fiber

SNR = signal to noise ratio

SS-OCT = swept-source optical coherence tomography

TD-OCT = time-domain optical coherence tomography

TPEFM = two-photon excited fluorescence microscopy

USAF = United State air force

# Acknowledgements

I would like to express my sincere gratitude to my supervisors, Dr. Chen Nanguang, Prof. Dietmar W. Hutmacher, and Prof. Kam W. Leong, for their kind support and help during the cadidature. I am particularly grateful for all the knowledgable instructions and patience provided by my main superviser Dr Chen. I would like to thank Prof. Colin Sheppard for his insightful advice and the knowledge in his publications. I am also grateful to Dr. Huang Zhiwei, Prof. Hanry Yu, Dr. Evelyn Yim for their help.

I also take the opportunity to thank:

Dr. Zheng Wei for her kind help and technical assistance; Dr. Wang Haifeng from Data Storage Institute (A*STAR) for many fruitful discussions; Dr. Liu Cheng and Dr. Wang Lin for many fruitful discussions and valuable suggestions; Dr. Brigitte Loiseaux, Dr. Jean-Pierre Huignard and Mr. Frédéric Diaz from Thales Research & Technologies (France) for their hospitality and help in the pupil filter experiments.

Mr. Wong Chee Howe for his help in dual-mode imaging experiments; Mr. Xu Yingshun for his help in signal conditioning circuits in OCT setup; Mr. Lu Fake and Ms. Shao Xiaozhuo for their assistance in experiments and helpful discussions.

Finally, I would like to thank the rest of my colleagues in the Optical Bioimaging Lab at Division of Bioengineering, National University of Singapore for good interactions.

# Abstract

Visualization of microstructures in intact tissues is the key to understand the biological process *in vitro* and *in vivo*. Imaging technology that has spatial resolution high enough to detect subsurface early-stage tissue abnormalities associated with diseases such as cancer and atherosclerosis is utmost important for pathophysiologic investigation *in vivo* and diagnostic purpose. With the development of three-dimensional (3D) scaffold and tissue culture techniques, there have also been increasing demands for imaging techniques that are capable of performing high-resolution imaging in real-time and at large depths in highly-scattering engineered tissues.

An emerging imaging modality known as optical coherence tomography (OCT) meets these demands well for it is a noninvasive, non-ionizing, high-speed, high resolution, and high sensitivity method. By review of basic and applied research that has been done so far, this thesis identifies fundamental and practical problems with the current OCT technology according to the requirements in the biomedical research and clinical settings. To tackle some of these problems, a few novel methods are developed including double-pass rotary mirror array (RMA), double-reflection parallel mirror array (DRPM), and focus optimization with binary-phase spatial filters. Double-pass RMA based optical delay line was constructed to achieve fast or even real-time imaging in TD-OCT, especially for high-resolution and spectroscopic measurement; DRPM based scanning device enables high-speed or even real-time *en face* scanning OCM; binary-phase spatial filters are designed to overcome the limitation of transverse resolution along a large DOF.

Lack of molecular contrast is one of major drawbacks of OCT for a broad spectrum of biomedical applications. A novel dual-mode microscopy combining optical coherence microscopy and focal modulation microscopy (FMM) is developed as a dedicated instrument for simultaneous and collinear molecular-specific / morphology contrast deep tissue imaging. The OCM subsystem is based on the-state-of-the-art swept source OCT technology which provides a high sensitivity above 100 dB and real-time two-dimensional and fast 3D volumetric imaging; The FMM subsystem is a novel light microscopy (invention of the thesis supervisor) method for deep tissue imaging with single photon excited fluorescence. As a pilot study, the dual-mode microscope has been validated and characterized with animal and engineered tissues labeled with an organic fluorescence dye. Both subsystems provide cellular-level resolution and allow penetration depth of 300 μm in biological tissues.

Although the collinear system is still in its early stage of development, these results demonstrate the possibility of coupling functional and anatomical imaging based on independent contrast mechanisms derived from fluorescence and back-scattered light. Such a dedicated dual-mode microscopy is expected to dramatically enhance the capability of clinicians and biomedical researchers to track biochemical distribution and changes within tissue samples in question.

# Chapter 1 Introduction

## 1.1 Overview

This thesis develops novel methods to address fundamental and practical problems in deep tissue imaging with optical coherence tomography or optical coherence microscopy for biology and medicine. Optical coherence tomography (OCT) is a noninvasive, non-ionizing, high-speed method for imaging the internal micro-structure of biological system and materials. Optical coherence microscopy (OCM) is essentially an OCT technique with the confocal parameter matched to the coherence gate. The ability of measuring nontransparent tissue properties with micrometer spatial resolution and millimeter penetration depth makes it an ideal imaging tool for both biological research and medical diagnosis. Since its introduction in 1990s, numerous basic and applied studies have been done towards the end of successful deep tissue imaging in the laboratory and clinical settings. OCT technology has been evolved with an amazing speed during past 17 years. Advances in solid-state lasers and nonlinear fiber light sources have enabled the development of ultrahigh resolution and spectroscopic OCT techniques that promise to improve tissue differentiation and image contrast. Recent developments in new detection techniques, such as Fourier or spectral domain OCT, swept source OCT (also known as optical frequency domain imaging) and full-field OCT provide very high imaging speed which enables three dimensional imaging. Tissue microstructure can now be visualized and rendered using methods similar to MR imaging, except with micron scale resolution. OCT has been applied clinically for high-resolution, non-contact imaging of structures in the anterior and posterior segments of the eye. Recently, basic and applied studies of

OCT imaging performance in highly scattering tissues led to the investigation of this technology for diagnostic imaging of the skin, vascular tissue, teeth, and oral cavity, as well as the mucosa of the gastrointenstinal (GI), respiratory, and urogenital tracts.

Except for the early success in ophthalmic imaging, the investigation of this technology for research and diagnostic imaging of biological systems and biomaterials is still in the stage of system development and clinical trials. By review of basic and applied research that has been done so far, this thesis identifies fundamental and practical problems with the current OCT technology according to the requirements in the biomedical research and clinical settings. To tackle some of these problems, a few novel methods are developed including double-reflection parallel mirror array (DRPM, invention of the author), focus optimization with binary-phase spatial filters, focal modulation microscopy (FMM, invention of the thesis supervisor) and double-pass rotary mirror array (invention of the thesis supervisor).

According to the objective of the study, we have designed and developed high performance imaging systems based on the above mentioned methods. Experimental results of simple targets and biological tissue models demonstrate superiority of the proposed methods over conventional ones.

## 1.2 Objectives

Develop a high-resolution, bench-top collinear OCM/FMM system for simultaneous molecular-specific and morphological contrast imaging in vitro. A real-time OCM and FMM should be combined into a dedicated instrument. Since the size of cells in the mucusa of luminal organ is typically several microns, the spatial resolution of both microscopes should be less than 1 μm and 3 μm for transverse and axial direction respectively, so that cellular or even sub-cellular structural and functional image can be acquired collinearly and simultaneously. Because many important diseases arise from and exist within superficial tissue layers, for example, epithelial metaplasia, dysplasia and early cancers may be found in luminal organ mucosa, the penetration depth of both microscopes should be up to 500 μm, which should be able to cover all the epithelial layers and most depth of mocusa.

Design and develop a fast scanner for high-speed en face scanning OCM. A simple, high-speed, high-efficiency, high-duty-cycle, path-length maintaining and linear beam scanner should be developed for en face scanning optical coherence microscopes.

Develop a simple technique to achieve super-resolution along an extended DOF for real-time OCT imaging in vivo. The DOF should be extended to a much larger range than the conventional one with improved transverse resolving power. The technique used should be simple and easy to fabricate and miniaturize, meanwhile, the image acquisition speed should not be compromised.

Develop a fast optical delay line for high-speed time-domain OCT, Doppler OCT and spectroscopic OCT. The 3-dB scanning range of the RMA based optical delay line should be 2~3 mm with high scanning linearity, broad bandwidth, and A-line rate of 4~20 kHz.

## 1.3 Background

A signification amount of data collected by cell biologists and tissue engineers relies on invasive imaging techniques such as histology, scanning electron microscopy (SEM) and micro-CT. These invasive methods have many advantages, for example, SEM possesses ideal resolution; however, their intrinsic drawbacks are significant: First of all, these methods preclude the possibility of real-time and dynamic imaging. Since a good many of cell events, for example, intracellular and intercellular signaling, can occur in seconds or even milliseconds [1], the above disadvantage substantially compromises the efficacy of the imaging in such scenarios. Second, invasive imaging requires long and harsh processing steps, so that the viability of the cell/tissue is compromised. The last but not the least, the structural and functional imaging must be done at discrete time points, making structure-function correlation very difficult [2]. As a consequence, despite a tremendous increase in biology and tissue engineering research, real-time cell behaviors inside turbid tissue are poorly understood.

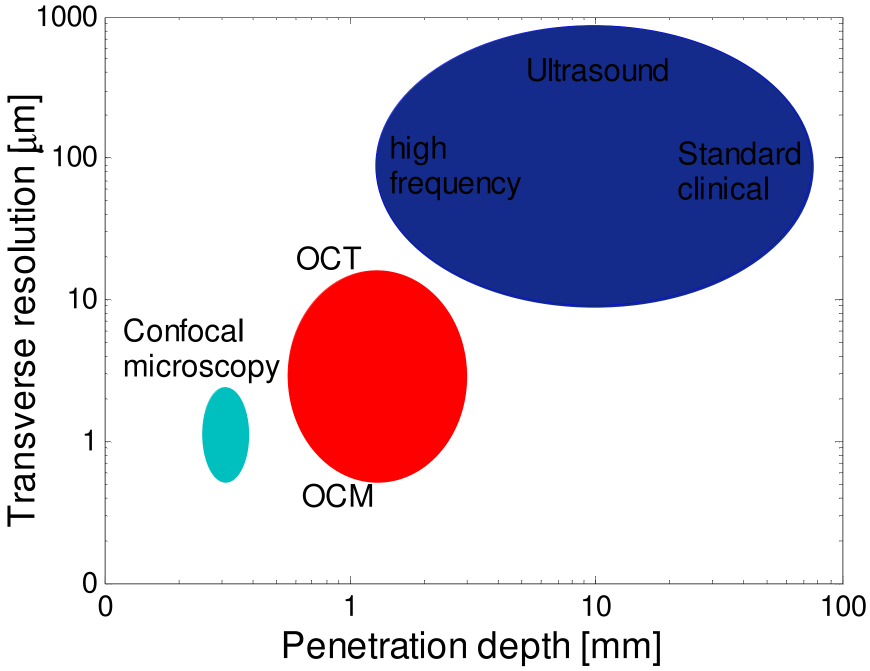

Fig. 1.1 Transverse resolution and image penetration in OCT.

Non-invasive methods such as Ultrasound, computerized tomography (CT), magnetic resonance imaging (MRI) and radiography have all been revolutionized clinical diagnosis; however further success of such methods is mainly limited by their relative low spatial image resolution. Confocal microscopy and multi-photon microscopy have been the most important methods for non-invasive, subsurface imaging in cellular level. Nevertheless, the penetration depth of confocal microscope is limited to a few hundred micrometers in turbid tissue; the penetration depth of multi-photon microscopy can be several hundred micrometers but such a modality necessitates use of expensive laser source, furthermore, multi-photon microscopy relies on nonlinear process of light-mater interaction so that it cannot detect linear properties including important information such as tissue/ cell morphology.

OCT has several apparent advantages over alternative modalities. OCT imaging is non-invasive, non-ionizing, and can be implemented with near video rate image acquisition. Shown in Fig. 2.1, compared with ultrasound imaging resolution is improved by at least an order of magnitude; OCM can dramatically enhance image penetration compared to confocal microscopy alone while significantly improving transverse resolution in OCT to enable cellular level imaging. The potentially small size and low cost of a simple fiber-optic OCT scanner are also important advances. More importantly, the thickness of an engineered tissue normally ranges from tens of microns to several millimeters, which is within the depth range of OCT imaging (2~3 mm); the potential for clinical application of OCT is particularly exciting since many common lesions also occur within the depth range of OCT imaging. OCT may fill this valuable niche in high resolution deep tissue imaging, because of its micrometer-scale spatial resolution in three dimensions and high sensitivity.

### 1.1.1 OCT technology – history and status quo

OCT originates from low-coherence interferometry, which measures echo time delay to achieve high-resolution ranging for characterization of optoelectronic components [3, 4]. Low-coherence interferometry has been applied in the biomedical optics field for the measurement of eye length [5]. OCT was invented by adding lateral scanning to a low-coherence interferometer, allowing depth resolved acquisition of two-dimensional cross-sectional information from the volume of biological material [6]. The concept was initially employed in heterodyne scanning microscopy [7]. The depth resolution in OCT is determined by the coherence length of the source [8]. This is the length over which a process or a wave maintains strict phase relations, and interference takes place only between events that happen within the coherence length [9]; an ideal laser source, for instance, emits light with more than a few kilometres coherence length, while the coherence length of light emitted by a broad-band optical sources can be below 1 μm [10]. OCT technology has been developing with an amazing speed: it takes less than 10 years to evolve from the first generation time-domain technique to the second generation Fourier or spectral domain and swept-source techniques; there have also been a good many of derivatives of OCT technology, including Full-field OCT, Doppler OCT, molecular-contrast OCT (MCOCT), polarization sensitive OCT, and interferometric synthetic aperture microscopy.

### Time domain OCT

The first generation OCT is the time domain OCT (TD-OCT). TD-OCT requires an optical delay line, where a reference mirror is scanned to match the optical path from reflections within the sample. Limited by the scanning speed of the optical delay devices, TD-OCT provides imaging speeds of 4,000–8,000 axial lines per second [11-15]. Normally for a shot-noise limited detection, TD-OCT can reach a maximum sensitivity of

105 dB [16]. TD-OCT was the most popular form of OCT arrangement before Fourier domain or spectral domain OCT.

### Fourier or spectral domain OCT

Fourier or spectral domain OCT (FD-OCT or SD-OCT) is an extension of the concept of “spectral radar” or “coherence radar” [17, 18] and white light interferometry [19] with initial applications in absolute ranging and sensing. This refers to Fourier transformation of the optical spectrum of a low coherence interferometer with a fixed reference mirror and a mismatched optical path-length. In the last 7 years considerable research has been contributed by different groups developing OCT for deep tissue imaging into the FD-OCT method. FD-OCT is attractive because firstly it eliminates the need for depth scanning in time domain OCT, performed usually by mechanical means, and increases the A-line acquisition rate up to ~29 KHz [20, 21]. Recent studies [22-24] have shown that Fourier domain OCT can provide a signal to noise ratio that is more than 20 dB better than the conventional time domain OCT and sufficient sensitivity was demonstrated by displaying video rate images from the retina [20]. FD-OCT has two disadvantages: (i) fast dynamic focusing point by point in depth, which is often utilized in the TD-OCT, is not possible, and therefore the interface optics is devised with a large depth of focus, to accommodate the entire range of the A-scan, usually 2~3 mm; this precludes the possibility of using a high numerical aperture objective to enhance the transverse resolution; (ii) the optical spectrum of the interferometer output consists of symmetric spectral terms, i.e. the same image results for positive and negative optical path-length differences. For the latter, an initial non-zero optical path-length difference is required between the reference mirror and the sample content of interest. This is not possible all the time, especially when imaging moving thick organs or tissue [9]. Different methods have been devised to attenuate the symmetric terms in order to obtain a correct image such as phase-shifting interferometry, or complex signal processing [25]. (iii) The A-line scanning rate is eventually limited by the acquisition speed of available linear CCD, so that Fourier domain OCT is not capable of fast *en face* scanning OCM in which one point scan requires an axial line scan and pixel rate is equal to axial line scan rate in OCT.

### Swept source OCT

Swept-source OCT (SS-OCT, also known as optical frequency-domain imaging OFDI) originates from optical frequency-domain reflectometry (OFDR). OFDR using frequency-swept lasers has been well established for measuring reflections in photonic devices [26-29]. However, it was only recently recognized that Fourier-domain detection using swept lasers dramatically improves sensitivity and imaging speed [22, 23], owing to the recent progress in the fast tunability of laser sources [30-39]. The achievable signal to noise ratio is similar to that of Fourier domain OCT. Swept source OCT suffers from the same disadvantage as Fourier domain OCT except the disadvantage (iii), as the modulation frequency of the interferogram is proportional to the absolute value of the optical path-length difference. Therefore, the optical path-length of the reference mirror must be placed outside the depth range of interest. The time required to tune the wavelength determines the time to produce an A-scan. Currently, tuning speeds of tens of kHz or higher have been achieved, which allows swept source OCT to compete with TD-OCT and FD-OCT in terms of speed. In fact, SS-OCT has much higher capacity in line scanning rate since it employ a single element detector as in TD-OCT, so that with the development of higher speed swept source, SS-OCT has the capacity to perform fast *en face* scanning OCM.

Besides the basic configurations, there have also been a good many of derivatives of OCT technology, which can assume any of the above mentioned basic detection schemes.

### Full-field OCT

Full-field OCT (FF-OCT) obtains *en face* information of a slice of the sample in a single shot, without the need for mechanical scanning. A CCD camera is placed at the output in place of the single detector in TD-OCT. Depth scanning is facilitated by scanning the reference mirror or moving the sample axially in the fashion of conventional TD-OCT. The first FF-OCT system was implemented in a commercial microscope body, using an infrared LED light source [40]. More recently, this technique has been investigated using a thermal halogen light source [41-53]. The use of a thermal light source has a number of advantages, it is inexpensive, has an ultra-broad spectrum and exhibits short spatial coherence (~1 μm); therefore, image speckle is much reduced. This high resolution OCT modality has paved the way for three-dimensional sub-cellular real-time imaging in endoscopic OCT. The drawback is that FF-OCT has a detection sensitivity of around 80 dB with a three-dimensional image aquisition time of 1 s, which is much lower than for conventional TD-OCT.

### Doppler OCT

When the scatterers in the sample tissue move with a constant velocity, there will be Doppler shift in the carrier frequency of the fringe pattern. This change in carrier frequency appears as a frequency bit when the object beam is mixed with the reference beam on the photo-detector in the OCT interferometer. Hence, Doppler OCT can be used to measure or monitor Brownian motion and flows of biological liquids, typically blood flow [54, 55]. In addition to laser anemometry, Doppler OCT provides a depth resolved profile of the flow velocity in the vessel, with the resolution determined by the coherence length of the source. Due to the fact that the scanning itself shifts the frequency of the OCT signal, a challenging avenue in research is to produce the OCT image and velocity map simultaneously [56].

### Molecular contrast OCT

Conventional OCT only detects the morphological information of the sample tissue. To enhance the conventional OCT with molecular-specific contrast, several research groups have implemented various modified OCT schemes that have the capability to detect molecular contrast agents or contrast agents that can potentially bind to a specific chemical or protein. A detailed literature review of molecular-contrast (enhanced) OCT is provided in Chapter 6.

### Polarization sensitive OCT

Polarization sensitive OCT (PS-OCT) detects and quantifies the polarization properties of the tissue by analysing changes in the polarization state of the sample light beam before and after the scattering event. A change in the polarization incurred by light-tissue interaction can be related to a change in the structure, functionality or integrity of the sample tissue. For instance, thermal injury denatures collagen in skin and polarization sensitive OCT can sense changes in the collagen birefringence. Retinal nerve fibre layer, cornea and dentin are birefringent [57]. Since the first report of a functional polarization sensitive OCT system [58], a diversity of polarization sensitive OCT configurations has been investigated. The most complete information about the polarization properties of a biological target is given by systems capable of producing depth resolved Mueller matrix elements [59].

Interferometric synthetic aperture microscopy

Recently, a computational method - interferometic synthetic aperture microscopy (ISAM) is introduced to produce a depth-invariant transverse resolution in interferometric microscopy, especially FD-OCT/OCM, in attempt to overcome the limitation of transverse resolution along a large depth of focus [60-62]. ISAM is essentially an inverse scattering method proposed to produce spatially invariant transverse resolution inside and outside of the focal region by rephasing the scattered signal. ISAM provides a way to extend the axial scanning range of OCM system with a high numerical aperture.

### 1.1.2 Applied research in biomedicine

OCT was initially applied for imaging in ophthalmology [63, 64]. Advantages of OCT technology have made it possible to use OCT in a wide range of biomedical applications. While there are also a couple of applications for study of tissue engineered products and cell biology in tissue models [2, 66-69]. Applications for medical purpose are still dominating [70-72];

Ophthalmologic OCT has been the most successful clinical application of OCT technology. The reasons for that are: (i) the high transmittance of ocular media; (ii) the interferometric sensitivity and precision of OCT which fits quite well the near-optical quality of many ophthalmological structures [73]; (iii) the independence of depth resolution from sample beam aperture which enables high sensitivity layer structure recording at the fundus of the eye [74]. Hence, OCT has already become a routine tool for the investigation in particular, of the posterior part of the eye. Besides, attention has also been drawn to the anterior segment of the eye [75, 76].

Skin is a highly complex tissue with many inhomogeneities. OCT penetration depth covers the *stratum corneum*, the living epidermis containing mainly keratinocytes, and the *dermis* consisting mainly of a network of collagen and elastin fibres and fibroblasts. Most skin diseases can be diagnosed simply by the naked eye or by epiluminescence microscopy, whereas for cancer diagnosis conventional excisional biopsy is still the gold standard. Clinical studies revealed that standard OCT is of value for diagnosis of some inflammatory and bullous skin diseases [77, 78].

Endoscopic and catheter-based procedures are enabling technologies for low-invasive treatments in medicine and, therefore, are growing rapidly. Imaging of the gastrointestinal (GI) tract is a first example for detection of neoplastic changes, where conventional excisional biopsy can have unacceptably high false-negative rates because of sampling error. Gastroenterological OCT has been initiated in 2003 [79], in which it is shown that OCT and OCM can delineate sites like internal histological-level tissue microstructure in bulk GI tissue samples. Gastrointestinal tract OCT imaging in patients [80, 81], validation of diagnostic criteria for Barrett's esophagus [82, 83], and esophageal volume microscopy [84] have been successful implemented. Biliary [85] and intracoronary imaging in patients [86, 87] have also been successful implemented. The following clinical trials demonstrate capability of coronary atherosclerotic plaque diagnosis [88-90] and intracoronary volume microscopy [32].

### 1.1.3 Problems with the current OCT technology

(i). Lack of molecular contrast is another major drawback of OCT for biological research and optical biopsy.

(ii). For endoscopic OCT, limitation of transverse resolution along a large depth of focus (2~3 mm) is the major obstacle to achieve real-time, high-resolution imaging *in vivo*.

(iii). A critical technical challenge for real-time *en face* scanning OCM is identified as low image acquisition rate limited by the speed of the available beam scanning device.

(iv). For OCT implemented in time-domain, a high-speed, ultra-broadband optical delay line is a critical challenge, especially for high-resolution and spectroscopic measurement

## 1.4 Organization and scope of the thesis

This thesis has been mainly supported by two Academic Research Grants from National University of Singapore: real-time optical coherence tomography (R-397-000-024-112) and real-time dual-mode microscopy for tissue engineering *in vitro* (R-397-000-615-712). The later project includes design, instrumentation and applied research of the DRPM based scanning device (Chapter 4) and a dual-mode OCM/FMM system (Chapter 6) for deep tissue imaging *in vitro*. Besides, the work on the former project is also included in this these, which develops novel techniques for *in vivo* imaging. Double-pass RMA based optical delay line was constructed to achieve fast or even real-time imaging in TD-OCT (Chapter 3); binary-phase spatial filters are designed to overcome the limitation of transverse resolution along a large DOF (Chapter 5). In Chapter 2, general theory of OCT is covered; In Chapter 7, further research topics and methods are recommended as important outcome of the study.

# Chapter 2 Theory of OCT

## 2.1 Time-domain method

A system configuration of a typical fiber-based time-domain OCT is show in Fig. 2.1. The system is composed of an interferometer illuminated by a broadband light source, a moving reference mirror, sample arm optics with scanning mirror, and photo-detector with signal conditioning and acquisition electronics. OCT or OCM is essentially the combination of low coherence interferometry and confocal microscope.

### 2.1.1 Low coherence interferometry

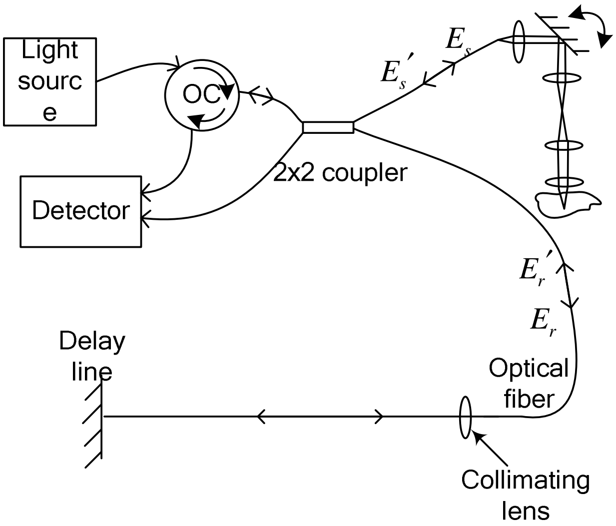

Fig. 2.1 Component blocks of a time-domain OCT system.

In the longitudinal direction, the interferometer in an OCT scanner splits a broadband source field into a reference field $E_r$ and sample field $E_s$. The sample field is focused into a small volume in the tissue. After scattering back from the tissue, the sample field modulated with the sample function $E_s'$ mixes with $E_r$ on the surface of the photodetector. The intensity that impinges on the photodetector is

$$I_d = \left\langle \left| E_d \right|^2 \right\rangle = 0.5\left( I_r + I_s' \right) + \mathrm{Re}\left\{ \left\langle E_r^*\left(t+\tau\right) E_s'\left(t\right) \right\rangle \right\}, \tag{2.1}$$

where $I_r$ and $I_s$ are the DC intensities returning from the reference and sample arms of the interferometer. The second term in this equation, which depends on the optical time delay set by the position of the reference mirror, represents the amplitude of the interference fringes that carry information about the tissue structure. Time-domain A-scans was facilitated by moving the mirror in the reference path of the interferometer, so that the optical path-length of the reflected light in the reference arm is scanned. The interference only occurs when the optical path-length of the sample arm is matched to that of the reference arm (so that light of different wavelength is in phase), thus the interferometer functions as a cross correlator and the amplitude of the interference signal generated after integration on the surface of the detector provides a measure of the cross-correlation amplitude. Meanwhile a carrier (in the form of an oscillating signal) is also generated. Its frequency is the Doppler shift produced by the axial scanner itself [92].

Under the assumption that the tissue behaves as an ideal mirror that leaves the sample beam unaltered, the correlation amplitude depends on the temporal-coherence characteristics of the source, according to [91]

$$\mathrm{Re}\left\{ \left\langle E_r^*\left(t+\tau\right) E_s'\left(t\right) \right\rangle \right\} = \left| G\left(\tau\right) \right| \cos\left[ 2\pi \upsilon_0 \tau + \phi\left(\tau\right) \right], \tag{2.2}$$

Where $c$ is the speed of light, $\upsilon_0 = c / \lambda_0$ is the center frequency of the source, and $G\left(\tau\right)$ is its complex temporal coherence function with argument $\tau$. According to the Wiener–Khinchin theorem, $G\left(\tau\right)$ is related to the power spectral density of the source, as [92]

$$G(\tau)=\int_{0}^{\infty}s(\upsilon)\exp(-j2\pi\tau)d\upsilon. \qquad (2.3)$$

This equation provides important knowledge that sources with broad spectra are desirable because they produce interference patterns of short temporal (and spatial) extent. The half-power bandwidth represents the spectral width of the source in the optical frequency domain. Under Gaussian approximation of spectrum distribution, the corresponding measure of the correlation width is the free-space coherence length of the source, given by [92]

$$l_c=\frac{2c\ln(2)}{\pi}\cdot\frac{1}{\Delta\upsilon}\approx 0.44\frac{\lambda_0^2}{\Delta\lambda}, \qquad (2.4)$$

where $l_c$ is the full-width of the coherence function at half maximum measured in wavelength units. The coherence length basically defines the axial parameter of the coherence gating or axial resolution of low coherence interferometry.

### 2.1.2 Confocal optics in the sample arm

Most of the scanning OCT/OCM systems assume the confocal schematic in the sample arm optics. For example in Fig. 2.1, the fiber tip in the sample arm serves physically as a confocal pinhole which actually creates a confocal volume in the sample space and rejects back-reflected or back-scattered photons from out of focus region [95-98]. This confocal volume basically defined the three dimensional range of an A-line. The transverse spot size of such a confocal volume is defined by the famous Abbé's rule:

$$\Delta x=1.22\frac{\lambda}{2NA}, \qquad (2.5)$$

or a diffraction-limited spot size of $\lambda/2n$NA (FWHM). NA is the numerical aperture of the microscope objective, which is inversely proportional to the lateral resolution. However, the depth of field (FWHM) of such an objective is then given by [99]

$$\Delta z = 1.4\frac{n\lambda}{NA^2}, \tag{2.6}$$

or

$$\Delta z = \frac{\lambda}{4n\left\{1-\left[1-\left(NA/n\right)^2\right]^{1/2}\right\}} \tag{2.7}$$

at full-width at 0.9 maximum [100].

Another notation of depth of focus is Rayleigh range or confocal parameter, which is associated with Gaussian optics and is given by the distance between the two points where the beam width expands to $\sqrt{2}$ times of the beam waist.

From the confocal constraints of the sample arm optics it is found that by increasing the lateral resolution, maximum depth penetration is sacrificed. In the low NA (objective lens) case, the confocal parameter is much larger than the coherence length of the light source, so that one of the apparent advantages of OCT is that the lateral resolution is completely decoupled from the axial resolution. Therefore, the optical design of the system can be optimized for lateral scanning, with no effect on the axial resolution. In the medium or large NA (objective lens) case, the confocal parameter is almost matched to the coherence length of the light source; confocal parameter also has effect on the axial resolution. For example, to obtain a high lateral resolution, say 1 μm at a wavelength λ = 800 nm, requires an objective NA = 0.40; the DOF will be approximately 7μm.

According to the single scattering model [92], the interference signal can be expressed as a convolution, so that the photodetector current can be written as

$$\tilde{i}_d(l_r) \propto \int_0^{\infty} \sqrt{R_s(l_s)h_s(l_s)} \bullet \tilde{R}_{ii}(l_r - l_s)\, dl_s, \tag{2.8}$$

Where $l_r$ and $l_s$ are optical path-length at reference and sample arm respectively;

$R_s(l_s)$ stands for the depth dependent object function;

$h_s(l_s)$ is the axial PSF of sample arm confocal optics;

$\tilde{R}_{ii}(l_r - l_s)$ is the source autocorrelation function, which can be thought of as the axial PSF of the coherence gate. The optical sectioning ability is achieved by exploiting the short temporal coherence of a broadband light source, enables OCT scanners to image microscopic structures in tissue at depths beyond the reach of conventional bright-field and confocal microscopes. The salient feature of the above equation is that the confocal PSF $h_s(l_s)$ multiplies with the object function $R_s(l_s)$, whereas the low coherence interferometric PSF $\tilde{R}_{ii}(l_r - l_s)$ convolves with reflection coefficient profile. Therefore, Axially OCT/OCM is a combination of reflection confocal microscopy with low coherence interferometry, as a result when the confocal gating is matched to the coherence gating, the axial resolution is determined by the joint effect of confocal and coherence gating. However, there is large difference in the section ability between the two gating methods.

The coherence gating mechanism in OCT is much more effective than confocal in picking up the desired signal [94, 95], since only the back-scattered (scattered once) or reflected light, which has a well defined optical pathlength and polarization state, generates the fringe signal for image formation. The improved axial sectioning provided by optical coherence gating permits greater imaging depth and contrast than confocal microscope alone.The difference between the noise rejection ratios is as much as 70dB, It happens that for highly scattering medium, penetration depth of OCT can be 1-2mm while for a confocal microscope this figure is limited to a few hundred micrometers [102].

### 2.1.3 Signal to noise ratio and sensitivity

The noise model for time-domain OCT system has been well established in the previous literatures [102, 103]. The following expressions are from these literatures. Assuming that the light intensity backscattered from the sample is negligible compared with the reference power, for the case of a single detector, the total photocurrent variance or noise is given by [102]

$$\sigma_i^2 = \sigma_{re}^2 + \sigma_{sh}^2 + \sigma_{ex}^2, \tag{2.9}$$

where receiver noise $\sigma_{re}^2$ may be modeled as thermal noise in a resistance-limited receiver, or, for a commercial photoreceiver module, the receiver noise can be obtained directly from the manufacturer's specifications. The random arrival of photons from a monochromatic light source is a Poisson process. The resultant photocurrent variance is shot noise and is given by $\sigma_{sh}^2$ [102]

$$\sigma_{sh}^2 = 2qI_{dc}B, \tag{2.10}$$

where $q$ is the electronic charge, $I_{dc}$ is the mean detector photocurrent, and $B$ is the electronic detection bandwidth. The random arrival of photons from a broadband, incoherent light source is a Bose–Einstein process. The resultant photocurrent variance has two terms: shot noise and excess photon noise. Excess photon noise is given by [102]

$$\sigma_{ex}^2 = \left(1+V^2\right) I_{dc}{}^2 B / \Delta \upsilon, \tag{2.11}$$

where $V$ is the degree of polarization of the source and $\Delta\upsilon$ is the effective linewidth of the source.

If balanced heterodyne detection is used, excess photon noise is largely canceled. When the extra retroreflected power from the sample arm, $P_x$, is taken into account, however, a component of the excess photon noise remains, which is called beat noise [103] and is given by

$$\sigma_{be}^2 = 2\left(1+V^2\right) I_r I_x B / \Delta \upsilon, \tag{2.12}$$

where $I_r = \rho P_r$ *and* $I_x = \rho P_x$. And $\rho$ is the detector responsivity, $P_r$ is the optical power incident upon the photodetector reflected from the reference arm of the interferometer, and $P_x$ is the optical power incident upon the photodetector reflected from the sample arm of the interferometer that is incoherent with the reference light (e.g., spurious reflections from the sample-arm optics). The uncanceled noise in each of the detectors that compose the balanced receiver is independent, so the noise variances add and the total photocurrent variance in the case of balanced heterodyne detection becomes [102]

$$\sigma_i^2 = 2\left(\sigma_{re}^2 + \sigma_{sh}^2 + \sigma_{be}^2\right), \tag{2.13}$$

It should be noted that all photocurrent variances have been written in terms of one-sided noise spectral density functions (i.e., integrated over positive frequencies only) and that, however demodulation is performed, $B$ is the width of the detection band-pass filter as opposed to, for example, the cutoff frequency of a demodulation low-pass filter.

Signal to noise radio is defined as $SNR = \left\langle I_s^2 \right\rangle / \sigma_i^2$. Sensitivity is $S = \sigma_i^2 / \left\langle I_s^2 \right\rangle$. In literature [102], the SNR of the typical single detector system and varies dual-balanced detector systems (refer to Figs. 3.3 (b), 4.2, 5.8 and 6.4) is quantitatively analyzed. It has been demonstrated that dual-balanced detection scheme has a net SNR advantage of several decibels over that of the single detector system. This analysis also indicates the value of low-noise photo-receivers and minimizing back-reflections from the sample arm optics. Some of the possible technical measures that can be made to minimizing back-reflections from the sample arm optics are suggested in Chapter 7.

## 2.2 Fourier-domain method

In time-domain OCT, interference contrast is detected only if the object path length equals the reference path length. Therefore the reference path has to be scanned through the depth range. Fourier domain principles derive from the concept of “coherence radar” or “spectral radar” [104], which avoid scanning the reference through the depth range. These OCT obtain depth information by evaluating the spectrum of the interferogram. The Fourier transformation of the spectrum delivers the depth information. For this type of OCT, there are two approaches. For the basic implementation shown in Fig. 2.2, the interferometer output is spectrally dispersed and the whole spectrum is detected by an array of photodiodes. Shown in Fig. 2.3, the detector in TD-OCT is a single element photo-diode, which normally has response bandwidth over 1GHz.

Whereas those assume FD-OCT configuration require linear CCDs as photodetectors with a typical rate of less than ~100 kHz. In a further modification, the spectrum can be produced by a tunable laser or swept source and then be detected by a single photodiode.

The measuring principle is based on spectral interferometry. The signal from the object consists of many elementary waves emanating from different depths $z$. If the dispersion in the object is neglected, the scattering amplitude of the elementary waves versus depth is $a(z)$. The object signal is superimposed on the plane reference wave $a_R$. At the exit of the interferometer, if one locally separate the different wave numbers $k$ by a spectrometer, the interference signal $I(k)$ is [104]

$$I(k) = S(k)\left| a_R \exp(ikl_r) + \int_0^{\infty} a(z) \times \exp\left\{ i2k\left[ 0.5 l_r + n(z)\cdot z \right] \right\} dz \right|^2 , \quad (2.14)$$

where the path-length in the sample $l_s = l_r + 2n(z)\cdot z$ ; $z_0$ is the offset distance between the reference plane and object surface; $n$ is refractive index; $a_R$ is the amplitude of the reference (for further investigations set $a_R = 1$); $a(z)$ is the backscattering amplitude of the object signal; with regard to the offset $z_0$ , and $a(z)$ is zero for $z<z_0$; and $S(k)$ is spectral intensity distribution of the light source. With these assumptions, the interference signal $I(k)$ can be written as [104]

$$\begin{aligned} I(k) &= S(k)\left| 1 + \int_0^{\infty} a(z) \exp\{ i2knz \} dz \right|^2 \\ &= S(k)\left[ 1 + 2\int_0^{\infty} a(z)\cos(2knz)\, dz + \int_0^{\infty}\int_0^{\infty} a(z)\, a(z') \exp\left[ -i2kn \times (z - z') \right] dz\, dz' \right]. \end{aligned} \quad (2.15)$$

It can be seen that $I(k)$ is the sum of three terms. Besides a constant offset, the second term encodes the depth information of the object. It is a sum of cosine functions, where the amplitude of each cosine is proportional to the scattering amplitude $a(z)$. The depth $z$ of the scattering event is encoded in the frequency $2nz$ of the cosine function. $a(z)$ can be acquired by a Fourier transformation of the interferogram. The third autocorrelation term describes the mutual interference of all elementary waves [104]. The measuring range $\Delta Z$ of the Fourier-domain OCT is limited by the resolution of the spectrometer. [104]

$$\Delta Z = \frac{1}{4n}\frac{\lambda^2}{\delta\lambda}, \tag{2.16}$$

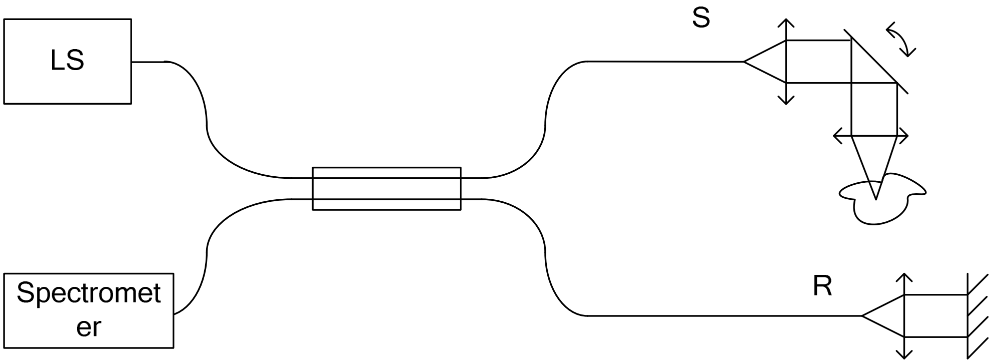

Fig. 2.2. FDOCT setup with reference arm R, light source LS, photodiode PD, sample S and spectrometer.

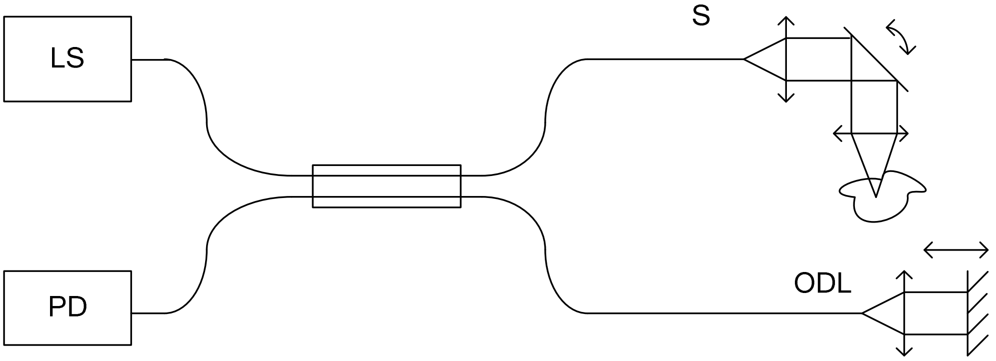

Fig. 2.3. TDOCT setup with Optical Delay Line ODL, light source LS, photodiode PD, sample S and Photodetector PD.

## 2.3 Advantage/disadvantage of Time domain and Fourier-domain method

Fourier domain OCT (FD-OCT) has the following advantages over TD-OCT:

1) Much higher SNR (>30 dB);

The increased SNR in FD-OCT compared with that of TD-OCT is based on the significant reduction of shot noise obtained by replacement of the single-element detector with a multi-element array detector. In a TD-OCT system, each wavelength is uniquely encoded as a frequency, and shot noise has a white-noise characteristic. In a single-detector TD-OCT system the shot noise generated by the power density at one specific wavelength is present at all frequencies and therefore adversely affects the SNR at all other wavelengths [22-24].

2) No moving parts are required to obtain axial scans;

3) Because of 1) and 2), up to ~100X increase in imaging speed.

There are also disadvantages with FD-OCT compared with TD-OCT.

1) The high speed spectrometer required by FD-OCT is practically limited by the avaibilbe spectral resolution, which ultimately limits the ranging depth and/or axial resolution.

The spectral resolution of a high speed, high efficiency spectrometer is practically degraded by the abberration of the camera lens. To achieve theoretical resolution, the camera lens should be corrected for aberration, especially field of curvature, chromatic aberration and astigmation within the field of view. Commercial camera lens are mostly designed for visible light and corrected for a much smaller field of view than high speed line scan CCD used for FD-OCT. Normally, specially designed multi-eliment air spaced camera lens are used, but the performances are not consistant with the theoretical predictions, resulting in reduced bandwidth and spectral resolution, hence, reduced axial resolution and ranging depth [105-106]. The degraded spectral resolution and effective bandwidth will also result in degraded sensitivity in spectroscopic FD-OCT with normally employs a broadband source.

In contrast, TD-OCT is free from these problems since a point detector instead of spectrometer is used. This is why the highest axial resolution ever achieved is produced using TD systems.

2) Compared with TD-OCT, FD-OCT is much slower in doing en face imaging, including *en face* confocal scanning OCT. For FD-OCT to do en face imaging, each point is acquired by Fourier transforming an A-line scan, so the point scan rate is equial to line scan rate in B-mode scanning, which is below 100 kHz, while for TD-OCT to operate in *en face* scanning mode, the pixel rate can be up to tens or even hundreds of MHz (see Chapter 5) using a phase modulator as the delay line.
3) FF-OCT operates in time-domain and FD-OCT can not perform full-field imaging since 2D array of spectrometers is almost impossible.

# Chapter 3 High-speed optical delay line for fast longitudinal scanning

## 3.1 Introduction

Optical coherent tomography permits exceptionally high-resolution subsurface imaging of tissue microstructures. Spectroscopic optical coherence tomography (SOCT) is an extension of conventional OCT, which can reveal the wavelength-dependent backscattering or absorption properties of the intact or stained tissue, so that additional chemical and molecular contrast is provided for functional imaging. In many clinical situations, successful use of OCT and SOCT depends on the design of fast delay lines, which can provide real-time imaging and, therefore, suppression of motion artifacts. A high-performance fast scanning optical delay line is critical for real-time optical coherence tomography implemented in the time domain. Parameters associated with the design of fast delay lines are scanning range, linearity, duty cycle, and cost. Often, compromises among these parameters have to be made.

## 3.2 Literature review

Various designs have been proposed to achieve a scanning repetition rate up to a few thousand A-lines per second and a scanning range of a few millimeters [107-122]. A primitive delay line is a translating mirror, which is driven by a linear motor, an actuator, or a piezoelectric transducer. As the mirror moves back and forth, the power consumption required for generating acceleration increases dramatically with frequency and scanning range. This increase is the reason that most commercially available linear motors and actuators can provide a repetition rate of only ~30 Hz when a 2~3-mm scanning range is required [105]. Although piezoelectric transducers can be driven at much higher frequencies, they can provide only a limited scanning range. Resonant scanners have been demonstrated to achieve a frequency of 1200 Hz and as great as 3-mm optical length difference [106]. The drawback to resonant scanners is that the optical path-length change is a time-dependent sinusoidal function. As a result, the Doppler frequencies of interference signals are depth dependent and vary within a wide range, which may cause difficulties in signal filtering and introduction of more noise. More sophisticated delay lines convert a small-angle rotation into a longitudinal optical path-length change. This conversion can be achieved by use of either a retro-reflector [106] or a combination of gratings and lenses [107, 108]. The former implementation requires a complicated arrangement of mirrors and lenses and precise alignment. The grating-based rapid-scanning optical delay line (RSOD) has been widely used by researchers, and repetition rates of 2000 [107] and 4000 [108] scans have been reported for such delay lines with a galvonometer (driven with a 1-kHz triangle waveform) and a 4-kHz resonant scanner, respectively [100, 104-106]. While its advantages (e.g., independent control over group and phase delays) are well recognized, the dispersive property of the grating may reduce the available bandwidth, and thus limits the axial resolution. A broad bandwidth is not only important for ultra high resolution, but also essential for spectroscopic OCT [118-122]. A rotary mirror array (RMA) was developed in attempt to provide a nearly ideal fast scanning optical delay line. Chen *et* a*l* [113, 123] have demonstrated its superb linearity (>99.9%), millimeter scanning range, and high-speed capability. The dispersion of such a delay line is so trivial that commonly available light sources at 800 nm, 1300 nm, and 1550 nm can be readily connected to it without additional alignment or noticeable differences in performance. This feature makes a RMA highly suitable for real-time spectroscopic OCT. Nonetheless, a drawback with this single-pass design was soon identified which prevented this novel device from successful applications in OCT. The returned light from the RMA-based delay line is subject to strong amplitude modulation. As a result, the effective scanning range is reduced to less than 1 millimeter when 3-dB flatness is required. The amplitude modulation is caused by non-uniform coupling between the optical fiber and the RMA, which will be explained in the following section. In this chapter, a double-pass design is proposed which has achieved more uniform coupling and an extended scanning range (over 3 mm). At the same time, the existing advantages of the RMA are not compromised [124, 125].

## 3.3 Materials and methods

### 3.3.1 Optical design

The structure of RMA has been described in reference [113]. We follow exactly the same geometry in this research. A total number of 36 small mirrors (9 mm by 9 mm) are uniformly deployed along the circular periphery of a rotary base in a discrete rotational symmetry about the axis (Fig. 3.1 (a) (b) and (c)). The effective radius $R$, defined as the distance between the light incident point and the rotation axis, is set to be 50 mm. The reflective facet of each mirror is tilted at a small angle $\alpha$ with respect to the rotary plane and the local mirror translation direction. In the previous single-pass design, an objective lens is used to couple the light between the RMA and an optical fiber. If the mirrors move in a strictly linear fashion (translation), the incoming beam (from the optical fiber) can be collimated into a parallel beam and strikes a mirror at a right angle. Such a configuration would allow the light beam to return to the optical fiber with a uniform intensity, independent of the scanning depth. Unfortunately, this ideal situation is practically impossible: only the local motion of mirrors in a RMA can be approximated as linear; from a global point of view, the mirrors are actually rotating around the axis. The circular motion causes the normal direction of the reflective facet to change constantly. The change in the normal direction as a result of rotation is given by

$$\begin{bmatrix} n'_x \\ n'_y \\ n'_z \end{bmatrix} = \begin{bmatrix} \cos\varphi & -\sin\varphi & 0 \\ \sin\varphi & \cos\varphi & 0 \\ 0 & 0 & 1 \end{bmatrix} \begin{bmatrix} n_x \\ n_y \\ n_z \end{bmatrix}, \tag{3.1}$$

where $\vec{n} = [n_x \quad n_y \quad n_z]^T$ and $\vec{n}' = [n'_x \quad n'_y \quad n'_z]^T$ are normal vectors of a mirror before and after the mirror array is rotated counterclockwise for an angle $\varphi$. The coordinates system is so chosen that the Z axis coincides with the rotation axis. The maximal difference in the normal direction can be estimated with the following equation:

$$\vec{n} - \vec{n}_0 = \begin{bmatrix} -\sin\alpha\cos\Delta \\ -\sin\alpha\sin\Delta \\ \cos\alpha \end{bmatrix} - \begin{bmatrix} -\sin\alpha \\ 0 \\ \cos\alpha \end{bmatrix} \approx \begin{bmatrix} 0 \\ -\sin\alpha\sin\Delta \\ 0 \end{bmatrix}, \tag{3.2}$$

where $\vec{n}_0 = [-\sin\alpha \quad 0 \quad \cos\alpha]^T$ is the normal vector when the incident beam hits the center of a mirror, and $2\Delta = 360^\circ / \textit{number of mirrors}$ is the angular period of the RMA. To minimize the directional variation, it is necessary to reduce the tilting angle $\alpha$ and/or the angular period $2\Delta$. However, smaller angles lead to a smaller scanning range. In our current configuration, $\alpha$=14° and $\Delta$=5°. The corresponding maximal directional variation is about ±1.2°, mainly in the elevation direction.

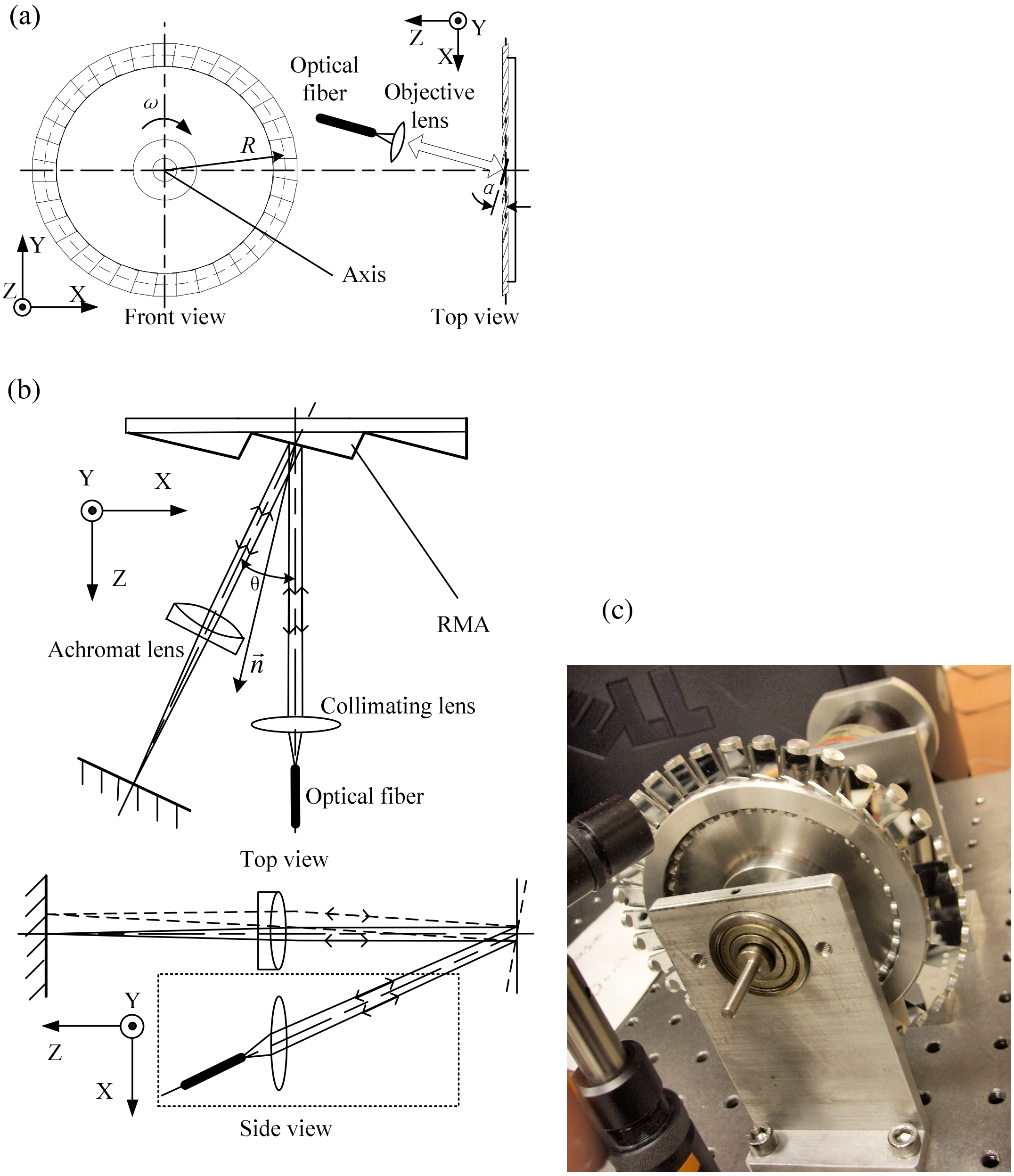

Fig. 3.1 Principle of double-pass RMA: (a) Rotary mirror array and single-pass optical delay line. (b) Double-pass configuration of our delay line. The dashed lines denote a second mirror orientation and the corresponding optical paths. To avoid overlapping, we have displaced the optics in the dotted box. (c) Photo of RMA.

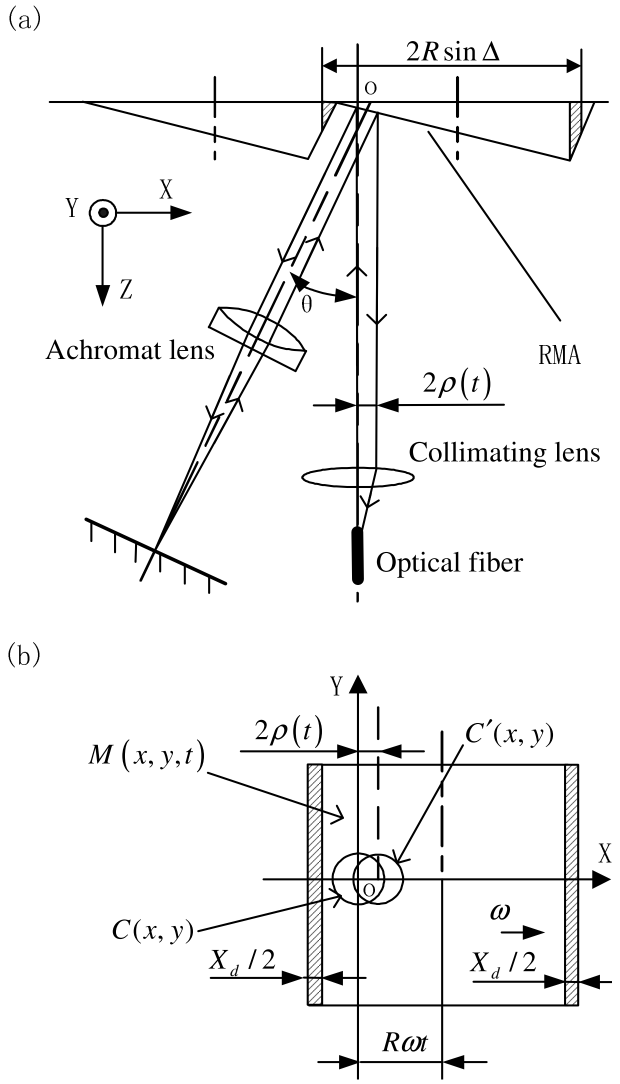

Fig. 3.2 Parallel shift in the double-pass RMA. (a) Parallel shift in the double-pass configuration (For simplicity, a single line denotes a light beam). (b) Parallel shift and mirror edge effect projected on the principle plane of the collimating lens.

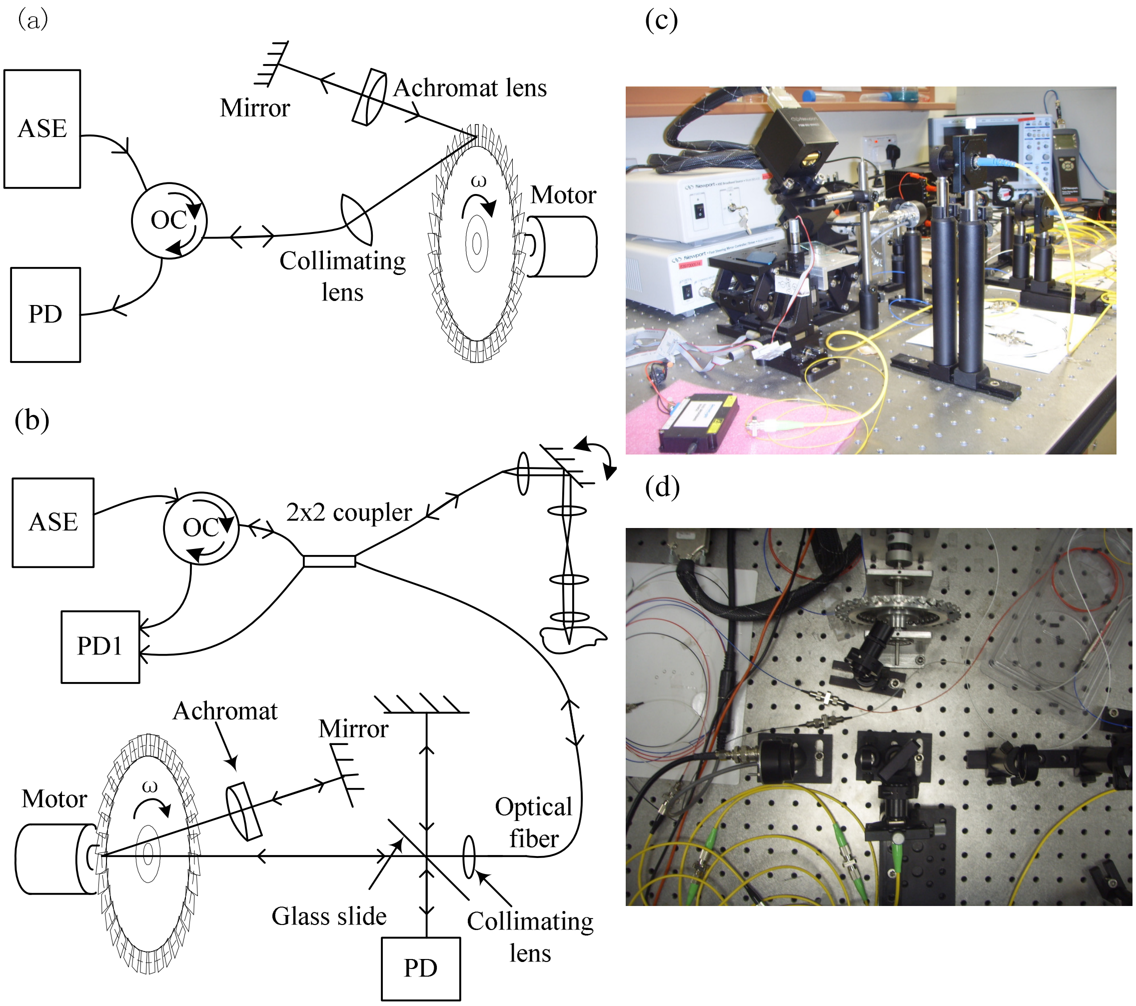

Fig. 3.3 OCT setup with double-pass RMA. (a) Experimental setup for testing of amplitude modulation. (b) The fast OCT system used for imaging experiments. OC: optical circulator; PD: photodetector; PD1: dual-balanced photodetector. (c) Photo of RMA based optical delay line. (d) Photo of sample arm optics.

As one can see, when the collimated light beam is reflected back to the collimating lens, it cannot always be coupled into the optical fiber since the focal point is moving laterally. The typical core diameter of a single mode optical fiber is only 8.2 microns, too small to catch the moving focal point all the time. The solution used previously is to focus the incoming light beam onto the mirror. But the mirror facet is also scanning axially. As a result, the intensity of returned light may fall rapidly when the mirror facet moves away from the focal point. This is one of main sources of amplitude modulation. Another important factor is that the returned light beam may not be captured within the useful aperture of the objective lens since the beam is deflected with a varying angle. These factors pose a serious challenge to optical design. Suffering from amplitude modulation, the effective scanning range (-3 dB) we achieved with the previous single-pass design was less than 1 mm [113].

To address the problem of non-uniform coupling, we have designed and implemented a double-pass RMA. Shown in Fig. 3.1(b), a specially designed retroreflector is included to reflect light back along paths parallel to that of the incident beam. The retroreflector is comprised of an achromat (focal length $f_r = 25\ mm$) and a mirror in the focal plane. The light beam from the optical fiber is collimated, propagates along the direction parallel to the rotation axis, and then it is deflected by the RMA toward the retroreflector. The optical axis of the retroreflector is aligned coincident with the beam from the RMA (at the moment when the incident point on the RMA is located at the center of a mirror). The distance between the RMA and the achromat is roughly identical to the focal length of the achromat. With such an arrangement, the returned beam from the retroreflector actually follows a path very close to that of the incoming light beam, regardless of the normal direction of the RMA (see the side view in Fig. 3.1(b)). Besides the reduced amplitude modulation, the maximal scanning range is nearly doubled. In each duty cycle, the one-way optical path length can be expressed as a function of time $t$ with the origin at the moment when the incident beam illuminates the center of the mirror:

$$\Delta l(t) = R(1+\cos\theta)\tan\alpha\sin(\omega t), \tag{3.3}$$

where $\theta$ is the angle between the optical axes of the RMA and retroreflector.

There are two major factors that determine the amplitude modulation: parallel shifting of the returned beam and the edge effect of the mirror. As shown in Fig. 3.2, the incident collimated beam (enclosed in the circle $C(x,y)$) is always centered at $(x, y) = (0, 0)$ and the intensity follows a Gaussian distribution:

$$I(x,y) = \frac{1}{2\pi\sigma^2} e^{-\left(x^2+y^2\right)/2\sigma^2}, \tag{3.4}$$

where $\sigma$ is the standard deviation. The reflected beam from the retroreflector (enclosed in the circle $C'(x,y)$ )) is centered at $(x,y) = \left(-2\rho(t), 0\right)$. The parallel shifting of the symmetric center line is given by

$$\rho(t) = R\sin\theta\tan\alpha\sin(\omega t). \tag{3.5}$$

In Fig. 3.2 (b), the shaded regions denote discontinuity between two consecutive mirrors on the RMA. Accordingly, the mirror aperture function is given by

$$M(x,y,t) = \begin{cases} 1 & |x-\omega t| < R\Delta - X_d/2 \\ 0 & elsewhere \end{cases}, \tag{3.6}$$

where $X_d = 4R\Delta\sin^2\alpha$ is the width of the discontinuous region. Taking these factors into account, the normalized amplitude as a function of time is given by

$$U(t)=\int_{-\infty}^{+\infty}\int_{-\infty}^{+\infty} I(x,y)\times M\left(x,y,t\right)\times C(x',y')dxdy, \tag{3.7}$$

where the circular fiber aperture

$$C\left(x,y\right)=\begin{cases}1 & x^2+y^2\le r^2\\ 0 & elsewhere\end{cases} \tag{3.8}$$

is defined by the beam radius $r\approx NA\times f$ (single mode optical fiber $NA=0.14$ measured at 1% power level, the focal length of the collimating lens $f=7.5mm$). (x, y) is the coordinates of an incident ray while ($x'=-x-2\rho(t),\ y'=y$) is the coordinates of the corresponding returned ray. The intensity profile $I(x,y)$ is defined by the standard deviation $\sigma\approx r/3.035$. To minimize the mirror edge effect, the beam size should be as small as possible. However, a smaller beam size is accompanied by a smaller circular fiber aperture $C(x,y)$, which results in a lower coupling efficiency of returned rays into the optical fiber due to parallel shifting. Consequently, the optical beam size is a compromise between both limiting factors.

It is worth mentioning that there is always variation of certain degree in positioning of the 36 mirrors, which causes mirror to mirror fluctuation in the returned light. As shown in Fig. 3.3 (b), we incorporate an additional Michelson interferometer in the reference arm, where a photodetector detects the interference signals for timing purpose and pathlength calibration, so that the geometric error can be cancelled out via simple signal processing.

### 3.3.2 Testing setup

Our new double-pass design has been evaluated experimentally in terms of amplitude modulation and linearity. Shown in Fig. 3.3 (a) is the setup to measure the returned light intensity as a function of optical pathlength. The RMA is directly driven by a Maxon DC motor (150 W, 40 mm diameter) with a continuous speed up to 6900 rpm (revolution per minute). The maximal repetition rate for axial scanning is around 4000 Hz. An optical circulator (PIOC15P2122, AC Photonics Inc.) with a typical insertion loss of 0.88-dB conveys light to and from the delay line, and an ASE light source (BBS-430, Newport) is used to provide 13-dBm broadband light in the 1525-1605 nm wavelength range. The output from the light source (attenuated appropriately) is conveyed by the circulator to the double-pass RMA and the returned light is directed to an adjustable photodetector (2117-FC, New Focus), which converts light power to voltage. When the RMA is rotating at a constant speed, the periodic output signal from the photodetector is registered by a Lecroy digital oscilloscope or a PCI data acquisition card (not shown in the Fig. 3.3 (a)).

### 3.3.3 In-house OCT/OCM setup

Our double-pass RMA has been incorporated in a fast OCT system (Fig. 3.3(b) (c) and (d)) for imaging experiments. An ASE light source (BBS-430, Newport) is used to provide 13-dBm broadband light in the 1525-1605 nm wavelength range. The output of the light source is split by a 50:50 fiber coupler pigtailed with FC/UPC connector into separate paths for the reference and sample arm. An optical circulator (PIOC15A2122, AC Photonics Inc.) conveys light to and from a double-pass optical delay line based on rotary mirror array (RMA), which provides over 3-mm depth scanning range in air. With an A-line repetition rate set at 4 KHz, the B-scan frame rate is 15 Hz with 256 A-lines per frame. In the sample arm the optical beam is collimated by a near-IR achromat and goes into a dual-axis fast steering mirror (FSM-300, Newport) which allows two dimensional x-y *en face* scanning. The beam is relayed to the objective lens by a pair of identical near-IR achromat lenses.

We have two achromats of different focal length used as the objective lens. With a focal length of 50 mm, the effective numerical aperture is set to be 0.05, so that the theoretical transverse resolution is 15 μm and the depth of focus is up to 3 mm. In this case, the setup normally works in the cross-sectional imaging mode, which a typical OCT assumes. With a focal length of 7.5 mm, the effective numerical aperture is set to be 0.3, so that the theoretical transverse resolution is 2.3 μm and the depth of focus is about 60 μm. In this case, the setup can work in the *en face* scanning mode; therefore, it is essentially an optical coherence microscope (OCM). The backscattered is coupled to the fiber by a near-IR achromat. The light from the sample and reference are recombined the coupler and the interference signal is directed to a dual-balanced photodetector (2117-FC, New Focus). Due to the high speed of RMA, the interference signal is modulated with a carrier frequency up to several mega hertz. The voltage signals from two detectors are demodulated with mixers (ZFM-3, Mini-circuits) and a function generator. The demodulated signals are digitized with a dual-channel, 12-Bit, 10 MS/s/ch, Simultaneous-Sampling Multifunction DAQ (NI PCI-6115).

### 3.3.4 Engineered tissue and in vivo imaging

The in-house OCT/OCM system is used to image biological / engineered tissue samples to verify the performances of the optical delay line and the whole time-domain system. PLGA (poly (lactic-co-glycolic acid)) scaffold was obtained from the Tissue

Repair Lab at Division of Bioengineering, NUS. Engineered tissue pellets for *in vitro* human embryonic stem cell expansion was provided by Prof. Kam. W. Leong's Lab at Division of Biomedical Sciences, Johns Hopkins in Singapore. The *in vivo* imaging on human skin was done using the author's finger tip.

## 3.4 Results

### 3.4.1 Optical delay line (RMA)

Plotted in Fig. 3.4 is a segment of acquired waveform corresponding to the returned light intensity as a function of time. During each period, the optical pathlength increases (or decreases, depending on the rotation direction) almost linearly with time. Therefore, the waveform also represents the dependence of the returned light intensity on the optical pathlength. The light intensity is fairly constant except the narrow dips.

Scanning range vs. Flatness

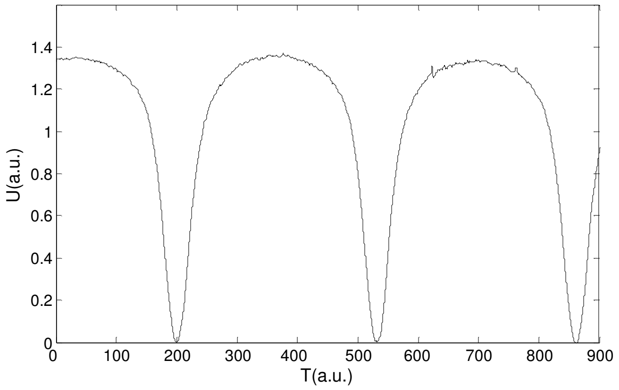

Fig. 3.4 Waveform acquired from our delay line.

The available flatness, defined as the maximal difference in the returned light intensity, is associated with the scanning range and duty factor (Table 1.1). A scanning range of 3.43-mm can be achieved when a 3-dB flatness is required. Eqs. (4)-(8) provide theoretical modeling of amplitude modulation, which depends on RMA dimensions and the collimator focal length. Shown in Fig. 3.5 (a), our experimentally acquired waveform is in good agreement with the theoretical prediction. The dependence of coupling uniformity on collimator focal length is numerically characterized in Fig. 3.5 (b), which suggests a collimator focal length around 6.5 mm for the least amplitude modulation.

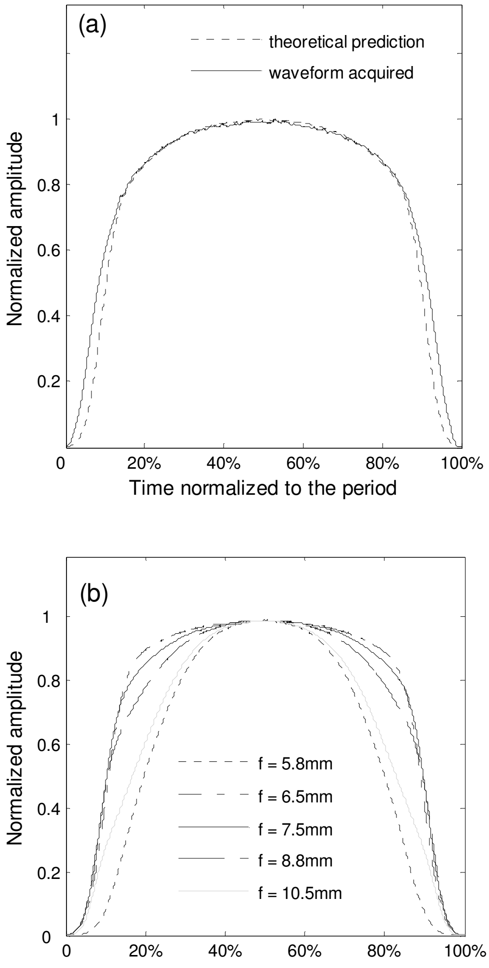

Fig. 3.5 reference arm reflectivity profiles. (a) Expected normalized beam amplitude versus acquired waveform as a function of time. (b) Fiber-optical coupling efficiency with different beam diameters (collimator focal length).

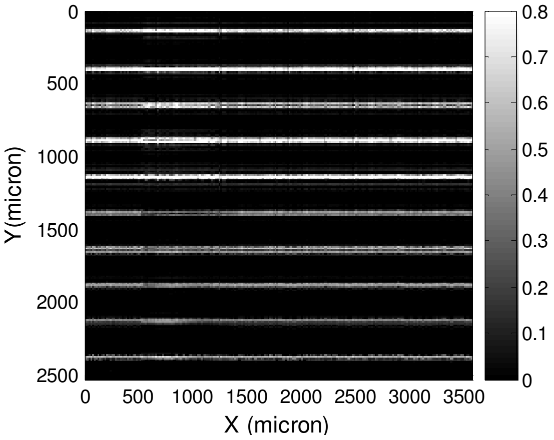

Fig. 3.6 Cross-sectional image of the glass cover slips.

Table 1.1. The flatness and corresponding scanning range.

| Flatness | Duty cycle | Scanning range |
|---|---|---|
| 1-dB | 71% | 2.91-mm |
| 2-dB | 80% | 3.26-mm |
| 3-dB | 84% | 3.43-mm |

Table 1.2. The actual axial position of a mirror surface and corresponding measured interferometric values.

| Axial position $(\mu m)$ | 507.6 | 1507.6 | 1557.6 | 1607.6 | 1657.6 | 1807.6 | 2307.6 | 2357.6 | 2407.6 | 2457.6 |
|---|---|---|---|---|---|---|---|---|---|---|
| Measured value $(\mu m)$ | 507.6 | 1505.1 | 1544.4 | 1604.1 | 1653.3 | 1808.7 | 2310.6 | 2359.5 | 2410.7 | 2457.5 |

### 3.4.2 In-house OCT/OCM

Transverse resolution

Using the achromat with 7.5 mm focal length as the objective, the calculated transverse resolution was about 2.5 μm. Shown in Fig. 3.7 (a) and (b), the element 4 in the group 7 of a USAF resolution target could be resolved and the measured value was less than 2.7 μm.

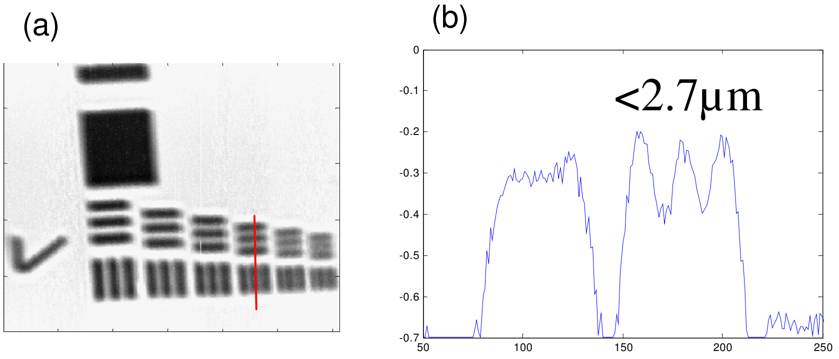

Fig. 3.7 Resolution measurements of the OCM system. (a) resolution chart (US air force resolution target) bar periods of better than 5.4 mm can be resolved (red line); (b) The radius of the focal spot is 2.7 µm.

### Axial resolution

For an OCT system with a low numerical aperture of the objective lens, the axial resolution is solely defined by the coherence length of the light source. Fig. 3.8 (a) shows interference fringes acquired with a planar object, which is essentially the axial point spread function of the setup. The measured resolution is 17.8 µm in air and 12.9 µm in tissue. Together with a transverse resolution of 2~15 µm, tissue microstructure in the histopathology level could be retrieved using this setup.

### Signal to noise ratio

We use an empirical method to measure the SNR of the setup. In the first measurement, we used a glass slide with a refractive index of 0.04 as the sample, and acquired the signal; in the second measurement, no sample was used so that we can get the "signal" of the noise. The SNR is calculated as ratio between the root mean square (rms) of signal and noise:

$$\mathrm{SNR} = 20 \log \left(\mathrm{Signal}_{\mathrm{rms}} \times 25 / \mathrm{Noise}_{\mathrm{rms}}\right) \tag{3.9}$$

As shown in Fig. 3.8 (b), the measured SNR is 96 dB, which is slightly below the optical value of >105 dB. Several factors contribute to the high noise floor of the system: first of all, the light reflected by the fiber tip at the fiber-air interface significantly elevates the noise floor due to the FC/UPC pigtail; Secondly, the build-in amplifier of the photodetector has limited gain-bandwidth product (GBP) and filter performances, so that the noise can not be effectively suppressed resulting in aliasing noise after digitization.

Frame rate

With an A-line repetition rate set at 4 KHz, the B-scan (cross-sectional) frame rate can be up to 15 Hz with 256 A-lines per frame. However, to maintain a penetration depth of around 1 mm in highly scattering medium, for example human skin, the frame rate was set to 2 Hz. When the setup was working in the *en face* scanning mode, the imaging speed was ~3 minute per frame with 512×512 pixels.

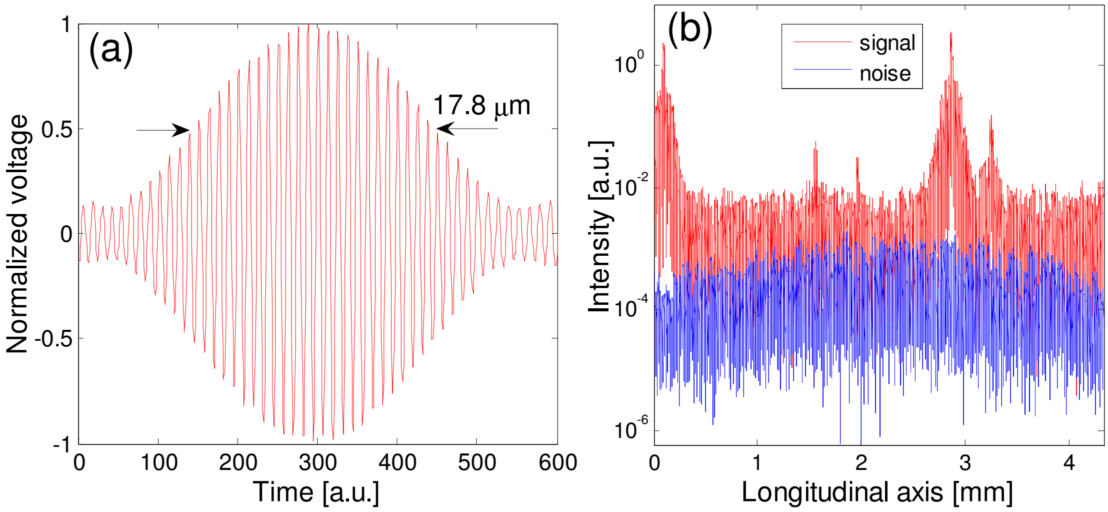

Fig. 3.8 (a) axial point spread function; (b) Signal to noise ratio.

### 3.4.3 Engineered tissue and in vivo imaging

PLGA scaffold

Show in Fig. 3.9, both images demonstrate a penetration depth of less than 500 µm due to highly scattering and/or absorbing properties of the PLGA scaffold.

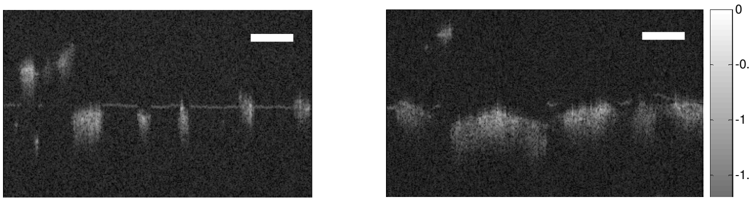

Fig. 3.9 Cross-sectional images of PLGA (poly (lactic-co-glycolic acid)) scaffold. Scale bar 500µm.

## Engineered tissue pellet for the human embryonic stem cell expansion

Fig. 3.10 shows the cross-sectional images of an engineered tissue pellet for the human embryonic stem cell expansion. Four cross-sectional images of the pellet were obtained with transverse interval of 20 µm. Since collagen fibers and extra-cellular matrix have much higher refractive index than the cytoplasma and culturing medium, the area with higher gray levels might indicates collegen fibers and matrix in the image plane. The full cross-section of the pellet was retrieved demonstrating a penetration depth greater than 1 mm for such an engineered tissue.

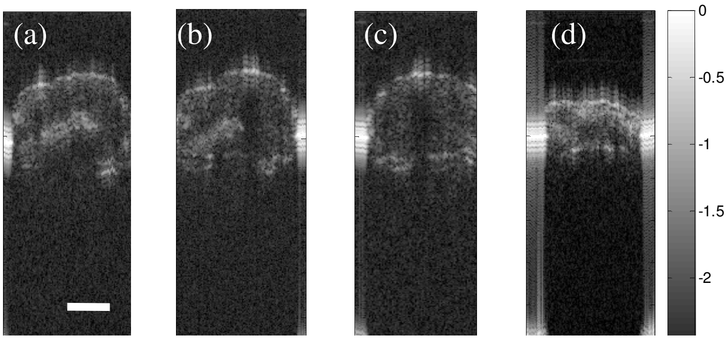

Fig. 3.10 Images of an engineered human ES cell tissue pellet obtained at cross-sections with interval of 20 µm (a) (b) (c). Cross-sectional images of the same engineered tissue pellet obtained 100 µm from (b) (d). Scale bar 300 µm.

## Human skin *in vivo*

Shown in Fig. 3.11, a cross-sectional image of human skin *in vivo* is demonstrated with a penetration depth of around 0.7 mm. A sweat gland is indicated by an arrow. To facilitate better visualization, the gray scale is inversed.

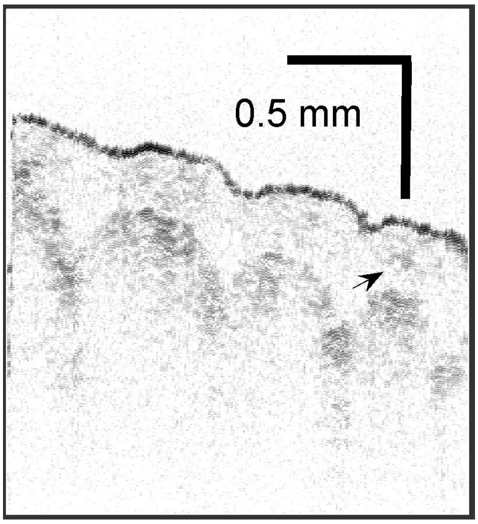

Fig. 3.11 Cross-sectional image of human skin in vivo. Gray scale is inversed.

## 3.5 Discussions and conclusion

For the double-pass RMA based delay line, there is still room for further improvement in terms of flatness. By the use of an objective lens (as the collimator) of shorter focal length (higher magnification), the beam diameter can be reduced. The parallel shifting problem can be alleviated by decreasing the angle $\theta$. Of course, this could add some difficulties to components deployment and optical alignment. Nonetheless, a scanning range over 3 mm should be enough for most applications. An even longer range is available by simply enlarging the overall size of RMA. While the repetition rate of the current setup is bounded to 4000 Hz by the dc motor, it is not difficulty to achieve a much higher rate with high-speed motors or turbines. But practically, a few kilohertz is usually adequate for real-time image acquisition.

Although RMA provides a scanning range of more than 3 mm in air, due to highly scattering property of many biomedical specimens like above mentioned scaffold and human skin, the practical probing depth is limited within 1 mm or even shorter. The penetration depth is dependent mainly on the scattering and absorbing coefficient of the tissue, and basically limited by the available sensitivity of the imaging system. For example, one can expect a penetration depth more than 3 mm in tissue when one is imaging an African frog due to semi-transparence of the body. If one changes the sample to human skin, the practical probing depth is limited within 1 mm. The scattering coefficient of some biomedical tissues has been listed in Chapter 1.

As mentioned in Chapter 2, the second generation OCT technologies (Fourier-domain OCT and swept-source OCT) provide much better sensitivity than the first generation one (time domain OCT), so that the penetration depth can be improved significantly. Due to the advantages in sensitivity and axial scanning speed, the second generation OCT technology is almost dominant in all the biomedical applications since its invention, except for optical coherence microscopy working in the *en face* fast scanning mode.

In a time-domain OCT system, the longitudinal scanning is usually performed by a moving mirror in the reference arm. While in a FD-OCT, the longitudinal scanning is achieved by Fourier transform of spectral interference signal acquired using a spectrometer or equivalent instruments. Mechanical scanning of reference mirror is avoided in the FD-OCT. Since the interference signal of the whole spectra is acquired simultaneously. Therefore, the longitudinal scanning in FDOCT is much faster than that in TDOCT when both setups are working in cross-sectional scanning mode. The linear CCD commonly used as the photo-detector in FDOCT systems allows maximum line acquisition speed of ~100 kHz, which is enough for the line rate requirement in real-time cross-sectional scanning mode. However, in the *en face* scanning mode, a transverse point scan is actually an axial line scan, so that a typical line scan rate of a few mega hertz is required for a frame rate of several Hz. In this case, the TD-OCT is superior in axial line acquisition speed over FD-OCT, since in TD-OCT one can use a phase modulator with modulation frequency from DC to several Giga Hertz for longitudinal scanning. In Chapter 4, FDOCT is combined with high performance sample arm optics for the cross-sectional imaging; while in Chapter 5, the time-domain schematic is adopted to achieve a fast *en face* scanning OCM

To conclude, we have developed the double-pass RMA by including a specially designed retro-reflector and an interferometer in the optical path. The novel design presented solved the last crucial problem keeping RMA from practical use in an OCT system. A sufficient scanning range (greater than 3 mm) for OCT has been achieved with uniform optical coupling and high delay repeatability. Inheriting the original advantages such as high linearity, high repetition rate, constant scanning speed, and minimal dispersion, the double-pass RMA has become nearly ideal as a fast scanning optical delay line.

# Chapter 4 Ultra-fast transverse beam scanner

## 4.1 Introduction

Laser scanning microscopy

Confocal microscopy, multi-photon microscopy and interference micrcoscopy (including but not limited to optical coherence microscopy) are powerful tools that can provide subsurface high-resolution imaging of samples (including but not limited to biomedical samples). Confocal microscope can achieve a sub-micron resolution and a penetration depth up to a few hundred micrometers. Optical coherence microscope and multi-photon microscope have comparable spatial resolution with confocal microscopy, but the penetration depth can be one to two millimeters. All above mentioned microscopic techniques, however, share the same fundamental attribute: they are scanning microscopes. The main drawback of scanning is that image acquisition is not as rapid as wide field techniques in which the entire image is acquired simultaneously [126]. In many potential biomedical applications, the data acquisition speed is a critical issue in suppressing motion artifacts and acquiring high resolution four dimensional images (three spatial dimensions and one temporal dimension).

A fast beam scanner is utmost necessary for high-speed, high-resolution laser scanning microscopic imaging methods. Three dimensional scanning can be implemented in either transverse priority fashion or axial priority fashion. Most of the current fast scanning schemes assume transverse priority fashion, in which angular scanning of collimated beam is transformed into transerve scanning of focus in a sample so that *en face* images of the sample can be obtained. Generally, parameters that determine the performance of a fast beam scanner are scanning range, line rate, scanning efficiency and linearity; for interference microscopy, ability to preserve optical path-length is critical; for microscopic methods that involve photons of different wavelengths, such as fluorescence microscopy, incoherence microscopy and low coherence microscopy, the dispersive characteristic must be considered; Besides, the cost of the scanner and system complexity, although not critical, are important practical considerations in many applications.

*En face* scanning OCM

High-speed optical coherence microscopy has important applications in modern biology and medicine [127, 73]. The *en face* scanning modality used in this study contrasts with that used B-mode imaging where the longitudinal scanning is achieved by use of an optical delay line or Fourier transform of spectral interference fringes. OCM scans an *en face* plane with the coherence gate matched to the confocal gate, so that it does not suffer from depth-of-field limitations present in standard depth-scanning OCT [128-130]. Another important advantage is that it can be combined with other imaging modalities, for instance multi-photon microscopy, to achieve simultaneous functional and morphological deep tissue imaging. A high-speed path-length maintaining beam scanner is critical for successful application of such a microscope in biology and medicine.

## 4.2 Literature review

For the purpose of increasing image acquisition speed in scanning microscopy techniques, parallelized multi-foci schemes are introduced, and have been used to achieve video rate confocal and two-photon microscopy [131, 132]. Because the scanning is accomplished with an array of foci rather than with a single beam, the image acquisition time is cut down by the number of foci applied. One example of parallelized multi-foci scheme is Nipkow disc based scanner, in which an array of pinholes on a rotating disk splits the laser beam into beamlets, producing an array of diffraction limited foci in the sample. However the light throughput is low and therefore not energy efficient. More importantly, like all other parallel excitation microscopy, Nipkow disc based microscopes also suffers from crosstalk between adjacent foci, and axial section ability is compromised [132]. Parallelized multi-foci schemes cannot readily achieve real-time, high quality image at reasonable system complexity.

A widely used laser scanner is galvanometer based steering mirrors. This system typically consists of two synchronized steering mirrors that move in tandem to produce an x-y (transverse coordinates) raster scanning pattern. Galvanometer based beam scanners provide variable scan velocity, good linearity and good position control. However, such a scanner suffers a trade-off between the scanning bandwidth and scanning linearity, and the scanning bandwidth is limited to 1 kHz in close-loop operation mode resulting in a frame rate of 4 Hz with 250 lines per image [133]. In consequence, such a scanner can hardly perform real-time or video rate imaging in a scanning microscope. When a galvanometer based scanner is working in resonant mode, the repetition rate can be up to 7~8 kHz, nevertheless, the scanning angular is a sinusoidal function of time therefore it provides a low efficiency or duty cycle, defined as the ratio of the period of active scanning to the total period; in addition, it may also cause difficulties in signal filtering and introduction of more noise..

The polygon mirror system has been used to implement video-rate confocal microscopy and two photon microscopy to image human tissue *in vivo* [134, 135]; Rotation polygonal mirror systems have the potential to generate line rate up to 10~30 kHz which has been documented in [136]. Rotation polygonal mirror systems have limitations: first of all, the optical path-length is modulated throughout the whole scan cycle, as a result, this scanning means can hardly be used in interference microscopy, such as optical coherence microscopy, coherence probe microscopy, focal modulation microscopy and confocal interference microscopy; secondly, the scanning efficiency, which is inversely proportional to the line scan rate and beam width, is usually limited to fairly modest values since a high efficiency implies a large size of rotor and this is impractical. The limitation in efficiency of such scan rotors is due to the movement of the rotor facets passes the incident beam which is stationary in the direction of rotor movement. During the active scan period the whole of the incident beam must be reflected by the scan rotor facet, so that the width of each facet must be greater than that of the beam by the amount dependent on the desired scan efficiency. Thirdly, parallelism error exists between the rotary shaft and deflection surface of the mirror facet, this is due to the fact that the rotation axis is not in the plane of reflective facet, so that reflection point (intersection point of incident beam axis and the mirror surface) also scans along the incident beam axis, such errors cause the scanning beam to be displaced perpendicular to its defection direction. This additional beam scan is neither linear nor on-axis and will definitely compromise the scanning linearity and accuracy; in addition, it may also cause difficulties in signal filtering and introduction of more noise.

More recently, various rotation double-reflection scanners are design to overcome some of the above mentioned limitations. One example for overcoming the second limitation has been described in a U.S. Patent [137], in which a focused beam instead of a collimated beam impinges onto the facet of the rotation mirror array and a high scanning efficiency is retained. One example for overcoming the third limitation has been disclosed in another U.S. Patent [138], in which a pair of identical polygon mirrors arrays with the same parallelism error is disposed at conjugation planes of a relay lens. When the mirror arrays are rotating synchronously, the parallelism error of two mirror facets are cancelled out. One example for avoiding rotation wobble has been documented in a U.S. Patent [139]. However, each of the above mentioned rotation double-reflection scanners has the disadvantage of increased system complexity, and cannot solve all the problems in one design, especially the problem of optical path-length modulation.

Another fast rotation scanner that performs axial priority scanning has been introduced in [140, 141], in which high speed and linear axial priority scanning can be implemented for real-time confocal microscope and time domain optical coherence microscope. However, the scanning duty cycle is inversely proportional to the scanning range achieved, so that the scanning efficiency is compromised. In addition, such a design necessitate optical path length modulation, so that this scanning means cannot be applied in Fourier domain optical coherence microscopy, which has superiority in terms of sensitivity and image acquisition speed over time domain optical coherence microscopy.

For non-mechanical scanner, acoustic-optical scanners have also been used for beam diffraction. Acoustic scanners have the advantage that arbitrary scanning patterns can be generated. But the dispersive property of the chirped gratings precludes its application in multi-chromatic imaging methods, such as optical coherence microscopy, fluorescence microscopy and nonlinear microscopy.

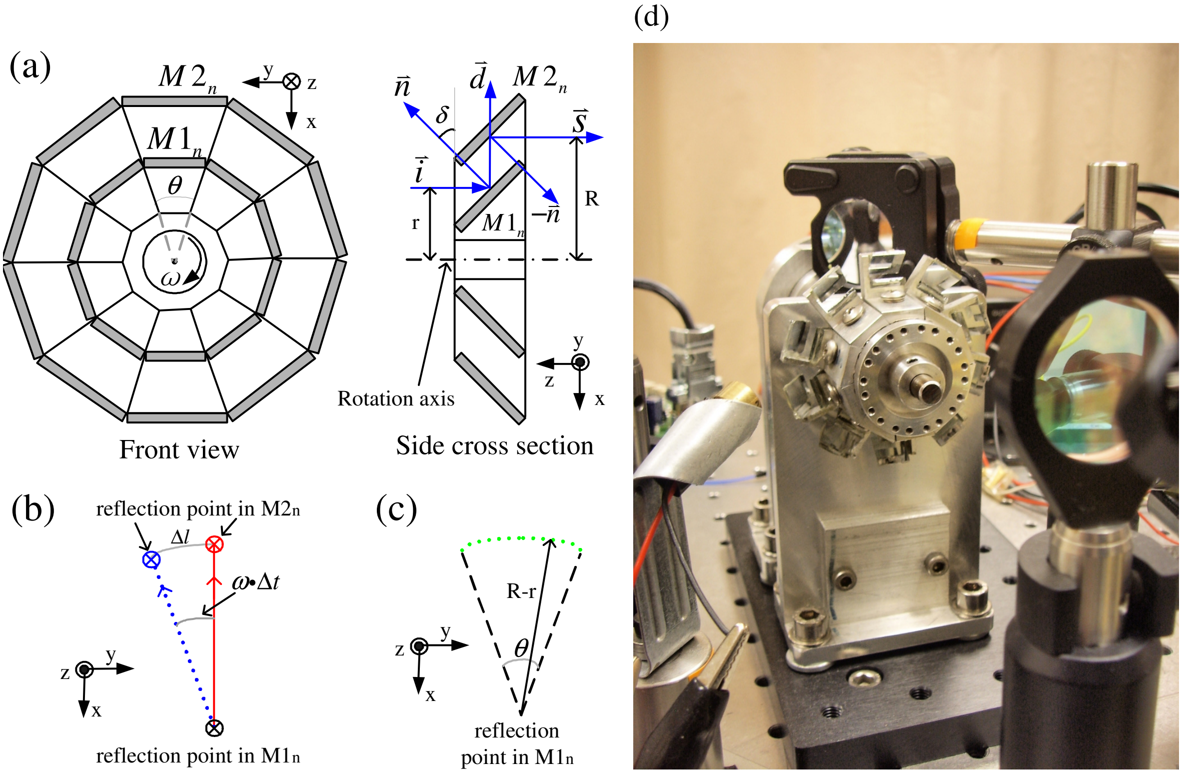

Fig. 4.1 Double-reflection parallel mirror based scanner. (a) Structure of the DRPM. (b) Transverse sketch of the beam scanning. The lower cross (black): incident beam; the upper-right cross (red): doubly reflected beam when t = 0; the upper-left cross (blue): doubly reflected beam when $t = \Delta t$. (c) The trace of beam scanning (dotted green curve) in the front principal plane of the tube lens. (d) Photo of the device.

A number of features, which are necessary for enhanced utilization of these techniques commercially in medical and other applications include the following: ability to linearly scan the focus inside a sample in the range of several hundred micrometers;

high scanning speeds without sacrificing quality; dispersion free operation; path-length modulation free operation; easy to align; high duty factors or efficiency; robust to provide long lifetimes; and have a structure that is easy to fabricate and inexpensive compared to alternatives.

## 4.3 Materials and Methods

### 4.3.1 Optical and mechanical design

In this Chapter we present a novel scanner design based on a double-reflection polygon mirror (DRPM) that is path-length maintaining, and has high duty cycle and fast or even real-time *en face* scanning capacity [142, 143].

Shown in Fig. 4.1 (a) and (d), a DRPM comprises a plurality of mirror pairs (Edmund Optics Inc.) circumferentially arrayed about the rotational axis, forming a circular array of discrete rotational symmetries. The centers of the mirror pairs are spaced apart from one another at a prescribed angular displacement, $\theta$. Each mirror pair is composed of two mirrors $M1_n$ and $M2_n$ ($n$ = 1, 2… $N$, $N$ is the total number of mirror pairs) arranged in parallel. The centers of the mirror $M1_n$ and $M2_n$ are located at a prescribed radius $r$ and $R$, respectively, from the rotational axis. The normal of the mirror is inclined at a prescribed angle, $\delta$, with respect to the rotational plane. The sample beam is sequentially reflected by the mirror $M1_n$ and $M2_n$. The normal of reflective facet of $M1_n$ $\vec{n}_0 = \begin{bmatrix} -\cos\delta & 0 & \sin\delta \end{bmatrix}^T$, when the light is illuminating at the center of the mirror. $\vec{i} = \begin{bmatrix} 0 & 0 & -1 \end{bmatrix}^T$ is the unified vector of incident beam. When the DRPM rotates at a constant speed ω, at time t, the normal vector of the mirror $M1_n$ can be expressed as

$$\vec{n} = M_\omega \cdot \vec{n}_0 = \begin{bmatrix} \cos\omega t & \sin\omega t & 0 \\ -\sin\omega t & \cos\omega t & 0 \\ 0 & 0 & 1 \end{bmatrix} \cdot \begin{bmatrix} -\cos\delta \\ 0 \\ \sin\delta \end{bmatrix} = \begin{bmatrix} -\cos\delta\cos\omega t \\ \cos\delta\sin\omega t \\ \sin\delta \end{bmatrix}, \tag{4.1}$$

where the rotational matrix $M_\omega = \begin{bmatrix} \cos\omega t & \sin\omega t & 0 \\ -\sin\omega t & \cos\omega t & 0 \\ 0 & 0 & 1 \end{bmatrix}$; According to the law of reflection, the vector of the sample beam reflected by the mirror M1$_n$

$$\vec{d} = \begin{bmatrix} -\sin 2\delta \cos\omega t & \sin 2\delta \sin\omega t & 2\sin^2\delta - 1 \end{bmatrix}^T. \tag{4.2}$$

Again by the law of reflection, the vector of the sample beam reflected by the mirror M2$_n$ $\vec{s} = \vec{i}$.

A prototype DRPM has been developed by the author. Totally ten mirror mounts, a rotary base, a shaft, two shaft mounts with ball bearings, a motor mounts, and an auxiliary mirror mount were designed by the author and all of the parts were fabricated by a mechanical company using aluminum alloy. To attach the square mirror onto the mirror mount, the square mirror was fixed onto an auxiliary mounts whose orientation can be finely adjusted using three extremely fine hex adjusters (F3ES12, Thorlabs Inc). The orientation and position of the square mirror were carefully adjusted using the auxiliary mount and translation stage. The square mirrors were fixed in position using arodite glue. The detailed mechanical drawings of the scanner are provided in the appendix 1.

Fig. 4.1 (b) shows scanning principle of the device. The sample beam from the source is indicated by the lower cross (black) showing that it prorogates away from the observer. When $t = 0$, the reflection point on the mirror M1$_n$ is at the center of the mirror.

The reflected sample beam follows the optical path indicated by the solid line (red), so that the reflection point on the mirror M2$_n$ is at the center of the mirror M2$_n$ and follows the path indicated by the upper-right cross (red). When the two mirrors are angularly scanned with an angle $\omega \cdot \Delta t$, the sample beam reflected by the mirror M1$_n$ follows the optical path indicated by the dotted line (blue). The beam is further reflected by the mirror M2$_n$ and follows the optical path denoted by the upper-left cross (blue), so that the angular scanning of the sample beam is transformed to a parallel translation along the direction perpendicular to the plane formed by the optical path along $\vec{d}$ direction (between the two mirrors) and the path along the $z$-axis. Since the doubly reflected optical beam is translated around the incident beam with a fixed radius, the optical beam is scanned along an arc with the origin at the beam reflection point on the mirror M1$_n$. For the prototype scanner we developed, $\delta$ = 45°, $R$ = 45 mm, $r$ = 35mm and $N$ = 10. Shown in Fig. 4.1 (c), the trace of a line scan (dotted green curve) is an arc with radius R - r and angle $\theta$ = 36°. The beam displacement as a function of time in the back principal plane of the tube lens

$$\Delta l(t) = (R - r) \cdot \omega \cdot t. \tag{4.3}$$

The angular scanning range of the scanner

$$\pm \Delta A = \pm \operatorname{atan}\left[(R - r) \cdot \theta / (2 \cdot TL)\right], \tag{4.4}$$

where the tube length $TL$ = 100 mm and the corresponding angular scanning range is ±1.8°. In each cycle, the focus displacement inside the sample $\Delta\rho$ can be expressed as a function of time *t* with the origin at the moment when the incident beam illuminates the centers of the mirrors

$$\Delta\rho(t) = \frac{\Delta l}{M} = \frac{1}{M}(R-r)\cdot\omega\cdot t \tag{4.5}$$

where *M* is the magnification of the sample optics. Within each cycle, the displacement of focus is a linear function of time. For the expression of optical path-length, we split the optical path in to two parts: the optical path along $\vec{d}$ direction (between the two mirrors) and the path along the *z*-axis (from the source to M1n reflection point and from M2n reflection point to the sample). The path-length of the beam along the $\vec{d}$ direction can be written as

$$P = \frac{R-r}{\vec{d}\cdot\vec{n}} = \frac{R-r}{\sin\delta}; \tag{4.6}$$

its projection on the *z*-axis can be written as

$$P_z = P\cdot\cos 2\delta, \tag{4.7}$$

Therefore, the total optical path-length is independent of time within each scan cycle.

Shown in Fig. 4.2, an ASE light source (BBS-430, Newport) is used to provide broadband light in the 1525-1605 nm wavelength range, yielding an axial resolution of 13.4 μm in air. The system uses a circulator and dual balanced detection scheme. The optical circulator couples the light returning toward the source arm to a detector (except for an approximately 0.85-dB insertion loss), effectively doubling the signal power. A balanced differential detector is used to combine the signals while simultaneously rejecting common mode noise that is due to source-intensity fluctuations. In the sample arm the optical beam is collimated by a near-IR achromat L1 with a focal length of 30 mm and goes to a fast steering mirror, which is positioned in the back focal plane of the scan lens L2 (*f* = 100 mm). The front focal plane of the scan lens and the back focal plane of the tube lens L3 (*f* = 100 mm) coincide between the mirror $M1_n$ and $M2_n$. A synchronization beam of 650 nm emitted by a laser diode is reflected to the photodetector 2 by the mirror $M2_n$. At beginning of each line scan, a rising edge is detected at the photodetector 2 to provide the line synchronization. A near-IR objective lens L4 (Nikon CFI Fluor 10XW, NA = 0.30, focal length 20 mm) is underfilled resulting an effective NA of ~0.25, which gives a transverse resolution of 2.6 μm and confocal parameter of 30 μm. For high resolution application we use Nikon CFI Fluor 40XW with NA = 0.85, which gives a transverse resolution of 0.8 μm and confocal parameter of 2.5 μm.

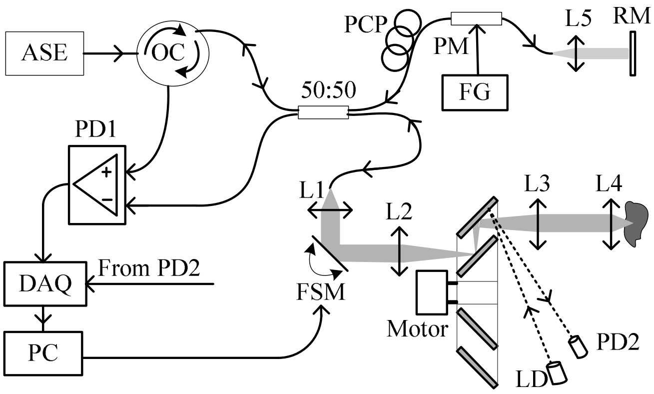

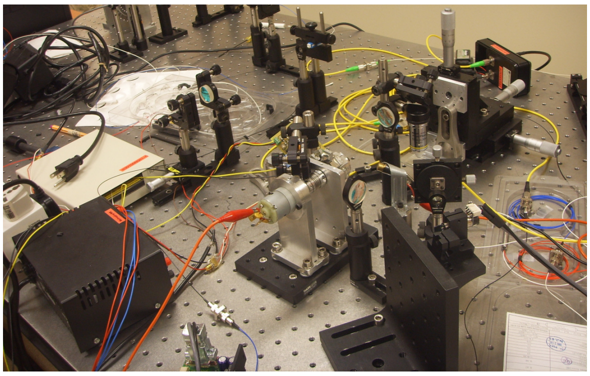

Fig. 4.2 Schematic and photo of OCM used for imaging experiments. OC: optical circulator; PCP, polarization control paddles; PM: fiber-based phase modulator; RM: reference mirror; FG: function generator; FSM: fast steering mirror; PD1: photodetector1; LD: 650 nm laser diode; PD2: photodetector2; DAQ: data acquisition device; PC: personal computer.

### 4.3.2 Biological tissue models and imaging

Onion skin is obtained from the local market, and a piece of fresh onion skin was held in place under the water and was imaged using the Nikon 10X water dipping objective lens. Normal Wistar rat liver tissues (fixed) were obtained from Prof. Hanry Yu's lab at Institute of Bioengineering and Nanotechnology. The liver tissue sample was held in place under the water and was imaged using the Nikon 40X water dipping objective lens.

## 4.4 Results

Fig. 4.3 shows the heterodyne interference signal between the reference and sample arm light, and its log-demodulated envelope. The signal amplitude is almost constant demonstrating that the optical path-length is maintained during the scanning. The theoretical scanning duty cycle is close to 100%. However, in practice, it is reduced to ~90% due to the gaps between the mirror pairs. To acquire *en face* images, we drive the DRPM with a DC motor of 18,000 rpm, scanning 3000 lines/s. The FSM is driven at 6 Hz to yield 500 lines per image. The high duty cycle of the scanner provides a large field of view of 400μm×750μm. To ensure the maximum heterodyne signal, we carefully match the reference-arm path length to the sample-arm path length to the focus. According to the geometry plotted in Fig. 4.1 (c), for each pixel of the final image in the Cartesian coordinates we locate the corresponding pixel in the polar coordinates with a nearest neighbor interpolation. Fig. 4.4 (a) shows the image of the resolution target captured by putting all the scan lines of the DRPM together. In Fig. 4.4 (b) a corrected image demonstrates the high scanning linearity of the DPRM. The group 7 element 2 with spacing of 3.5 μm can be clearly resolved. By use of the 10–90% width of an edge scan [126], the Gaussian spot $e^{-2}$ radius was estimated to be ~3 μm. The pixel number is 500×1000 and the pixel size of 1.5 μm×0.4 μm.

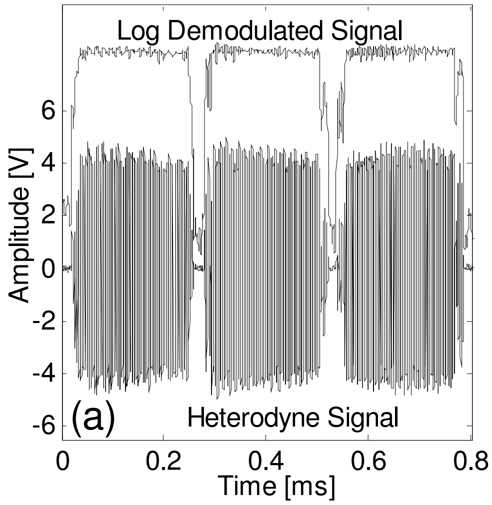

Fig. 4.3 Heterodyne modulation signal

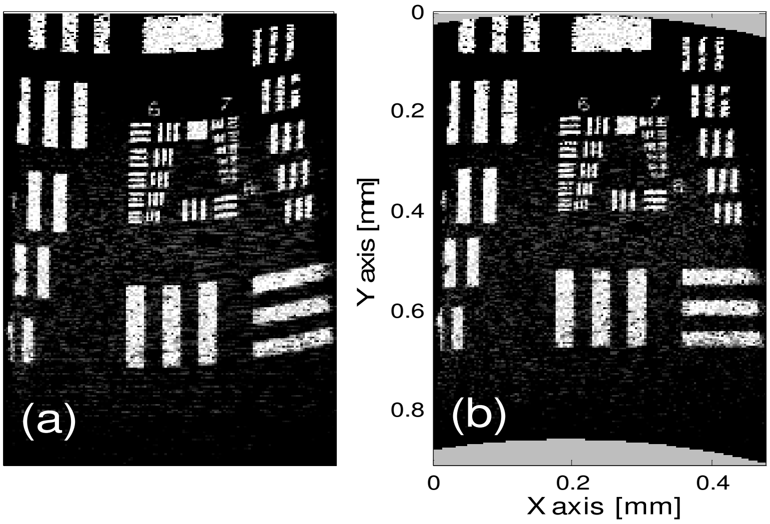

Fig. 4.4 (a) image of a US air force resolution target in the polar coodinates; (b) corresponding image in the Cartesian coordinates.

The performance for imaging biological samples is demonstrated in Figs. 4.5 (a) and (b), showing the cellular structure of an onion skin at a probing depth of 110 µm and 200 µm. Figs. 4.5 (c) shows an image of normal rat liver tissue. The high transverse resolution allows resolution of subcellular details such as the cell wall and the cell nuclei. Imaging was performed with 5-mW power and 93 dB sensitivity at 12 frames /s.

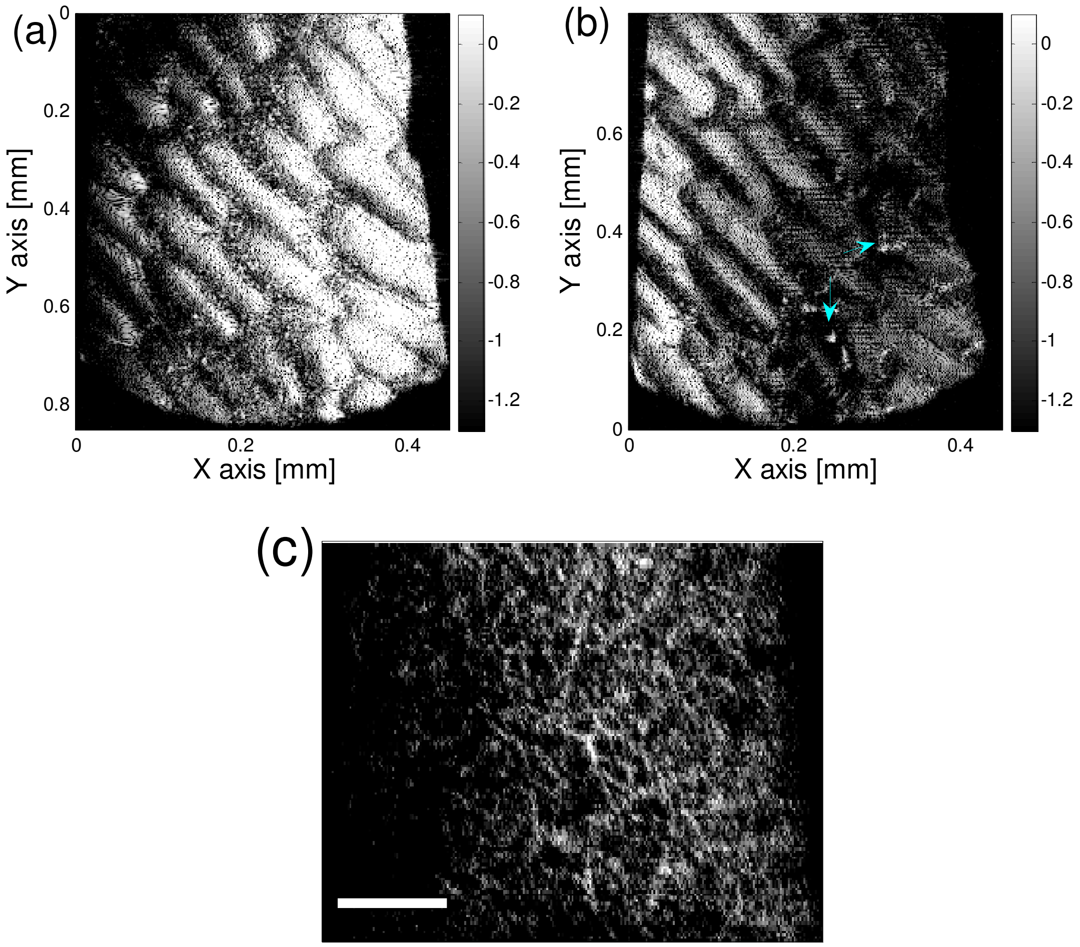

Fig. 4.5 Cellular structure of an onion skin at a probing depth of (a) 110 µm (2) 200 µm, and cell nuclei are indicated by the arrows; (c) cellular structure of rate liver tissue at a probing depth of 50 µm. Scale bar: 20µm.

## 4.5 Discussions

The double-reflection rotary parallel mirror array based beam scanning scheme has a number of advantages. First of all, real-time imaging can be implemented without sample scanning. If a motor with a speed of 20,000 revolution per minute is used, this scanning means can provide a line rate up to 6~25 kHz; if 1024 lines are used for a frame, the imaging frame rate range will be 6~25 frame per second; Second, as shown by Eq. (4.5), the scanning speed is linearly dependent on the scanning time. Third, a scanning duty cycle close to 1 can be obtained since the incident beam upon the scanner is a focused beam instead of a collimate beam. Fourth, the scanning is free of optical path length modulation. Fifth, objectives with arbitrary numerical aperture can be used to get images of different resolution and field of view. The last, the presented scanner has good scalability in terms of scanning range and speed. Much faster scanning can be achieved with increased number of mirror pairs; larger scanning range can be obtained with greater distance between the two mirrors.

The DRPM based scanner is currently still in the early stage of its development. Although the first prototype has demonstrated a very fast line-scanning speed, it is not optimized, stable and robust at all. First of all, lack of proper isolation equipment and measures makes the whole system vulnerable to the mechanical vibration caused by the spinning of the motor and the device. Consequently, the intensity of the interference fringes fluctuates within a range larger than the mean value; the optical path-length and the position of the optical components can not maintained due to vibration. One can see in Fig. 4.4 and Fig. 4.5 large vibration artifacts (black dots, and stripes), which elevate the overall noise floor of the image, resulting in a much smaller penetration depth. Secondly, the high-speed operation and vibration of the scanner gives rise to displacement of the mirrors relative to the mirror mounts during the long-term operation. The epoxy glue may not stand the long-time high torsion caused by the high-speed rotation and the stress caused by the vibration, so that it may undergo plastic deformation and gives rise to differences in both optical path-length and scan line position amongst mirror pairs. Thirdly, since the operation wavelength (1550 nm) is sitting on the absorption peak of water, so that measurement with water dipping lens is not possible, causing large spherical aberration induced by the refractive index mismatch between the air and the tissue sample. The spherical aberration will eventually degrade the spatial resolutions and signal strength of the measurement. Lastly, the ST connector of the phase modulator allows the almost all of the light reflected by the fiber tip coupled back to the detector, giving rise to large excess photon noise and future degrading the system sensitivity.

The problem of mechanical vibration can be addressed by better isolation between the scanning component and still parts. A damping table is necessary for the stability of the fringe intensity. The mechanical bearings should be replaced by the non-contact type air bearings for better isolation and less friction. A second prototype scanner should be made using professional fabrication facilities. A light source of shorter center wavelength, for example 800 nm or 1300 nm, can be used to facilitate use of water dipping lens. A phase modulator with an APC pigtail should replace the ST pigtailed one to minimize the excess noise.

## 4.6 Conclusion

In conclusion, a simple, high-speed, high-efficiency, high-duty-cycle, path-length maintaining and linear beam scanner is proposed for *en face* scanning optical coherence microscopes. A line scanning rate of 30 kHz and a scanning range of ±1.2° can be readily achieved with a DC motor of 60,000 rpm, a mirror pair number of 30 and a scanner diameter of 100 mm. **To our knowledge, our invention is the fastest scanner for *en face* OCM imaging.** The proposed scanner facilitates dual-mode imaging, for instance, optical coherence / multi-photon microscopy or optical coherence / focal modulation microscopy to achieve real-time simultaneous molecular-specific and morphological contrast deep tissue imaging *in vivo*.

There are still technical problems with the first prototypical scanner and the whole imaging system, such as mechanical vibration, spinning rate, fabrication precision /accuracy, robustness, and SNR of the imaging system. All these problems can be properly addressed by advanced mechanical design, fabrication and dedicated optical components. However, the current funding and workload might not support further investigation and developments, which might be done under additional support and in later stage of research.

# Chapter 5 SUPER-RESOLUTION ALONG AN EXTENDED DOF FOR *IN VIVO* DEEP TISSUE IMAGING

## 5.1 Introduction

Optical coherence tomography is an emerging imaging tool with non-ionizing, non-radiating, high resolution and high contrast imaging. High-performance OCT also promises real-time, non-invasive or minimal invasive, *in vivo* imaging based diagnosis in histopathology or cellular level [129, 133], which is often referred as a kind of "optical biopsy" [144]. As we have identified in Chapter 1, currently there are a few important performances to improve before such an imaging modality is successfully applied in deep tissue imaging *in vitro* and *in vivo*. These performances include spatial resolution, scanning range, imaging speed, miniaturization of the probe (for endoscopy), and contrast. Among all these performances, spatial resolution is probably the most important parameter for all imaging modality and a high spatial resolution of 1~2 µm or less is required for cellular level imaging.

With the development of broad bandwidth femtosecond laser and SLED technology, axial resolution can be improved to 0.75 ~1.5 µm with the light source centered at 800 nm, but there is a trade-off between lateral resolution and depth of focus when conventional focusing are used: conventional focusing optics provides a diffraction-limited spot size of $\lambda/2n\mathrm{NA}$ (FWHM) and a DOF of $1.4n\lambda/\mathrm{NA}^2$ (FWHM), when a uniform circular aperture is assumed, where $\lambda_c$ is the vacuum wavelength, $n$ is the refractive index [99]. The transverse resolution is so related with the DOF that a beam cannot be produced that has simultaneously a long focal depth and a narrow lateral width. Therefore, compromise is usually made between the lateral resolution and DOF. In order to achieve a DOF long enough to cover an axial scanning range of ~2 millimeter, a low numerical aperture objective lens ( $NA = 0.04$ ) is typically used in a B-mode OCT system. The corresponding focusing condition delivers a relative low lateral resolution of 15 μm ( $\lambda_C = 0.8\mu m$ ) in comparison with an axial resolution of 1~9 μm determined by the coherence length of typical broadband light sources.

In recent years, there has been a trend toward implementing endoscopic optical biopsy by use of OCT [32, 84, 87, 90, 144-148], and *in vivo* experiment has been implemented successfully with the spatial resolution near the level of histopathology; however, it is believed that the ability to image at the cellular level could improve the effectiveness of quantitative macrophage determination [90], and many surgical and microsurgical procedures [144]. It then becomes a challenging task to improve transverse resolving power of OCT without compromising the DOF, since use of lens with larger NA results in a much smaller DOF.

Super-resolution along an extended DOF is of great interest for cellular-level imaging with endoscopic OCT due to not only the theoretical limitations but practical implementations. Increasing NA of the objective lens is limited by overall probe size; a lens of large aperture size or small working distance is not practical for miniaturized probes working in internal tubular organs, such as gastrointestinal tracts, respiratory tracts and blood vessels.

## 5.2 Literature review

To overcome this limitation, dynamic focusing scheme (C-mode imaging) has been devised to increase the focal range of OCM systems [149-150]. However, dynamic focusing lenses are bulky so that it is difficult to be utilized in miniaturized probes for endoscopic OCM systems. Increased focal depth can also be realized by placing an annular aperture on the lens pupil [151-153]. An inverse scattering method has been proposed to produce spatially invariant resolution inside and outside of the focal region by rephasing the scattered signal [154, 155]. However, the out-of-focus signal is still attenuated due to the confocal effect. Axicon lens has been used to produce an effective DOF of 6 mm with a lateral resolution of 10 μm [156], whereas the focal volume carries only ~5% of the total power, limiting its application for biomedical samples. The power efficiency of such an axicon lens based scheme can be improved by decoupling the detection and illumination path [157]; nevertheless, the obtained DOF is limited by the confocal range (~200 μm) of the detection optics.

To achieve super-resolution along an extended DOF, many designs of pupil filters have been presented. These include amplitude filters, pure-phase filters and complex filters. Amplitude filters and complex filters are not energy-efficient since certain part of pupil area is obstructed; Continuous varying phase filters are difficult to implement in miniaturized probes; Pure-phase binary filters consisting of arrays of concentric rings have been demonstrated to be an effective and energy-efficient axial apodizer [158-162]; more importantly, such a filter can be easily fabricated and miniaturized, which make it the best fit for *in vivo* high-resolution endoscopic imaging applications.

H. Wang *et al* demonstrated that super-resolution and extended DOF can be achieved with binary-phase only masks assuming the optical beam is uniform and monochromatic [158-162]. However, this assumption is not valid for most practical applications. For instance, in a fiber-based scanning endoscope the transverse profile in the pupil plane of the objective lens is always a Gaussian distribution cut at a certain power level. It will be demonstrated in the results of this chapter that there is significant difference between the performances of binary-phase only masks under Gaussian beam profile and uniform beam profile. There has been little written concerning the effects of transverse beam profile on the performances of the filters and few experiment reported to validate the behaviors of such an important class of filters.

## 5.3 Materials and methods

In this chapter, BPSFs are classified into two sub-classes according to their axial and transverse performances; dependences of the filter performances on the transverse beam profile are presented numerically. Optimized designs are proposed for either high-resolution or ultra-large-DOF applications, and experimental results are shown to verify the theoretical predictions [163, 164]. As a proof-of-principle study, real-time images of simple samples and human skin *in vivo* are acquired to validate the efficacy of the proposed method [130, 165].

### 5.3.1 Analytical model and numerical results

The structure of BPSF is shown in Fig. 5.1 (a). A BPSF is composed of an array of concentric rings, and the radii of the rings are $a$, $b$, $c$, $d$, $e$, $f$ *and* 1 normalized to the pupil radius. The phase of each ring $\Phi$ is set to be 0 or $\pi$ regarding the center wavelength $\lambda_c$. In our present work, Gaussian beam profile and broadband source spectrum are taken into account to simulate the situations in a typical fiber-based SS-OCM. Shown in Fig. 5.1 (b), such a BPSF is mapped to the pupil plane of the objective lens. Therefore, the modulated pupil function can be written as

$$P(k,r) = \exp\left[i\Phi(k,r)\right], \tag{5.1}$$

where wave number k=2π/$\lambda_c$; $r$ is the radial coordinate normalized by the pupil radius $a_0$; the normalized wavelength dependant amplitude distribution in the sample space is given by [166]

$$g\left(k,\rho,u\right) = 2\sqrt{S(k)}\int_0^1 \tilde{f}P(k,r)rJ_0\left(\rho r\right)\exp\left[-\left(1/2\right)iur^2\right]dr, \tag{5.2}$$

where $\rho = k\left(NA\right)r_1$ and $u = k\left(NA\right)^2 z$ are the simplified radial and axial coordinates in the sample space respectively. $r_1$ and $z$ are the real radial and axial coordinates in the sample space and $NA$ is the effective numerical aperture of the objective lens. $S(k)$ is the source spectral intensity distribution; $J_0$ is zero-order Bessel function. Without loss of generality, circular, linear-polarized single mode fiber is assumed. Under the condition of Gaussian approximation, the amplitude profile of the fiber in the pupil plane $\tilde{f}$ is given by [167]

$$\tilde{f}\left(k,r\right) = 2\pi\left[r_0\left(k\right)\right]^2 \exp\left\{-\left(1/2\right)\left[2\pi\ r\ r_0\left(k\right)a_0 / f_o / \lambda_c\right]^2\right\}, \tag{5.3}$$

where $f_o$ is the focal length of the objective lens and the ratio $a_0 / f_o = \sin\left(\tan^{-1} NA\right)$. The wavelength dependant spot size $r_0(k)$ can be approximate as [168]

$$r_0(k) = r_{co} / [2 \ln V(k)]^{1/2} \tag{5.4}$$

where fiber parameter $V(k) = kr_{co}NA_f$, the core radius of the fiber $r_{co}$ = 4.1 μm. The normalized effective amplitude PSF of the sample arm optics can be written as

$$g_{eff}(\rho, u) = \int_{k_{\min}}^{k_{\max}} [g(k, \rho, u)]^2 \, dk \tag{5.5}$$

where $k_{min}$ and $k_{max}$ are cut-off wave numbers.

Assuming a top-hat source spectral intensity distribution $S(k)$ with a predefined bandwidth, the radii of the BPSFs shown in Fig. 5.1(a) can be systematically optimized based on searching in a discrete three-dimensional space (a b c d e f) for the axial intensity distribution with the least standard deviation within an extended axial focal range.

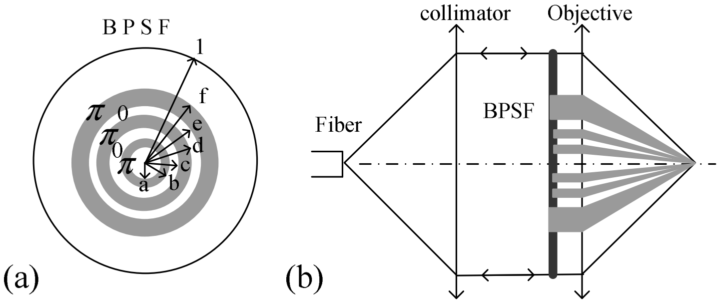

Fig. 5.1 (a) Structure of the BPSF; (b) BPSF optimized sample arm optics.

Properties of such a filter include the super-resolution factor, DOF gain, Strehl ratio, axial intensity nonuniformity and side-lobe strength: axial intensity nonuniformity is defined here as the ratio of the largest intensity fluctuation between two intensity maxima to the peak intensity; the side-lobe strength is defined here as the peak power ratio of the first side-lobe to the main lobe. The first three properties can be expressed in terms of the moments of the pupil [169, 170]. However, the last two properties can only be retrieved by calculating the diffraction field. The relative importance of these factors depends on the application. The super-resolution factor might be an important property for cellular-resolution applications, while filters with a very large DOF gain might be ideal for optical biopsy *in vivo* near the level of histopathology.

Simple and power-efficient pupil filters are designed to break the diffraction limit along a large DOF for the Gaussian beam. In the paraxial Debye regime, dependence of superresolution factor, DOF gain, Strehl ratio, side-lobe strength and axial intensity nonuniformity on the Gaussian profile in the pupil plane is characterized using the numerical method. Optimal filter designs are proposed for either high-resolution or ultra-large-DOF applications followed by experimental verifications.

### 5.3.2 Depth-invariant super-resolving filters

To investigate the dependence of the filter performances on the different Gaussian beam intensity profile, Thirteen discrete power levels, which define the pupil radius, is chosen to represent the whole power range of the Gaussian beam. For each power level, a filter design is obtained via exhaustive searching in a multi-dimensional space ($a$, $b$, $c$, $d$, e, and f) for the axial intensity distribution with the best uniformity within an axial range 3 times as large as the conventional DOF. In Table 4.1, optimized filter designs are provided for different power levels at the pupil radius ranging from 100% to 0.1%. These filters are featured with depth-invariant super-resolution, namely, depth-invariant super-resolving filters. In Fig. 5.2 (a), it is expected that the diffraction-limited spot size (blue solid curve) increases monotonically with the decrease of the power levels at the pupil radius, however the spot size achieved with the depth-invariant super-resolving filters (red circles) is almost constant around 0.4λ/NA for power levels above 10%. In Fig. 5.1 (b), the Strehl ratio (indicated by the black diamonds) fluctuates between 0.14~0.15 before 50% power level and goes to its minimum at 1% power level. In Fig. 5.1 (c), the side-lobe strength (the blue squares) is roughly the same for all power levels, while the axial intensity nonuniformity (blue hexagrams in Fig. 5.1 (d)) of power levels above 50% is below -25 dB. These facts indicate that the performances of such a sub-class of filters reach their optimum when the pupil radius is located at around 50% power level of the Gaussian beam.

Table 5.1 Dimension parameters of the depth-invariant superresolving filters

| **Power level (%)** | $r_1$ | $r_2$ | $r_3$ | $r_4$ |
|---|---|---|---|---|
| 100 | 0.10 | 0.28 | 0.47 | 0.67 |
| 90 | 0.10 | 0.28 | 0.49 | 0.69 |
| 80 | 0.10 | 0.29 | 0.49 | 0.69 |
| 70 | 0.07 | 0.27 | 0.48 | 0.68 |
| 60 | 0.07 | 0.26 | 0.48 | 0.68 |
| 50 (Filter 1) | 0 | 0 | 0.33 | 0.61 |
| 50 (Filter 2) | 0.08 | 0.23 | 0.44 | 0.65 |
| 40 | 0.09 | 0.28 | 0.49 | 0.68 |
| 30 | 0.18 | 0.37 | 0.53 | 0.70 |
| 20 | 0.14 | 0.31 | 0.48 | 0.67 |
| 13.5 | 0.09 | 0.28 | 0.48 | 0.67 |
| 10 | 0.09 | 0.27 | 0.47 | 0.66 |
| 1 | 0.10 | 0.17 | 0.31 | 0.53 |
| 0.1 | 0.15 | 0.19 | 0.21 | 0.40 |

H. Wang *et al* reported that for a uniform beam profile the DOF gain of such filters is at most 4.88 [159], which still holds true for other beam profiles based on Gaussian distribution. The DOF gain for filters in Table 4.1 is around 3.5. One can always trade axial intensity nonuniformity and/or Strehl ratio for a larger DOF gain within this limit.

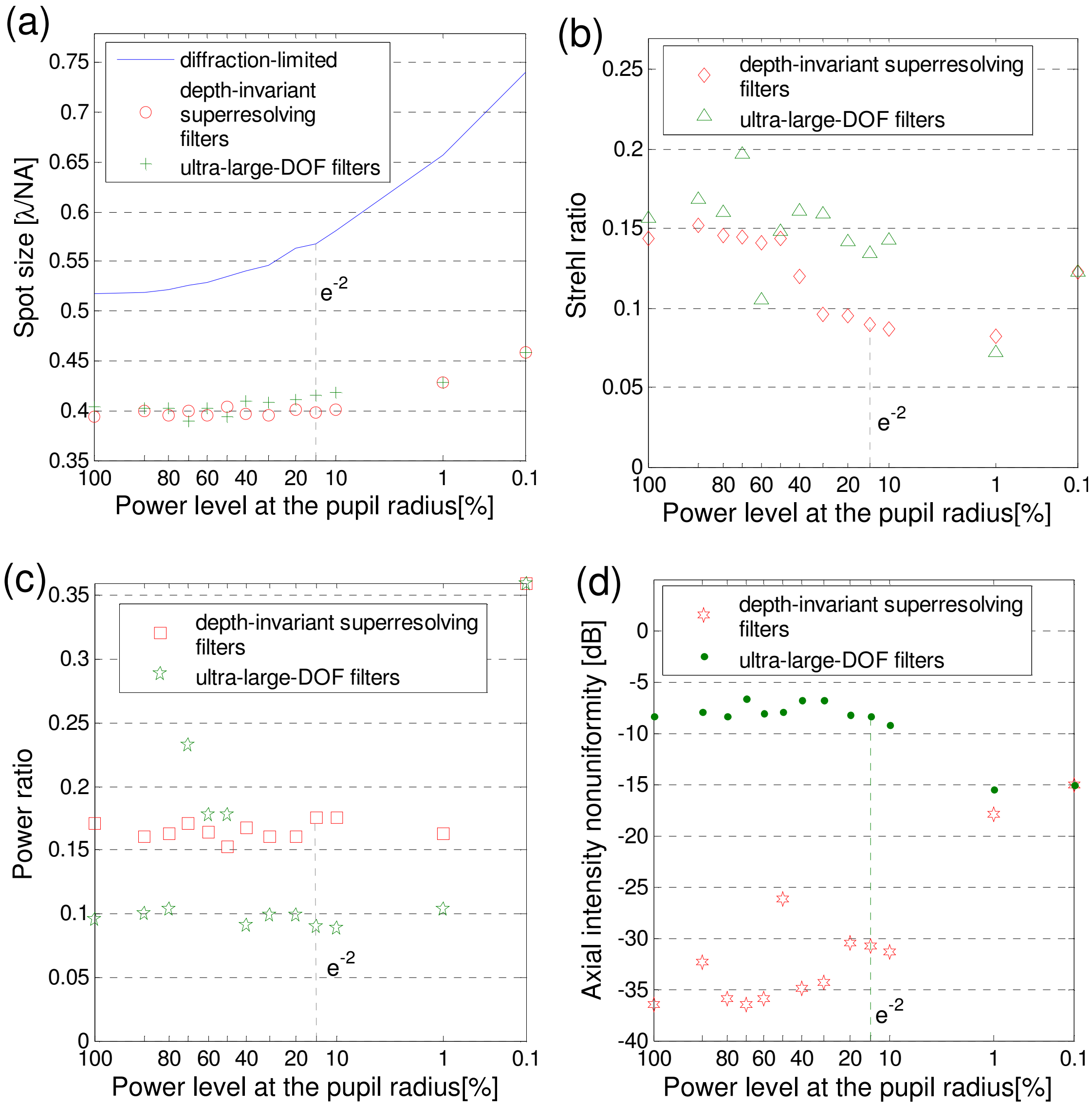

Fig. 5.2 Parameter of BPSFs. (a) Spot size in the focal plane, (b) Strehl ratio, (c) side-lobe strength and (d) axial intensity nonuniformity for the conventional focusing, focusing with binary-phase spatial filters.

Table 4.2 Performance parameters of optimized filters for pupil radius defined by 50% and 1% power level.

| **Filter performances** | **Pupil radius defined by 50% intensity level** | | | **Pupil radius defined by 1% intensity level** | | |
|---|---|---|---|---|---|---|
| | Diffraction -limited | Filter1 | Filter 2 | Diffraction -limited | Filter 3 | Filter 4 |
| Spot size (λ/NA) | 0.53 | 0.41 | 0.40 | 0.65 | 0.43 | 0.43 |
| Gain in DOF | 1 | 3.27 | 3.71 | 1 | 6.46 | 6.08 |
| Strehl ratio | 1 | 0.200 | 0.156 | 1 | 0.072 | 0.073 |
| Power ratio (the first peak vs. the central peak) | 0.013 | 0.119 | 0.149 | 0.004 | 0.107 | 0.106 |
| Axial intensity nonuniformity | -∞ | -20 dB | -26 dB | -∞ | -15 dB | -16 dB |

Shown in Figs. 5.3 (a), (b) and (c), with the pupil radius defined by 50% power level and NA = 0.01, the intensity PSFs are presented for the conventional focusing, focusing with a 3-ring filter (Filter 1 in Table 4.1) and the 5-ring filter (Filter 2 in Table 4.1) respectively. The coordinate $z$ stands for the axial position with origin at the focal point and $r$ denotes transverse radius. The performances of both filters are listed in the Table 4.2, from which we can see that the 5-ring filter is superior in every aspects except Strehl ratio. However, both filters demonstrate depth-invariant spot size with a super-resolving factor of 0.75.

### 5.3.3 Ultra-large-DOF filters

The limitation of DOF gain holds true only for the depth-invariant superresolving filters. Here we present another sub-class of filters that have much larger DOF gain. Ultra-large-DOF filter designs are obtained via exhaustive searching within an axial range 6 times as large as the conventional DOF. In Table 4.3, a filter design is provided for each power level.  Corresponding spot size in focal plane, Strehl ratio, side-lobe strength and axial intensity nonuniformity are shown as green crosses in Fig. 5.2 (a), orange triangles in Fig. 5.2 (b), red pentagrams in Fig. 5.2 (c), and purple dots in Fig. 5.2

(d). Since there are only two filters that provide axial intensity nonuniformity below -15 dB, we choose the two filters as optimized filters.

Table 4.3 Optimized parameters of the ultra-large-DOF filters

| **Power level (%)** | $r_1$ | $r_2$ | $r_3$ | $r_4$ |
|---|---|---|---|---|
| 100 | 0.08 | 0.34 | 0.55 | 0.73 |
| 90 | 0.03 | 0.32 | 0.54 | 0.72 |
| 80 | 0 | 0.30 | 0.53 | 0.71 |
| 70 | 0.16 | 0.36 | 0.55 | 0.73 |
| 60 | 0.16 | 0.36 | 0.55 | 0.72 |
| 50 | 0.14 | 0.34 | 0.54 | 0.72 |
| 40 | 0.07 | 0.22 | 0.45 | 0.67 |
| 30 | 0.07 | 0.20 | 0.43 | 0.65 |
| 20 | 0.11 | 0.22 | 0.41 | 0.64 |
| 13.5 | 0.13 | 0.23 | 0.41 | 0.63 |
| 10 | 0.28 | 0.39 | 0.42 | 0.60 |
| 1 (Filter 3) | 0.20 | 0.32 | 0.42 | 0.59 |
| 1 (Filter 4) | 0.05 | 0.07 | 0.24 | 0.37 |
|  | $r_5 = 0.44$ |  | $r_6 = 0.58$ |  |
| 0.1(Filter 5) | 0 | 0.04 | 18 | 40 |
| 0.1(Filter 6) | 0.15 | 0.19 | 0.21 | 0.40 |

Table 4.4 Performance parameters of optimized filters for pupil radius defined by 50% and 1% power level.

| **Filter performances** | **Pupil radius defined by 0.1% intensity level** |  |  |
|---|---|---|---|
|  | Diffraction -limited | Filter 5 | Filter 6 |
| Spot size (λ/NA) | 0.74 | 0.46 | 0.46 |
| Gain in DOF | 1 | 8.90 | 8.90 |
| Strehl ratio | 1 | 0.131 | 0.123 |
| Energy ratio (the first peak vs. the central peak) | 0.004 | 0.41 | 0.36 |

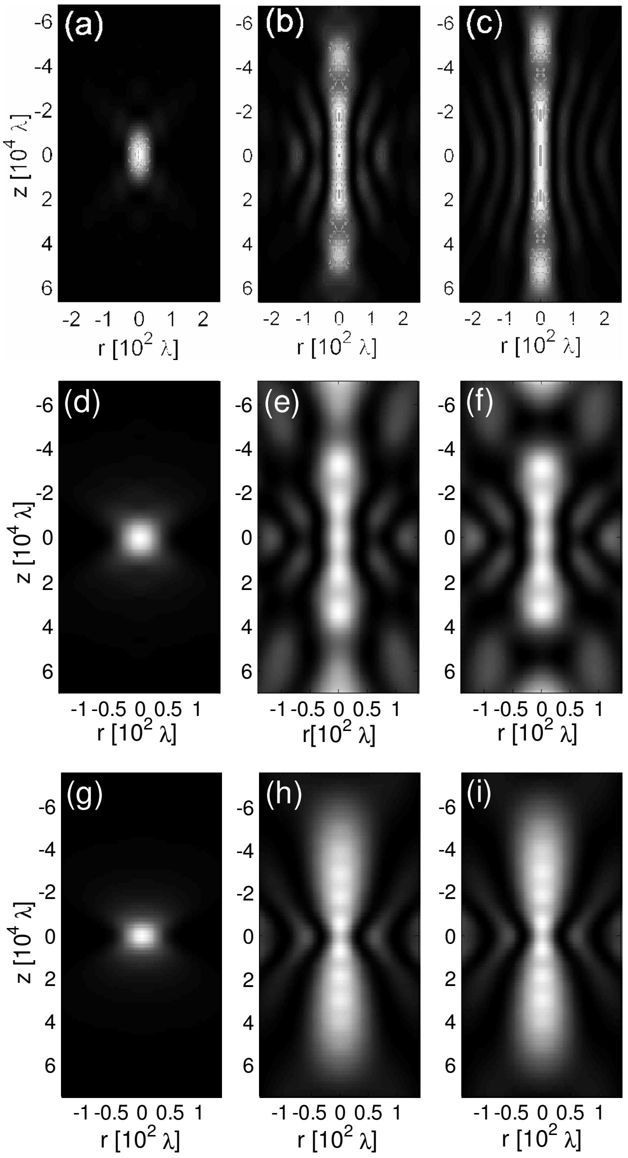

Fig. 5.3 Intensity distribution of the (a) conventional focusing, focusing with (b) Filter 1 and (c) Filter 2 with the pupil radius defined by 50 % power level; Intensity distribution of the (d) conventional focusing, focusing with (e) Filter 3 and (f) Filter 4 when the pupil radius is defined by 1% power level; Intensity distribution of the (g) conventional focusing, focusing with (h) Filter 5 and (i) Filter 6 when the pupil radius is defined by 0.1% power level.

Shown in Figs. 5.3 (d), (e) and (f), with pupil radius defined by 1% power level and NA = 0.0116, the intensity PSFs are presented for the conventional focusing,

focusing with the 5-ring filter (Filter 3 in Table 4.3) and a 7-ring filter (Filter 4 in Table 4.3) respectively. A dumb-bell shaped intensity PSF indicates that the spot size is depth dependent; nevertheless, the filters are still super-resolving along the full range of DOF under the Rayleigh range criterion. The performances of the two filters are listed in the Table 4.2, from which we can see that both filters have DOF gain above 6 and a super-resolving factor of 0.66.

It should be noted that for pupil radius defined by very small power level, filters with much smaller axial intensity nonuniformity can be found, which are featured with very large DOF gain and Strehl ratio. Such a filter as Filter 5 will be used for extending focus in real-time swept-source OCT in the following *in vivo* experiment. Shown in Figs. 5.3 (g), (h) and (i), with pupil radius defined by 0.1% power level and NA = 0.0143, the intensity PSFs in the sample space are presented for the conventional focusing, focusing with a 4-ring filter (Filter 5 in Table 4.3) and the 5-ring filter (Filter 6 in Table 4.3) respectively. For both filters, the achieved super-resolution factor, DOF gain, Strehl ratio and axial intensity nonuniformity are 0.62, 8.9, 0.13 and -16 dB respectively. Filter 5 has larger side-lobe strength of 0.4 than 0.36 achieved by Filter 6. However, both filters are super-resolving only in a limited region around the conventional focus.

### 5.3.4 Experimental setup for focal spot measurement

An optically addressed SLM (Thales Research and Technology, Palaiseau France) is used to create phase masks for our applications and a 4-wave shearing interferometry wave-front sensor (SID-4, Phasics Corp.) is used to register the phase map produced by the SLM. The principle and characteristics of the SLM have been presented in [171]. Fig. 5.4 (a) shows the structure of the BPSF used for the measurement of the focal spot, which is identical to that in Fig. 5.1 (a); Fig. 5.4 (b) shows a measured 3-zone binary wave-front with an annular ring of 3π and the rest region of 0 in phase. The unit of the color bar is radian. The steep phase gradient between different phase zones is expected. But it shows that undesired slow phase gradient is captured, this might be caused by either the SLM or wave-front sensor error or both.

Shown in Fig. 5.4 (c), a telescope system composed of an objective lens L1 (26X) and lens L2 (focal length = 250 mm) expands the optical beam from an Nd: YAG CW laser which provides $TEM_{00}$ laser at 1064 nm. Together with a pinhole, the telescope system also works as a spatial filter. The objective lens L3 and an aperture stop are positioned very close to the SLM so that the BPSF is mapped to the pupil plane of the objective lens. The aperture stop of the objective lens is carefully adjusted to the incident beam radius defined by the 50% power level. The effective numerical aperture of the objective lens is measured to be 0.0116. The phase excursion as a function of writing beam intensity is calibrated with a test gray map shown in Fig. 5.5 (a). The red and green channel of the test gray map is set to be 0 and the blue value of the pixels varies from 0 to 200 with a constant gradient. Figs. 5.5 (b) and (c) are acquired phase maps without and with the blue filter. The transmission coefficient of the blue filter is 25%. The unit of the color bar is radian. Fig. 5.6 plots the phase excursions of the SLM without (blue dashed curve) and with (red solid curve) the blue filter. Sine the gradient of phase curve with the blue filter is much less than the one without the filter, it is less sensitive to the addressing illumination non-uniformity. Shown in Fig. 5.7, the transverse beam intensity profile of the laser is acquired with the wave-front sensor with pixel number of 300×400 (not shown here).

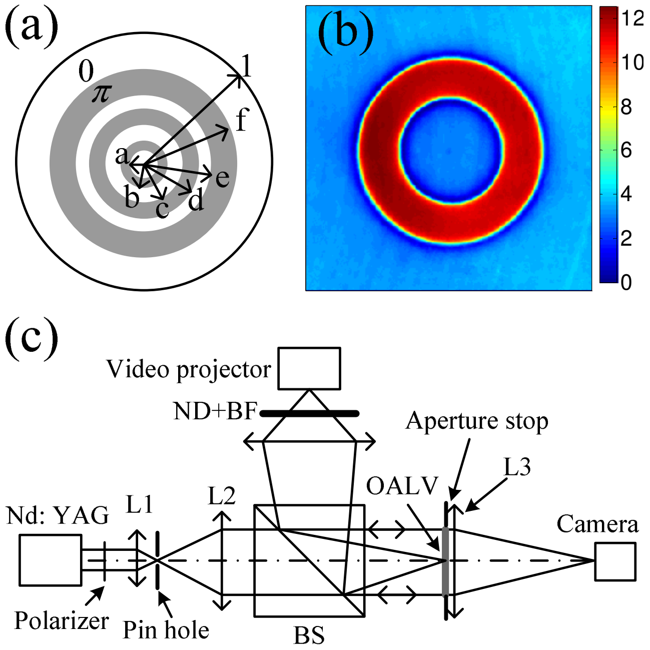

Fig. 5.4 (a) Structure of the binary phase mask; (b) a 3-belt binary wavefront created by OALV at TRT-fr; (c) Experimental setup. ND+BF: neutral density and blue filters. BS: beam splitter; OALV: optically addressed liquid crystal SLM.

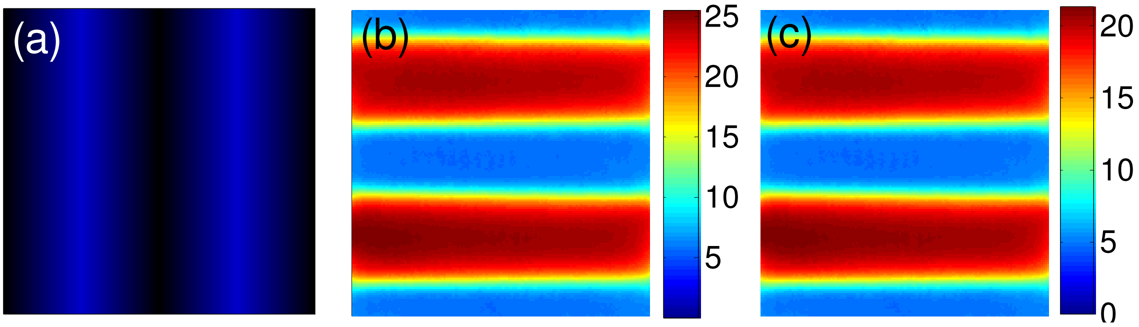

Fig. 5.5 Phase excursion calibration. (a) Test color map; (b) phase map acquired without the blue filter; (c) phase map acquired with the blue filter.

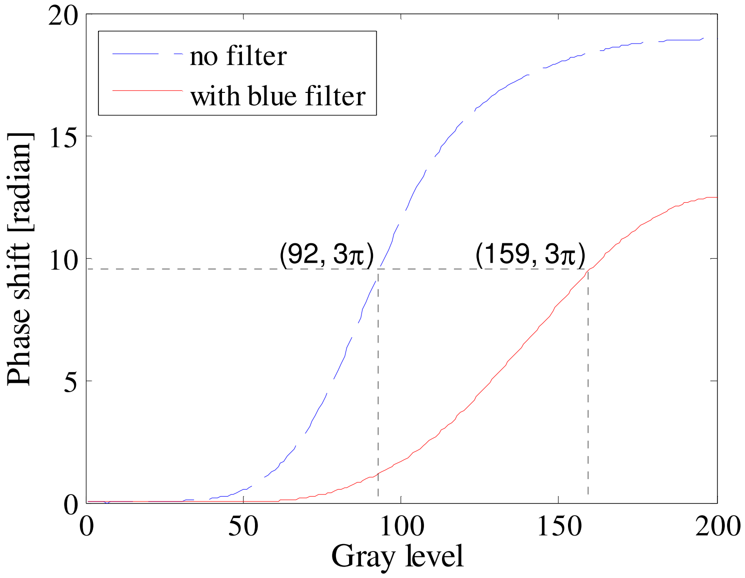

Fig. 5.6 phase excursion as a function of gray level of the projected video image. Blue dashed curve: without the blue filter; Red solid curve: with the blue filter.

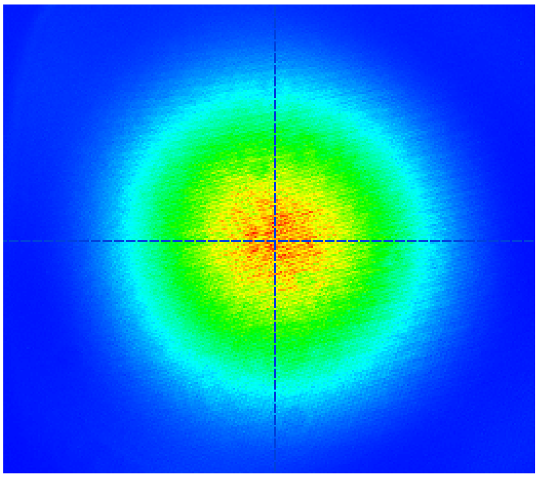

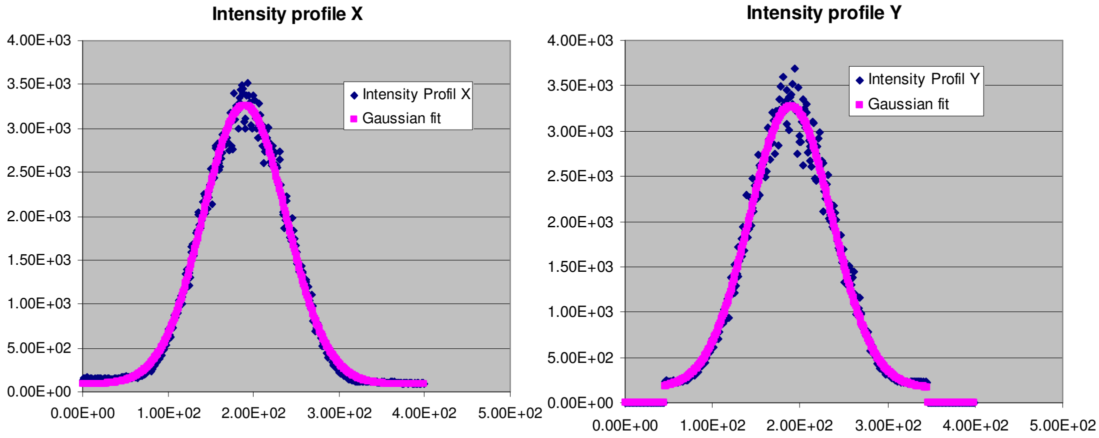

Fig. 5.7 Transverse beam intensity profile of the Gaussian beam (a) 2D profile; (b) Gaussian fit in the X direction; (c) Gaussian fit in the Y direction.

### 5.3.5 Experimental setup for in vivo OCT imaging

A swept-source OCT optimized by BPSF was developed for *in vivo* deep tissue imaging. Shown in Fig. 5.8, a swept source (SL1325, Thorlabs, Inc.) is used to provide broadband light in the 1260~1390 nm wavelength range, yielding an axial resolution of 12 μm in air. The system uses a circulator and dual balanced detection scheme. With an A-line repetition rate set at 16 KHz, the B-scan frame rate is 25 Hz with 640 A-lines per frame. In the sample arm the optical beam is collimated by a near-IR achromat L1 with a focal length of 40 mm and passes a linear polarizer and a SLM (X8267-1013M, Hamamatsu). The deflected beam then goes to a fast steering mirror. The beam is relayed to an objective lens L4 (near-IR achromat, $f_o$=40 mm) by a pair of identical near-IR achromat lenses L2 and L3 (f=100 mm).

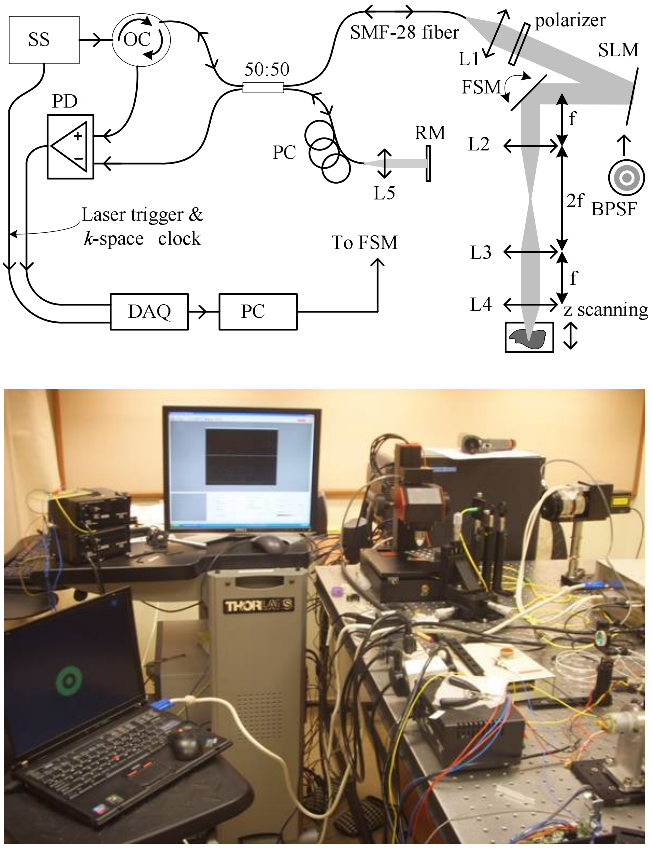

Fig. 5.8 Schematic and photo of SS-OCM used for imaging experiments. SS: swept source; OC: optical circulator; PC, polarization controller; RM: reference mirror; FSM: fast steering mirror; PD: photodetector; DAQ: data acquisition device; PC: personal computer.

Ultra-large-DOF filters are designed according to the system setup illustrated in Fig. 5.8. Assuming a top-hat source spectral intensity distribution $S(k)$ with a bandwidth of $\lambda_c/10$, the radii of the BPSFs shown in Fig. 5.1(a) can be systematically optimized based on searching in a discrete three-dimensional space (a b c) for the axial intensity distribution with the least standard deviation within an axial focal range of $1000\lambda_c$. The effects of different radii values on the optimized PSFs can be exemplified with four typical BPSFs: BPSF I (0.05 0.12 0.274), BPSF II (0.08 0.163 0.308), BPSF III (0.09

0.171 0.313) and BPSF IV (0.1 0.185 0.32). Fig. 5.9 (a) shows modulus of the effective axial PSFs of the conventional system and systems optimized with BPSF I-IV. With the BPSFs optimized systems, the achieved gain in DOF ranges from 9.8 to 11.5, whereas BPSFs with larger radii values give rise to larger amplitude fluctuations and axial side lobes. It is further assumed that the backscattered sample field intensity is much smaller than that of the reference field, the theoretical SNR differences between the focusing conditions optimized with BPSF I-IV and the conventional case at the focal position are −18 dB, −20 dB, −21 dB and −22 dB respectively. Fig. 5.9 (b) shows modulus of the effective lateral PSFs of the conventional and the four BPSF optimized systems. The BPSF optimized systems demonstrate a higher lateral resolution (FWHM) of 3.2 $\lambda_c$ compared to 5.0 $\lambda_c$ for the conventional system. Figs. 5.9 (c) and (d) show images of $\left|g_{eff}(\rho,u)\right|$ and the corresponding phase contour plots on the axial cross section for the conventional system and a system optimized with BPSF II respectively. Shown in Fig. 5.9 (c), the field changes from a converging spherical wave front to a diverging front within ~100 $\lambda_c$, while in Fig. 5.9 (d) plane waves are indicated by the straight lines along an extended DOF of ~1100 $\lambda_c$. The far field side lobe seen in Fig. 5.9 (d) has maximum modulus of 0.31 in the focal plane, which is much smaller than that reported in [158] (~0.4).

As one can see from Figs. 5.3 (h) (i) and Fig. 5.9 (d), the BPSF I-IV are actually very similar to the Filter 6 presented in section 5.3.1.2. However, the radii values are different due to the different Gaussian beam profile and the power levels that define the pupil radius.

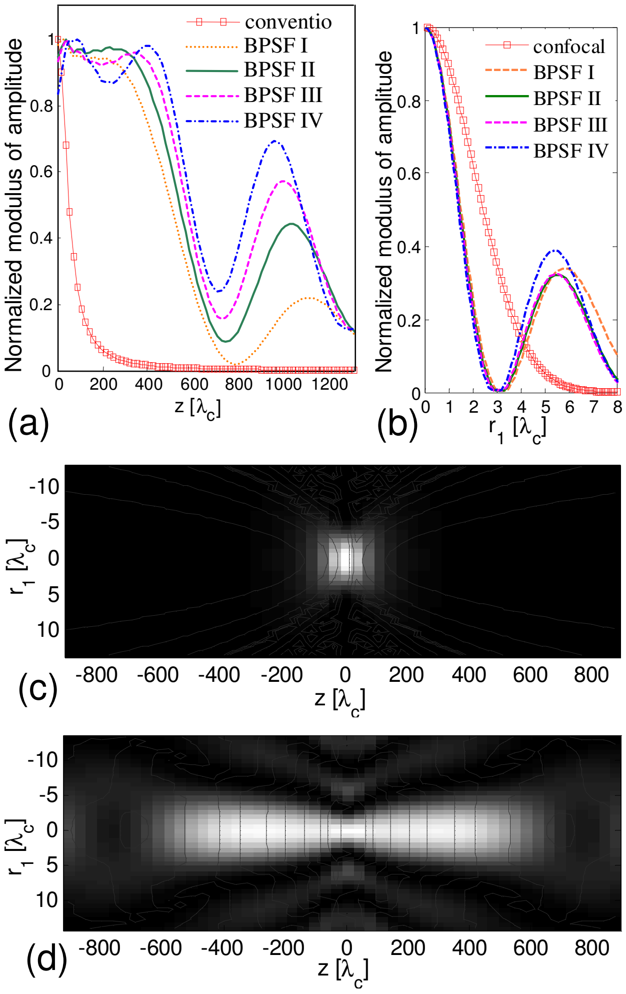

Fig. 5.9 (a) modulus of the axial beam profile: conventional case and cases optimized with BPSF I-IV; (b) modulus of transverse beam profile in the focal plane for the conventional case and cases optimized with BPSF I-IV; (c) modulus of amplitude image and phase contour plot in the focal region of the conventional system and (d) that optimized with BPSF II.

### 5.3.6 Human skin

The tissue sample for the *in vivo* imaging was the author's skin in the finger and proximal nail fold region. The total light power incident on the skin was less than 400 μW, and for a SSOCT imaging system that is capable of 16 kHz A-scan rate, the dwelling time on any given location is 39 μs. The average light intensity incident on the skin is 624 W/cm$^2$.

The ANSI sets a maximum permissible fluence for the use of laser on human subjects that a given location can be exposed to a continuous wave. The input fluence, as given by the product of the average light intensity with the dwelling time, is 0.06 J/cm$^2$, which is much lower than the ANSI safety limit for skin exposure [172].

## 5.4 Results

### 5.4.1 Focal spot measurement

According to the Gaussian fitted beam profile in Fig. 5.7, the radii of the binary phase masks are optimized numerically and the transverse focus intensity profiles are captured using a CCD camera to verify the theoretical results.

Figs. 5.10 (a)-(i) show calculated transverse intensity profile at different axial positions for the conventional system, system with Filter 1 and Filter 2 respectively; Figs. 5.10 (a')-(i') show the corresponding measured results. For better visualization, each profile for conventional focusing is auto-scaled. In Figs. 5.10 (a)-(c) and (a')-(c'), the spot size for the focusing with filters is smaller than that of conventional focusing. This lateral super-resolution resolution extends to the axial position of $z$ = 18 mm, where the conventional focus goes far beyond the focal depth and spreads to a very large transverse field. In Figs. 5.10 (g)-(f) and (g')-(i'), even in case of $z$ = 22 mm, the spot size with Filter 2 is still better than the diffraction limited one. The complete measured data can be viewed in the media 510. From left to right, transverse diffraction patterns of the conventional system, system with Filter 1 and Filter 2 are demonstrated with the axial position indicated at the top. In Fig. 5.11, the transverse intensity profiles of the conventional focusing (red dashed curve), focusing with Filter 1 (black dotted curve) and Filter 2 (blue solid curve) are plotted, and the measured superresolution factors are 0.77

and 0.78 respectively. The experimental results agree well with our theoretical predictions.

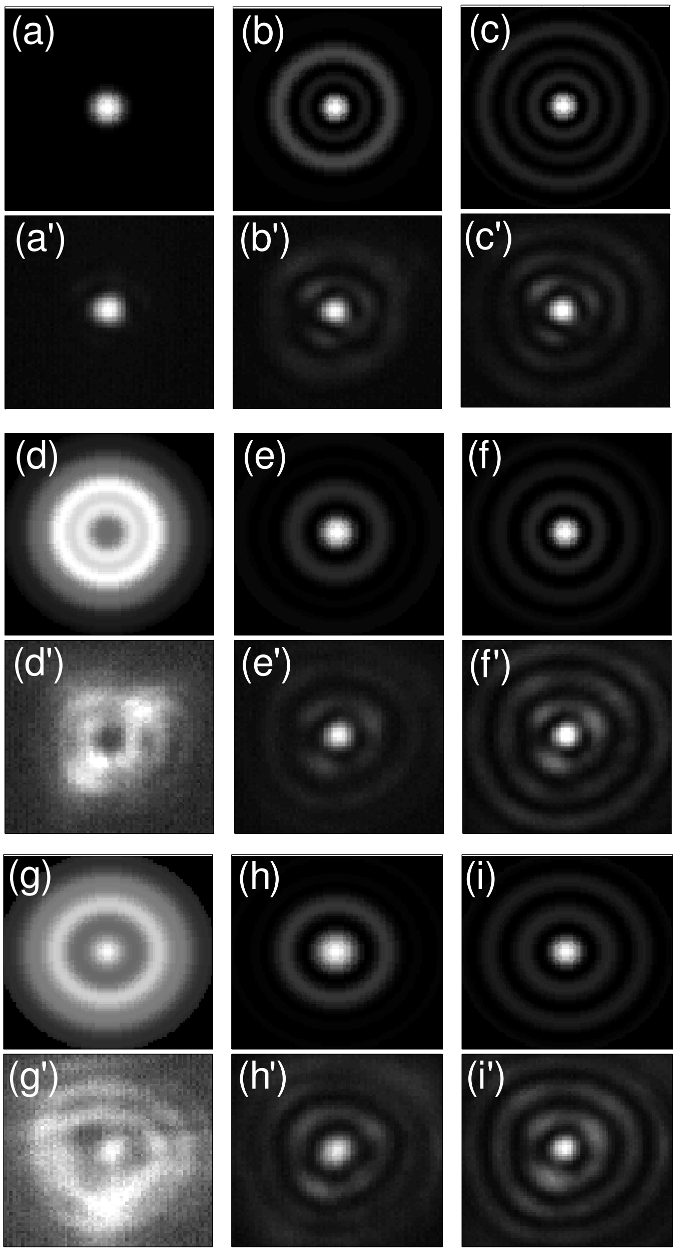

Fig. 5.10 Calculated transverse intensity distributions in the focal plane of the (a) conventional focus, focuses obtained with (b) Filter 1 and (c) Filter 2; transverse intensity distribution of (d) the conventional focus, focuses obtained with (e) Filter 1 and (f) Filter 2 at z = 18 mm; transverse intensity distributions of (g) the conventional focus, focuses obtained with (h) Filter 1 and (i) Filter 2 at z = 22 mm. (a')-(i') corresponding measured intensity.

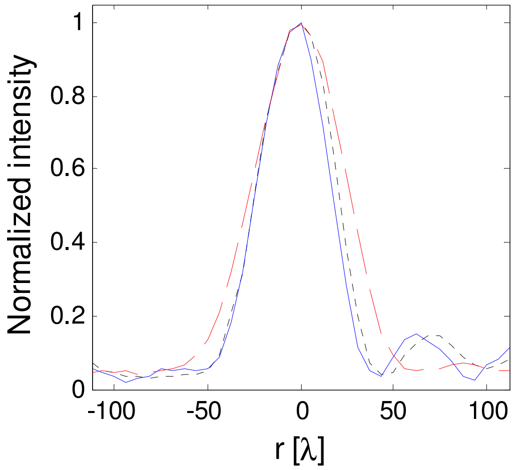

Fig. 5.11 Measured transverse intensity profiles in the focal plane of the conventional focusing (blue solid curve), focusing with Filter 1 (black dotted curve) and Filter 2 (red dashed curve).

Figs. 5.12 (a)-(i) show calculated transverse intensity profile at different axial positions for the conventional system, system with Filter 3 and Filter 4 respectively; Figs. 5.12 (a')-(i') illustrate the corresponding measured results. Shown in Figs. 5.12 (a)-(c) and (a')-(c'), the spot size for the focusing with filters is much smaller than that of the conventional focusing in the focal plane. Shown in Figs. 5.12 (d)-(f) and (d')-(f'), this lateral super-resolution resolution extends to the axial position of z=16 mm, where the conventional focus goes far beyond the focal depth and spread to a very large transverse field. Shown in Figs. 5.12 (g)-(f) and (g')-(i'), at z=36 mm, the spot size of focusing with the filters becomes larger than the diffraction limited one. The complete measured data can be viewed in the media 512. From left to right, transverse diffraction patterns of the conventional system, system with Filter 3 and Filter 4 are demonstrated with the axial position indicated at the top.

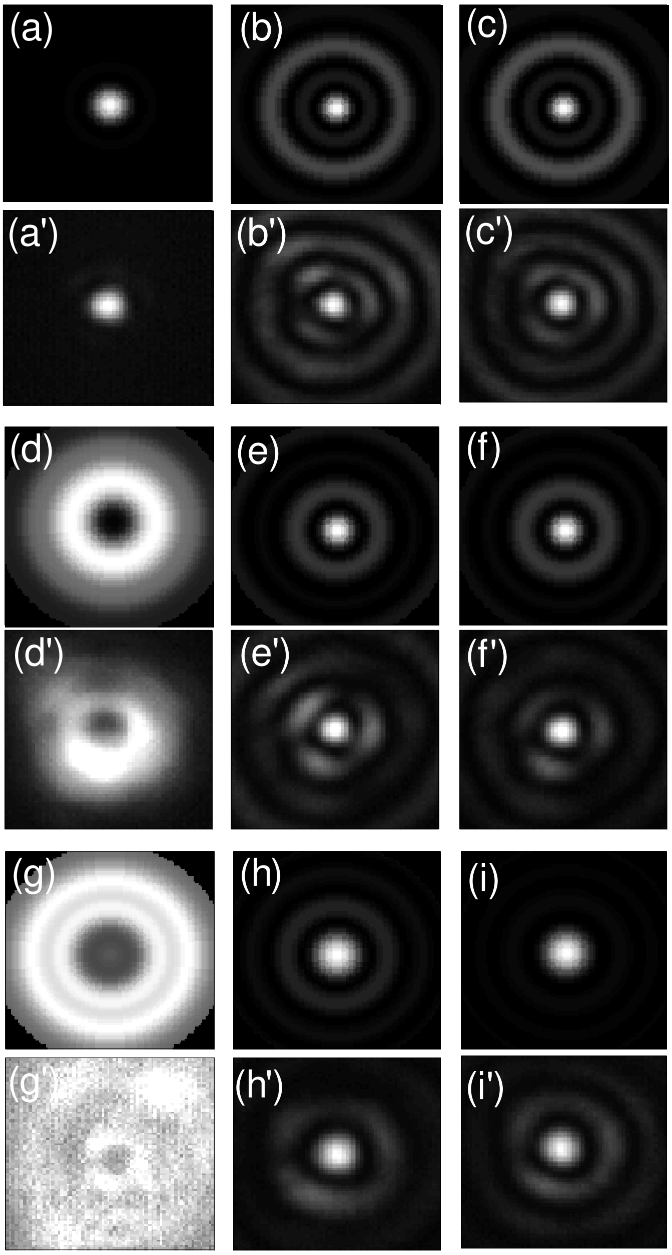

Fig. 5.12 Calculated transverse intensity distributions in the focal plane of the (a) conventional focus, focuses obtained with (b) Filter 3 and (c) Filter 4; transverse intensity distribution of (d) the conventional focus, focuses obtained with (e) Filter 3 and (f) Filter 4 at z = 16 mm; transverse intensity distributions of (g) the conventional focus, focuses obtained with (h) Filter 3 and (i) Filter 4 at z = 32 mm. (a’)-(i’) corresponding measured intensity.

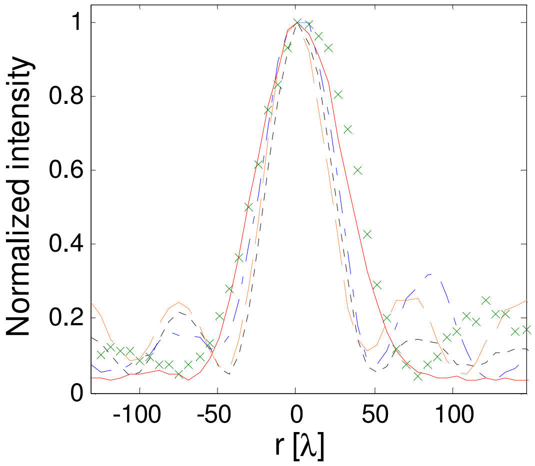

Fig. 5.13 Measured transverse intensity profiles of the conventional focus at z=0 (red solid curve) and focus obtained with Filter 3 at z=0 (black dotted curve), z = 8 mm (orange dashed curve), z = 16 mm (blue dash-dot curve) and z = 32 mm (green crosses).

Fig. 5.13 plots the measured transverse intensity profiles of the fosuing with Filter 3 at different axial position in the sample space. Compared with the diffraction-limited transverse intensity profile (red solid curve) Filter 3 are superresolving within z=±16 mm, equivalent to 2 DOFs for the conventional focusing. Even in case of z= 32 mm, the FWHM of the transverse intensity profile of the focusing with Filter 3 (blue dash-dot curve) is only 17% larger than the diffraction limited one. Again, the experimental results agree very well with our theoretical predictions.

### 5.4.2 OCT deep tissue imaging in vivo

The lateral resolution and axial signal distribution of the BPSF optimized SSOCT are estimated by taking images of a US air force test target located at different axial positions. Fig. 5.14 shows sequence of cross-sectional reflectivity profiles of the group 6, element 2-6 with an axial position interval of 300 μm. The spacing of element 5 is 101 line pairs /mm which correspond to a spatial resolution of 5 μm. A nearly constant axial signal distribution and a lateral resolution of 5 μm are demonstrated along an extended

DOF of 1.5 mm, which is in good agreement with our theoretical prediction. Figs. 5.15 (a) and (b) show tomograms of Latex calibration beads (diameter 5 μm, 0.1% W/V) acquired with the conventional and BPSF II optimized system respectively. In conventional case, a SNR advantage of ~18 dB over that of BPSF optimized system is observed at the focal position. Nevertheless, this advantage is rapidly lost and the image becomes blurred outside the corresponding confocal range of ~130 μm. The BPSF II optimized system exhibits high lateral resolution and a net SNR advantage along a DOF of almost 1.5 mm in water.

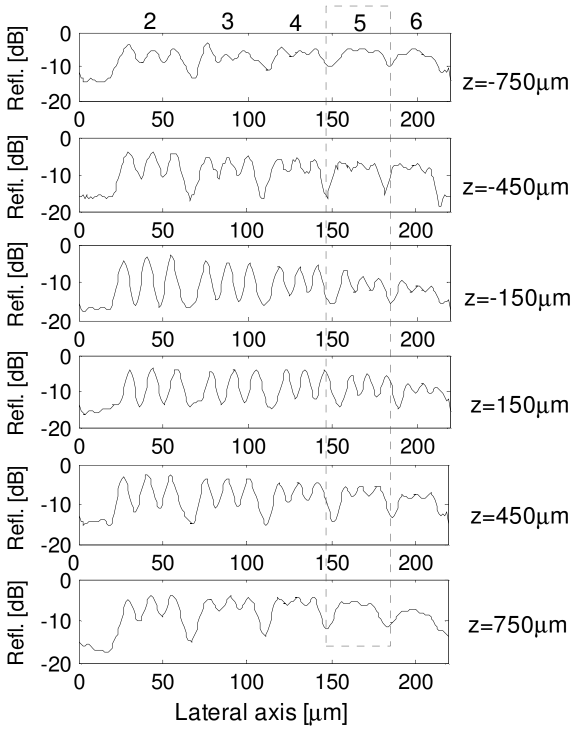

Fig. 5.14 Transverse signal profile at image plane obtained with BPSF II optimized systems. The element 5 is enclosed in the dotted box.

Figs. 5.16 (a) and (b) show tomograms of a human finger *in vivo* acquired with the conventional and BPSF II optimized system respectively. In the conventional case, the geometrical focus is at axial position of z = 500 μm, so that the signal becomes attenuated outside the corresponding confocal range of ~130 μm. The BPSF optimized system exhibits a net SNR advantage out of the confocal range. In addition, the image acquired with the BPSF optimized OCT demonstrate more details of the anatomical structure, such as sweat glands (SG) and interface between the stratum corneum (SC) and epidermis (E).

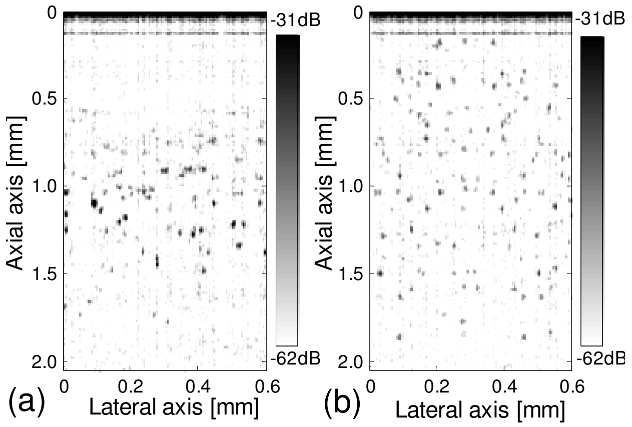

Fig. 5.15 Real-time tomograms of 5 μm latex calibration particles acquired with (a) the conventional system and (b) the BPSF II optimized systems.

Due to large differences in refractive indices between air and stratum corneum, stratum corneum and epidermis, there was strong back reflection at the skin-air interface and the interface between stratum corneam (SC) and epidermis (E). The strength of the back reflection becomes attenuated outside the corresponding confocal range of ~33 μm for the conventional case (Fig. 5.16 (a)), and one can hardly distinguish between the stratum corneum and epidermis above $z$ = 200 μm. Nevertheless, for the BPSF optimized case (Fig. 5.16 (b)) the strength of back reflection from the interfaces is almost constant. One can clearly distinguish between stratum corneum and epidermis even in z = 500 μm. Fig. 5.16 (a) and (b) is acquired with a frame rate of 21.6 Hz and image size of 1.3 mm by 3mm and 640 lines per image. A movie named media 516 is attached to demonstrate the real-time images of human skin *in vivo* with extended DOF. The movie basically displays the process that the imaging system started acquiring images with confocal configuration (no phase modulation) and then switched to BPSF optimized system in the middle of the movie and switched back to confocal in the end.

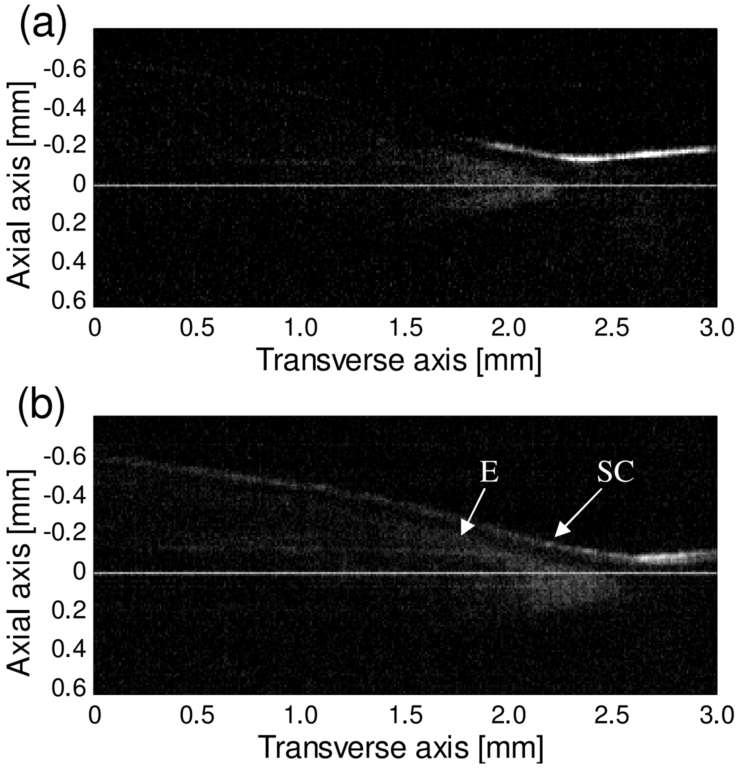

Fig. 5.16 Real-time images of human skin *in vivo* acquired with (a) the conventional system and (b) the BPSF II optimized systems.

The amplification in depth of focus is not as good as the theoretical prediction; the reason is that the extended depth of focus is compromised by the penetration depth of the BPSF optimized system, which is shortened due to a SNR loss of ~20 dB. This disadvantage can be compensated by use of a laser of larger power and decoupling the illumination and detection path in the sample arm. The detailed optical design for decoupling the illumination and detection path is proposed in Chapter 7.

## 5.5 Discussions and conclusions

### 5.5.1 Focal spot measurement

To optimize the filter performances, compromises are often made between filter properties. There could be numerous other designs available when one changes the searching criterion. For example, if axial intensity nonuniformity larger than -15 dB is acceptable, one would find many designs demonstrating DOF gains above 6 with the pupil radius defined by any power level. However, in our calculation and experiment, we choose filters with the best axial intensity nonuniformity to ensure a high-quality axial response for biomedical imaging applications.

It can be noticed that there are some difference between calculated diffraction pattern and experimental results, such as spot size, strength and symmetry of the side lobes. These discrepancies might be explained by aberrations brought about by the SLM. First of all, the nonuniformity of the SLM phase response affects the calibration accuracy of the device and thus the measured results, especially larger side lobe intensity of the measured data than the calculated data. Secondly, the effective image size of addressing video projector is about 200×200, so that the normalized pixel size of the phase mask is limited to 0.01. This limitation may be one of the reasons for the above mentioned differences.

### 5.5.2 OCT deep tissue imaging *in vivo*

To our knowledge, the current system is the first OCT system for super-resolution along an extended DOF. However, it is only a prototype for proof-of-principle study. Therefore, there are still technical problems in resolution and SNR with the current system, and improved optical design dedicated instrumentations are necessary to completely demonstrate the superiority of the proposed method over conventional method.

### Resolution

The objective lens (Nikon CFI Fluor 10XW, NA = 0.30, focal length 20 mm) provides a lateral resolution of ~2.5 μm; the light source offers an axial resolution of 9 μm (in water). This spatial resolution is equivalent to the size of a cell (4~10 μm), so that it is not enough to resolve individual cell in human skin. It might be hard to perceive resolution difference between the conventional case and BPSF optimized case without cellular level details.

A light source with much broader bandwidth or shorter center wavelength and a NIR objective lens with much higher NA would be sufficient to resolve individual cell and demonstrate the super-resolution of the BPSF optimized system. There are a few commercially available light sources that can provide cellular-level axial resolution; there are also many commercially-available high-NA NIR objective lenses. For light sources operating in telecom-band, an aberration-free objective lens can be designed and customized using commercial software and fabrication facility.

### Signal to noise ratio

The SNR demonstrated in Fig. 5.16 (a) is much lower than that of a standardized SSOCT [173]. The difference between the propose system and a standardized SSOCT is that additional optical components are inserted in optical path of the reference arm and sample arm of the current system, including a telecom-band polarizer, a liquid-crystal-based spatial light modulator, a NIR (but not telecom-band) objective lens, 4 SMF-28 batch cords to match the optical path-length and 3 aluminum coated mirrors to change the optical path. Both the polarizer and the SLM have a maximum power transmission rate of 70%; the NIR objective lens has a transmission rate of <60%; for each connection between two SMF-28 batch cords, the optical power loss is more than 0.1 dB; the reflection rate of the aluminum coated mirror is about 80% at 1300 nm. To calculate the round-trip SNR loss, this loss in optical power should be squared due to the double-pass configuration of both arms. In total, there is approximately SNR loss of >23 dB for the current system compared with the standardized SSOCT system.

Most of loss mentioned above can be avoided by improve optical design and dedicated components. For example, a binary phase plate can be easily fabricated by solid etching method [160] to replace the polarizer and the SLM. The material for the phase plate can be glass or semiconductor that is transparent for the designed wavelength range. By applying anti-reflection coating on the surface of the phase plate, the power transmission rate is expected be higher than 99%. A dedicated objective lens that is aberration free with high transmission rate for the designed wavelength might be commercially available or can be customized with commercial optical design software and fabrication facility.

### 5.5.3 Possible limitations

The possible limitations include above-mentioned power efficiency and susceptibility of transverse resolution and SNR to aberrations. The first limitation has been identified in section 5.4.2 and can be overcome by use of light source with higher optical power and decoupling the illumination and detection path in the sample arm. The detailed method to overcome this limitation will be discussed in Chapter 7.

The susceptibility to aberrations basically stands for the robustness of the optical field set up in the tissue sample, which may give rise to refractive-index-induced spherical aberration, wavelength dispersion, or even change of polarization. It is still unknown how susceptible the BPSF engineered PSF to all kinds of aberration compared with the conventional PSF. Quantitative study must be done on some tissue phatom with known optical aberration. The efficacy of the proposed method should be further verified with more tissue samples, for example human fat tissue.

## 5.6 Conclusion

In conclusion, a simple method to optimize the focusing condition using BPSF is presented. In the paraxial Debye regime, the dependence of filter performances on the Gaussian distribution in the pupil plane is characterized. Optimal filter designs are proposed for either high-resolution or ultra-large-DOF applications followed by experimental verifications. The DOF gain is independent of NA in the scalar regime. A BPSF is designed to optimize the focusing condition of a fiber-based real-time SS-OCM system, and the DOF is increased by a factor of 10.5 with a lateral resolution of 5.0 μm.

To our knowledge, this is the first time this important class of pupil filter is characterized experimentally under Gaussian approximation; and it is also the first demonstration of OCT imaging *in vivo* with extended DOF. Since binary phase masks can be easily fabricated and miniaturized, the merits of the proposed method should facilitate the development of high performance systems for in vivo imaging applications.

There are still technical problems to be solved and possible limitations to be identified and overcome. The specific methods to solve the technical problems and overcome the limitations will be proposed in Chapter 7. However, the current funding and workload might not support further investigation and developments, which might be done under additional support and in later stage of research.

# Chapter 6 Molecular and morphological imaging with dual-mode microscopy

## 6.1 Introduction

Molecular-specific contrast imaging in biology and medicine

Molecular-specific contrast mechanisms based imaging modalities, such as positron emission tomography [174], metallic ion-based magnetic resonance imaging [175] and fluorescence microscopy, have revolutionized biological research and clinical diagnosis. The capability to map out contrast agent distribution within a tissue sample provides biochemical specific and unambiguous information beyond the tissue morphology. Of these imaging techniques, fluorescence contrast microscopy stands out in terms of its ease of use, low cost and, most importantly, its wide applicability [176]. The family of fluorescence microscopy have been popularized in recent decades, including Forster resonance energy transfer (FRET) [177, 178], fluorescence correlation spectroscopy (FCS) [179, 180], total internal reflection fluorescence (TIRF) microscopy [181], stimulated emission depletion (STED) microscopy [182] , multi-photon fluorescence microscopy (MPFM) [183] and fluorescence lifetime imaging (FLIM) [184], fluorescence recovery after photo-bleaching (FRAP) [185]. Since the invention of antibody-conjugated fluorescence molecules [186], biologists have been able to tag specific protein type and study the protein function, protein transport and gene expression and regulation *in vivo*. The development of methods for expressing fluorescent protein, such as green fluorescent protein (GFP) [187-190], endogenously by genetic manipulation solidly cements the role of fluorescence contrast microscopy in biological research [176]. In the clinical environment, Food and Drug Administration (FDA) approved fluorescent dyes, such as indocyanine green (ICG) [191, 192] and fluorescein [193], have all found important applications.

Besides labeling the molecules with fluorophores, molecular contrast can also be provided by a variety of light-mater interaction mechanisms, including spectrally dependent absorption, Raman scattering [194, 195] and second harmonic generation (SHG) [196, 197], and coherent Anti-Stokes Raman Scattering (CARS) [198-200].

## Penetration depth limit of optical microscopy

One major disadvantage associated with optical imaging techniques for biomedicine is that they tend to have fairly shallow imaging penetration depth, which is attributed to the fact that biological tissues are highly scattering in the optical regime [176]. . The thickness of a biomedical tissue sample normally ranges from tens of microns to several millimeters, which is in the range of working distance of an optical microscope objective. However, the efficacy of deep tissue imaging through turbid medium is subjected to strong intensity attenuate and resolution degradation. The ballistic light decays exponentially as the optical thickness of a turbid medium becomes large, optical thickness

$$n = \frac{penetratoin\ depth}{scattering\ mean\ free\ pathlength}. \tag{6.1}$$

According to the imaging theory based on Born's approximation, which ignores the multiple scattering in a turbid medium, a high numerical-aperture objective lens can provide high diffraction-limited resolution. Born's approximation is applicable to the case in which the optical thickness is less than 1. This argument is based on the assumption that ballistic light is dominant in forming an image. When a turbid tissue is thick, e.g., n>10, unscattered light may be too weak to be detected, particularly in the presence of detector noise. In this situation scattered light has to be included in constructing an image. An important question raised here is what role the scattered light plays in constructing an image. It is found that, for a thick turbid medium, scattered photons have to be included as part of the signal in order for the noise level to be overcomes [201]; however, image resolution contributed by scattered photons is lower than diffraction-limited resolution. So, the disadvantage of the conventional microscope for imaging through thick object structures is that there is no or weak optical sectioning to suppress this background image (or multiply scattered photons), which can thus be strong for a thick object and can saturate the detector. In this respect, the ability of an optical microscopy to penetrate turbid tissue basically depends on its strength of sectioning or "gating".

### Confocal fluorescence microscopy and confocal gating

Confocal fluorescence microscopy (CFM) has been an important advance in microscopy history and has enabled the imaging of intact, optically nontransparent specimens to produce high resolution images. For a relatively thick specimen, CFM accomplishes optical sectioning by scanning the specimen with a focused beam of light and collecting the fluorescence signal via a pinhole aperture that spatially rejects light from out-of-focus areas of specimen. When images of optical sections that are deep within a turbid tissue are obtained using confocal microscopy, the fluorescence signal is attenuated by multiple scattering. Some fluorescence originating from regions away from the point being instantaneously illuminated will be scattered such that this fluorescence will pass through the confocal pinhole thereby increasing background noise. A fundamental limit to confocal imaging depth is then imposed when this out-of-focus scattered light produces noise that is greater than the in focus signal. This limit stands regardless of the available power and can be roughly approximated with a single-backscatter model. Confocal imaging therefore suffers deterioration in signal-to-background when obtaining images from deep within a sample. Meanwhile, out-of-focus photo bleaching prevent CFM from effective 3D or 4D imaging [202]. Additional or stronger gating methods must come into play when one is to penetrate deeper in highly scattering media.

### Two-photon fluorescence microscopy (TPEFM) and nonlinear gating

TPEFM is a technique that uses non-linear optical effects to achieve optical sectioning. In TPEFM, the sample is illuminated with a wavelength around twice the wavelength of the absorption peak of the fluorophore being used. Essentially no excitation of the fluorophore will occur at this wavelength. However, if a high peak-power, pulsed laser is used (so that the mean power levels are moderate and do not damage the specimen), two-photon events will occur at the point of focus. At this point the photon density is sufficiently high that two photons can be absorbed by the fluorophore essentially simultaneously. This is equivalent to a single photon with energy equal to the sum of the two that are absorbed. A key feature of TPEFM is the limitation of fluorescence excitation to within a femtoliter size focal volume. Fluorophore excitation will only occur at the point of focus, thereby eliminating excitation of out-of-focus fluorophore and achieving optical sectioning. There are a number of advantages of TPEFM. One prominent advantage of TPEFM over CFM is that the exciting photons are in the range of Near Infrared (NIR) which suffers much less scattering in the turbid tissue, so that it can penetrate deeper in to the tissue. The penetration depth varies based on the turbidity (scattering property) of the targeted tissue; a typical maximum depth penetration of about 300-400 μm can be expected for images that still preserves an axial resolution that is largely defined by the confocal parameter. Another important one is that due to confinement of multiphoton in a small volume, TPEFM only photo bleach the volume in focus, so that 3D and 4D imaging can be achieved [203].

### Optical coherence tomography and coherence gating

In terms of penetration depth, optical coherence tomography (OCT) compares very favorably with fluorescence-based or any other optically based imaging techniques; imaging depth of millimeters with spatial resolution comparable to confocal fluorescence microscope are relatively easily achieved with OCT at light fluence levels within the American National Standard (ANSI)-recommended limits [172]. OCT's superior depth penetration and ability to preserve high axial spatial resolution in thick highly scattering tissue is attributable to its ability to selectively detect only the ballistically propagating or components [204] of the backscattered light originating from a specific selectable depth within the sample. These components are the fraction of the light that are not scattered or suffer less scattering by the tissue. The ability of OCT to render high-quality three-dimensional structural images of biological targets noninvasively has propelled its rapid adaptation for clinical applications, most notably in imaging the anterior and posterior segments of the eye [205-209], vascular tissues [210, 211] and GI tracts [212-214].

**However, lack of molecular contrast is one of major drawbacks of OCT for biological research and optical biopsy.** OCT measures only physical entity of the sample, as a result a map of reflectivity or scattering coefficient provides only structural or morphological information which is nonspecific or ambiguous for functional study. Contrast enhancing mechanisms are needed to allow differentiation of tissue types that are morphologically or optically similar. Typical OCT cannot detect inelastically scattered light such as that emitted from fluorophores because such light is not coherent with respect to the incident field. OCT would greatly benefit from molecular-specific contrast enhancement, preferably fluorescence, to aid in deep tissue imaging.

## 6.2 Literature review

In Chapter 1, it has been identified that lack of molecular contrast is one of major drawbacks of OCT for biological research and some of clinical applications**.** There are generally two approaches to compensate for this drawback of OCT. Several research groups have implemented various modified OCT schemes that have the capability to detect molecular contrast agents or contrast agents that can potentially bind to a specific chemical or protein. A hybrid optical imaging approach that can combine OCT's ability to perform high-resolution and excellent penetration depth imaging with fluorescence contrast microscopy's ability to elicit molecular contrast from the sample can dramatically enhance the capability of clinicians and biomedical researchers to track biochemical distribution and changes within tissue samples in question.

### 6.2.1 Molecular contrast (enhanced) Optical coherence tomography (MCOCT) and its limitations

Pump-probe MCOCT [215] was the first reported approach for performing MCOCT imaging, in which an optical excitation field changes the absorption cross-section of the dye at the OCT probe wavelength by shelving the molecules into a relatively long-lived triplet state. The major challenge with this technique lies in creating a sufficiently fast OCT imaging system to acquire the OCT signal with the dye molecules in the short transition duration in their transition state. Pump-suppression MCOCT [216] is the next class of MCOCT seeks to address the above challenges associated with the short transition duration of the molecular contrast agents by choosing a slightly different molecular transition mechanics conformational change of molecules. However, unlike in the case for the previous method, the choice of molecular contrast candidates for this method is limited. Spectroscopic OCT [217-219] is based on the difference in absorption coefficient between the contrast agents, such as water, near-IR dye, and the surrounding tissue, so that the presence of the contrast agent in the tissue will tend to skew the spectrum of the backscattered light component by absorbing part of the input light spectrum. Nonlinear interaction based OCT [223] rely on the coherent nonlinear processes that can efficiently and coherently convert the incoming OCT probe light field into an emission that is detectable using interferometric approaches. Scattering based MCOCT uses engineered microspheres [224] and magnetic particles [225] as contrast agents. Both methods rely on creating a sizable sample reflectivity, with the presence of the contrast agent and correlating the size of the measured reflectivity signal to the contrast agent’s concentration.

The above mentioned MCOCT approaches have their own respective advantages. However, there are till several obstacles for these approaches to overcome for successful biomedical deep tissue imaging.

First of all, an ideal OCT-based molecular-contrast imaging modality should be able to image a wide range of contrast agents and be able to identify each contrast agent uniquely. What is more, it is extremely helpful when the simultaneous tracking of two or more chemical species within the sample is desired. Of the methods that we have discussed, only the CARS-OCT can meet these requirements owing to the high chemical specificity of CARS signal. Others have relatively restrictive range of possible molecular contrast agent choices [176].

The second obstacle is the light fluence limits. The first limit is set by the threshold of irreversible cell damage and is applicable in the context of deep tissue imaging that does not involve human subjects. The second limit is set by the clinical safety guidelines issued by ANSI for the use of lasers on human subjects [172]. CARS-OCT exceeds the first threshold slightly. SH-OCT and CARS-OCT methods exceed the ANSI limit by an order of magnitude.

### 6.2.2 Dual-mode microscopy

It is a simple idea to build a hybrid optical imaging approach that can combine OCT's ability to perform high-resolution and excellent penetration depth imaging with fluorescence contrast microscopy's ability to elicit molecular contrast from the sample. A dedicated dual-mode microscopy with combined molecular and morphologic contrast machanism can dramatically enhance the capability of clinicians and biomedical researchers to track biochemical distribution and changes within tissue in question.

E. Beaurepaire *et al* reported the first combined scanning OCM/TPEFM in 1999 [226]. Because the coherence length of Ti: sapphire laser was 15 μm, the intrinsic OCT axial resolution was not matched with the TPEFM channel (2 μm). In order to improve the axial resolution of the OCT channel, a pinhole was inserted into the beam path before the OCT detector; however, such a pinhole does not substantially improve the axial resolution for deep tissue imaging. The lateral resolution for both channels was 0.4 μm. The optical power incident on the sample was < 10 mW, resulting in a sensitivity of 130 dB at a pixel rate of 100 kHz.

Z. P. Chen et al employed a source with a much shorter pulse duration (12 - fs) and broader bandwidth [227]. Under these conditions, the coherence length of the light source is matched with the TPEFM axial resolution (0.5 μm for transverse and 1.5 μm for axial resolution). Such feature is tested on an organotypic RAFT tissue model. The RAFT model consists of a basic polymerized collagen gel made up of type-I rat-tail collagen and primary human neonatal dermal foreskin fibroblast cells.

S. A. Boppart's group developed an integrated OCM/TPEFM system roughly about the same time as UCI group [228]. Fourier domain schematic was used instead of time domain one; the Fourier domain setup demonstrates a signal to noise ratio of 100 dB at a line acquisition rate of 29 kHz. The axial and transverse two-photon resolutions are 0.8 and 0.5 μm respectively; the confocal gating (confocal parameter=2.2 μm) from the high numerical aperture objective was shorter in distance (higher axial resolution) than the coherence gating (coherence length = 4.7μm) from the broad 60 nm spectral bandwidth of the laser source. A transverse resolution of 0.9 μm was measured for the OCT channel.

TPEFM is an ideal molecular-contrast imaging modality that can be combined with OCM in terms of spatial resolution and penetration depth. However, TPEFM necessitates the use of a cost inhibiting femto-second laser; Moreover, unlike confocal fluorescence microscopy which is based on one-photon process, the available fluorophores that have high two-photon cross sections are limited [177]. TPEFM then finds itself hamstrung by the choice of the fluorophores it could utilize. These factors preclude its wide application in biomedical research and clinical diagnosis. **A fluorescence microscopy based on one-photon process with additional sectioning capacity other than confocal will be more pertinent than TPEFM to provide molecular contrast in a dual-mode instrument.**

### 6.2.3 Focal modulation microscope (FMM)

FMM is an optical heterodyne technique working in a confocal framework. FMM can provide additional optical sectioning besides confocal gating based on either one-photon or multi-photon fluorescence process; therefore it is an ideal molecular-contrast imaging modality that can be combined with OCM for dual-mode imaging.

Shown in Fig. 6.1, the schematic of FMM is identical to confocal fluorescent microscope except that the objective aperture is splitted into two different half apertures. The phase of source excitation light which goes through one of the half apertures is modulated by an optical phase modulator, while the other half acts as a reference. According to the diffraction theory, the two half beams are spatially coherent only in the confocal focal volume, resulting in the maximum interference at the geometrical focal spot and strong attenuation of interference signal out of the confocal parameter. Due to a varying spatial phase distribution, the excitation beam entering the objective aperture does not necessarily converge to the focal point. Consequently, an intensity modulation of the excitation light is achieved around the focal point. When the focal point is within a turbid medium, the excitation photons reaching the focal plane include both ballistic and scattered photons. Only the ballistic photons contribute to oscillatory excitation rates as they have well defined phase and polarization. The oscillatory excitation rate is in-phase with the modulation signal inside a small focal volume and out-of-phase elsewhere. In the case of fluorescence labeled specimen, only light emitted from the fluorescence at the focal region will exhibit a light intensity which is modulated with the source modulation frequency. In the out of focus region which is only being illuminated by one of the half beam, will not exhibit such modulated fluorescence intensity. This could then be simply removed through post filtering techniques. Essentially, additional sectioning or “optical gating” besides confocal gating is achieved, so that rejection of multiple scattered photon or background imaging is much more effective than confocal gating alone.

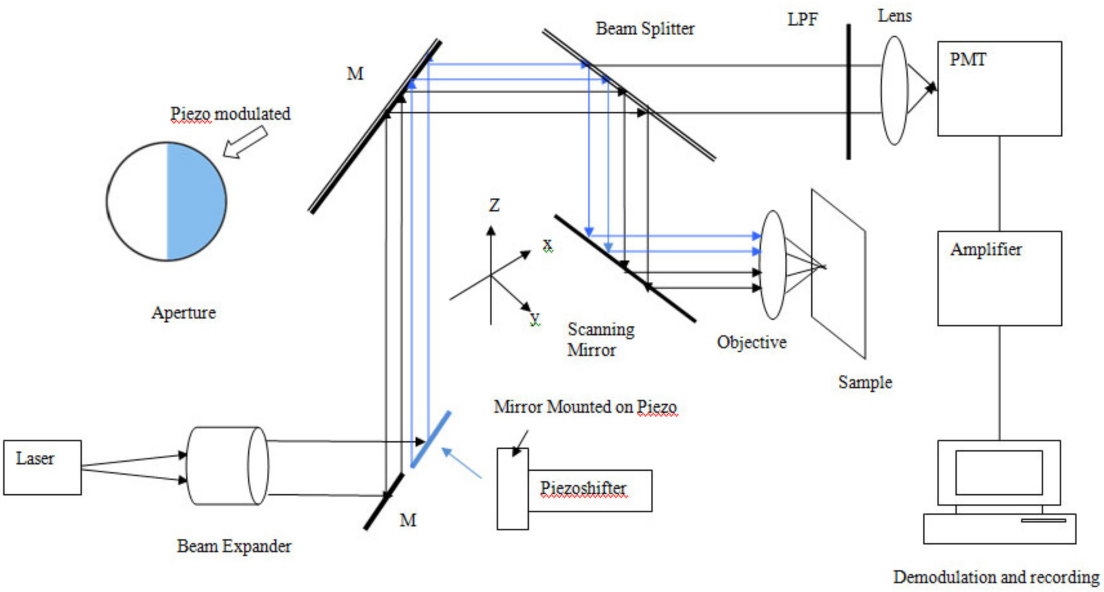

Fig. 6.1. Schematic of FMM.

The confocal pinhole defines a small focal volume for detection from which emissions are collected. Out-of-phase oscillatory emissions, mainly originating from regions out of the focal volume. Since the light of two half beams are coherent, the effective numerical aperture of FMM should be defined by the combined aperture of two half beams. From the two-dimensional distribution of the differential excitation power in the focal plane [230], it can be seen that the lateral spot size is essentially the same as the confocal one.

## 6.3 Materials and Methods

A novel dual-mode microscopy is proposed for molecular-specific and morphology contrast *in vitro* deep tissue imaging [229]. A novel microscopic technique, named focal modulation microscopy, a pending US patent of Dr. Chen Nanguang, Dr. Colin Sheppard and Mr. Wong Chee Howe [230], is adopted to provide molecular contrast with a penetration depth equivalent to OCT. An integrated dual-mode microscope has been developed combining the focal modulation microscope and a swept source OCT/OCM. *In vitro* imaging has been performed on thick tissue samples like chicken cartilage. The integrated instrument allows mapping of morphology image to the fluorescent imaging so that structural and functional correlation of the tissue can be studied in cellular level.

**Optical design**

In order to build a dedicated instrument that combines molecular and morphology contrast, a collinear dual-mode setup, shown in Fig 6.2, is constructed. The OCM subsystem is shown in the purple box. A high-speed frequency swept external cavity laser (SL1325, Thorlabs, Inc.) is used to provide broadband light in the 1260~1390 nm wavelength range, yielding a coherence length of 12 μm in air. The structure of the fiber-based OCM is essentially a Michelson interferometer. The system uses a circulator and dual balanced detection scheme. The optical circulator couples the light returning toward the source arm to a detector (except for an approximately 0.85-dB insertion loss), effectively doubling the signal power. A balanced differential detector (Thorlabs, PDB140C 15 MHz) is used to combine the signals while simultaneously rejecting common mode noise that is due to source-intensity fluctuations. The axial scans (A-scans) are performed at 16 kHz, same as the frequency swept speed of the laser. The transverse scans (B-scans) are performed at 17-26 Hz, which is controlled by a dual-axis fast steering mirror and determines the frame rate of the OCT imaging. With an A-line repetition rate set at 16 KHz, the B-scan frame rate is 25 Hz with 640 A-lines per frame.

In the sample arm the optical beam is collimated by a near-IR achromat L2 with a focal length of 30 mm and passes a dichroic mirror (DM2), and goes to the dual-axis fast steering mirror. The beam is relayed to an infinity corrected objective lens (Olympus UPLAN, 0.45NA, 20X, infinity corrected with correction collar). In the reference arm, the APC connectorized fiber is attached with a fiber collimation package (Thorlabs FC260-C) to convert the light to collimated beam. The reference mirror is an aluminum coated mirror. The optical delay of the reference arm is made adjustable by use of a translation stage. The reference arm reflectivity is controlled by appropriate attenuation.

The digitizer (ATS460, AlazarTech.) samples the laser trigger / *k* space clock and OCT signal simultaneously at 50 MHz. After Fourier Transforming of the recalibrated OCT interference fringe signals, the depth-dependent reflectivity profiles of the sample are generated and displayed. The computer also generates waveforms through an analog output board to command the XY scanner driver that controls the XY beam scanner in the microscope head to synchronize two-dimensional and three-dimensional imaging of the sample. The B-mode frame rate for the OCT subsystem is 21.6 Hz. Therefore it takes 30 s to acquire a three dimensional data set of $640\times640\times512$ points.

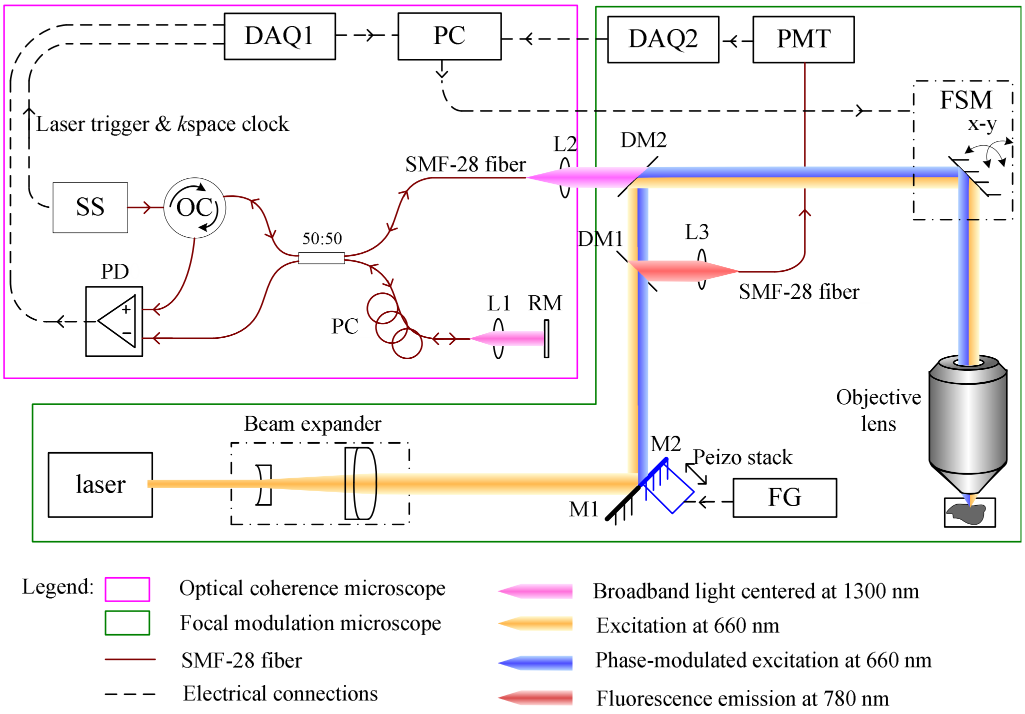

Fig. 6.2 Schematic of dual-mode microscope. SS: swept source; OC: optical circulator; PC, polarization controller; RM: reference mirror; PPM: programmable phase modulator; FSM: fast steering mirror; PD: photodetector; DAQ1 and DAQ2: data acquisition devices; PC: personal computer; PMT: photon multiplier tube; FG: function generator; DM1, DM2: diachroic mirrors.

The theoretical transverse focal spot sizes are 0.8 μm and 1.5 μm for FMM/CFM and OCM respectively; the theoretical confocal parameters are 5 μm and 9 μm for FMM/CFM and OCM respectively. Here the confocal parameter matches the coherence length of the swept source. Note that in contrast with standard confocal microscopy, OCM detects the backscattered electric field rather than the intensity that is returning from the sample. Thus the (normalized) envelope of the axial response of an OCM should be the square root of that of a standard confocal microscope, assuming that the reference beam detection is not itself confocal. In our case, the interferometric signal is squared after detection, which means that our apparent axial response turns out to be identical to that of a confocal microscope and the difference in theoretical resolution between FMM/CFM and OCM are mainly due to different operating wavelength.

Shown in the green box, the FMM subsystem is combined to the OCM subsystem by sharing the same scanning device and objective lens. Laser beam (660nm, 5 mW B&W Tek) is first expanded using a beam expander and is then spilt into two half apertures formed by placing two square mirrors that are placed beside one another and aligned closely to reduce distance and angular variation. In one of the half aperture mirror, a piezo-stack (NEC AE0203D04) is attached. In operation mode, a driving signal of 5 kHz sinusoidal wave is generated by a function generator to drive the piezo-stack to generate the phase shift in the wave-front. The beam is then focused onto the specimen via the objective lens. Reflected light from specimen is collected and coupled into a PMT with an achromatic doublet lens. The electrical signal output is then transferred to the computer and digitally acquired through a DAQ card (Labview NI). The heterodyne signal is then retrieved after demodulation of the digitized signal acquired. Note that when no half beam is phase-modulated, the FMM subsystem is essentially a CFM, so that CFM can also be acquired with our setup for comparison and verification.

### Sample preparation and deep tissue imaging

#### Schefflera Arboricola (OCM and FMM) and onion skin (OCM)

Schefflera Arboricola was obtained from freshly plucked leaves. Onion skin was obtained from local market. Three-dimensional volumetric images were captured with OCM using an objective lens (Olympus UPLAN, 0.45NA, 20X, infinity corrected with correction collar). 2D morphological images of Schefflera Arboricola were also compared with Chlorophyll autofluoresence images acquired previously in Ref. [229].

### PCL nano-fiber (OCM only)

Three tissue engineered samples were obtained from Prof. D. W. Hutmacher (Tissue Engineering lab, Division of Bioengineering, NUS). The samples are composed of electro-spun PCL (polycaprolactone), PCL-collagen and PCL-gelatin fibers, respectively. The diameter of the fiber ranges from 300 nm to 800 nm, and thickness of the tissue was estimated to be ~ 0.15 mm. A coverslip was placed on top of the sample to hold the sections in place together with a glass-slide. For high resolution OCM imaging, an infinity-corrected objective lens (Olympus UPLAN, 40X, 0.65NA) was used to provide a transverse resolution of 0.9 μm and longitudinal resolution of 4.3 μm. The images acquired with OCM were compared with reflectance images acquired by use of an Olympus IX71 upright microscope with the same objective lens.

### Rat liver tissue

Normal Wistar rat liver tissues (fixed) were obtained from Prof. Hanry Yu's lab at Institute of Bioengineering and Nanotechnology. Tissue samples were sectioned by use of a scalpel, so that the size of the specimens is 8 mm×8 mm×0.5 mm. The tissue specimens were mounted with Gel Mount$^{TM}$ Aqueous Mounting Medium (G0918, Sigma) in specially made glass-slide chambers underneath glass-coverslips.

### Chicken cartilage (FMM and collinear OCM/FMM)

The animal tissue used for *in vitro* dual-mode imaging was chicken cartilage. Tissue samples were sectioned by use of a scalpel, so that the size of the specimens is 8 mm×8 mm×0.5 mm (length × width × thickness). The specimens were then labeled with lipophilic tracer - dialkylcarbocyanine (DiR, D12731 Molecular Probes, Inc.). DiR (D12731) is widely used as anterograde and retrograde neuronal tracers in living and fixed tissues and cells. The major advantage of carbocyanines is that tracing experiments can be carried out in human tissues. DiR (D12731) has excitation maximum at ~750 nm and emission maximum close to near infrared region (~780 nm), where many tissues are optically transparent. A protocol was worked out for thick tissue labeling and imaging. The experimental procedures with chicken cartilage were approved by the Institutional Animal Care and Use Committee (IACUC) of National University of Singapore.

1) Stock solution of DiR is prepared in ethanol at 1 mg/mL.
2) As soon as the animal is sacrificed, tissue samples were sectioned by use of a scalpel, so that the size of the specimens is 8 mm×8 mm×0.5 mm; perfusion-fixation with 4% paraformaldehyde in 0.1 M phosphate buffer (pH 7.4) [231, 232]. Postfix tissues in the same fixative overnight to 2 days at 4°C [233].
3) Storage during the time required for diffusive labeling of the tissue (typically 1~3 weeks) can be at 4°C.
4) The tissue samples are rinsed with ethanol to remove excessive dyes before they are mounted with Gel Mount$^{TM}$ Aqueous Mounting Medium (G0918, Sigma) in specially made glass-slide chambers underneath glass-coverslips.
5) The focus position and penetration depth of the collinear system is determined by the real-time OCT cross-sectional imaging. Two-dimensional fluorescence images

(FMM/CFM) and three-dimensional OCT reflectance images are acquired simultaneously and collinearly.

## 6.4 Preliminary results

### 6.4.1 3D volumetric deep tissue imaging with standalone OCM

Human skin

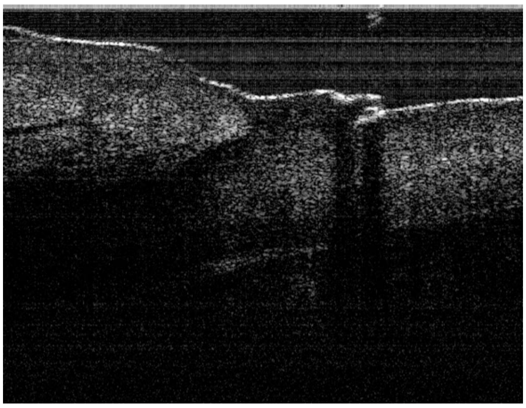

Fig. 6.3 Human skin *in vivo* in the nail fold region Image size: 3 mm by 3 mm.

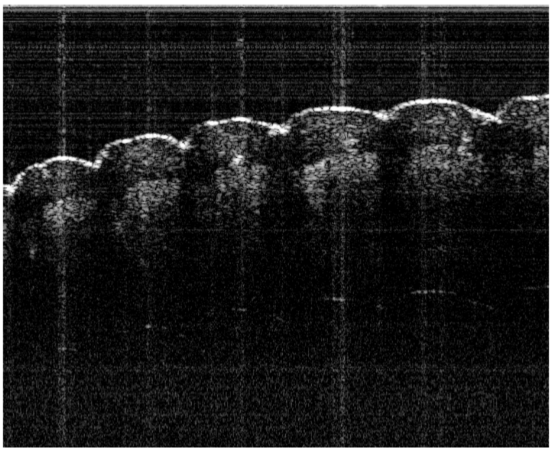

Fig. 6.4 Human skin *in vivo* in the finger (bottom). Image size: 3 mm by 3 mm.

Using an achromat (focal length = 40 mm) as the objective lens, a depth of focus as large as 3 mm in air can be achieved. In this case, real-time 2D images of the tissue sample within a full range of depth of 2 mm in tissue space can be acquired. Shown in Fig 6.3 and Fig. 6.4 are images of human skin *in vivo* in the nail fold region and finger respectively. These images basically demonstrate the penetration depth of the OCM system in highly scattering human tissue. The whole 3D volumetric data can be viewed in the media 63.

Schefflera Arboricola and onion skin

Fig. 6.5 (a) shows an *en face* image out of three dimensional data acquired with real-time SSOCM. Cell wall and nuclei are clearly identified at penetration depth of 100μm in air. When the OCM image is compared with FMM image of the same sample (not exact same location), it is found that cellular structures (cell wall and nucleus) present in OCM images can not be detected in FMM image; at the same time OCM can not identify the chlorophyll which provides nature contrast for FMM. It is a simple example demonstrating that the information provided by the two modalities is complimentary. The whole 3D volumetric data can be viewed in the media 65. In addition, a whole 3D volumetric data of onion skin can be viewed in the media 66onion.

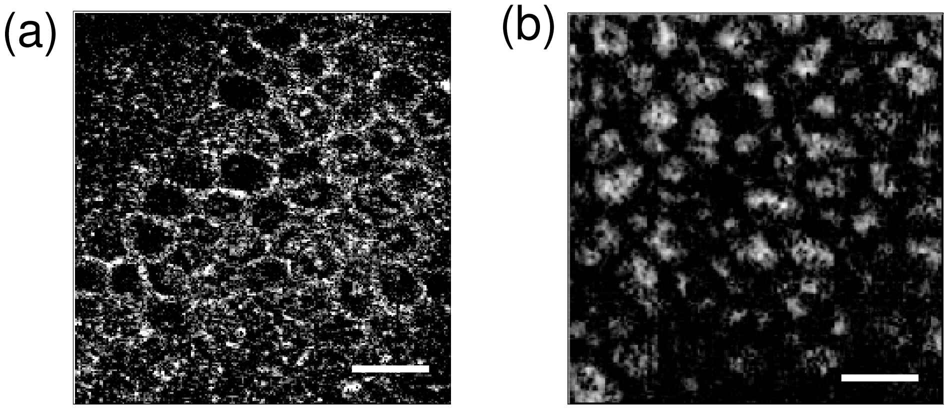

Fig. 6.5 Schefflera Arboricola (a) en face OCM image at depth of 100 μm in air; (b) Chlorophyll autofluoresence image acquired with FMM at depth of 160 μm. Scale bar: 30μm.

## PCL nano-fiber

Individual fiber is clearly identified for PCL tissue (Fig. 6.6 (a) and Fig. 6.7), which is verified by confocal reflectance imaging (Fig. 6.6 (b)). Fig. 6.6 and Fig. 6.7 demonstrates that spatial resolution of our SSOCM system is equivalent to that of a standard confocal microscope. There no difference found in OCM images of tissue composed of PCL, PCL-collagen (not shown here) and PCL-gelatin (not shown here), indicating that the OCM cannot detect molecular differences between these tissues. The whole 3D volumetric data can be viewed in the media 66.

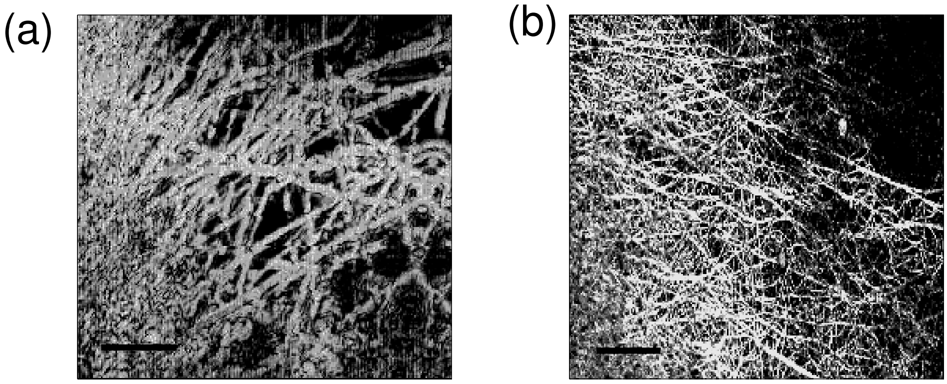

Fig. 6.6 (a) OCM image of PCL fibers, scale bar: 10μm; (b) Confocal reflectance image of PCL fibers, scale bar 20μm.

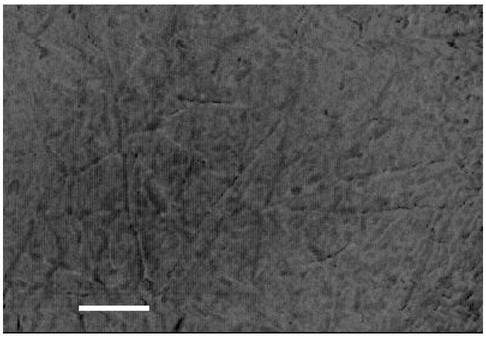

Fig. 6.7 (a) OCM image of PCL-gelatin fibers, scale bar: 10μm

## Rat liver

Fig. 6.8 shows OCM sequential images of normal rat liver tissue at penetration depth from 140 µm to 170 µm in tissue if a tissue refractive index of 1.38 is assumed. In the OCM images, cells (mainly hepatocytes) are indicated by dark spots because the cytoplasm is non-scattering; small blood vessels are also identified as dark holes which continuously appear along a large axial distance as indicated by the arrows. The bright region around the cell indicates localization and density of scatterers with are mainly contributed by the cell membrane, connective tissue and extra-cellular matrix proteins including collegan. Some cells may be seen in two sequential planes, while others are clearly seen in one of the planes and become obscured or even disappear in the ajecent plane. The whole 3D volumetric data is shown in media 68.

### 6.4.2 Fluorescence imaging with FMM/CFM

Figs. 6.8 (a) and (b) shows shows CFM and FFM images of chicken cartilage. Individual cell is clearly differentiated in both CFM image and FMM image at penetration depth of ~200 µm in tissue if a tissue refractive index of 1.38 is assumed. The FMM image shows a high spatial resolution equivalent to that of CFM, while much better background rejection is demonstrated in the FMM image. Indicated by the large arrow, the contrast of the confocal image is degraded by the signal of scattered fluorescence originating from out-of-focus cells, which is effectively suppressed in the FMM image; Indicated by the small arrow, some parts of the confocal image are blurred due to superposition of the fluorescence light from the focal plane and locate above or below the focal plane, while in the FMM image, the resolution and contrast of the image are restored owing to a stronger section ability of the FMM than CFM.

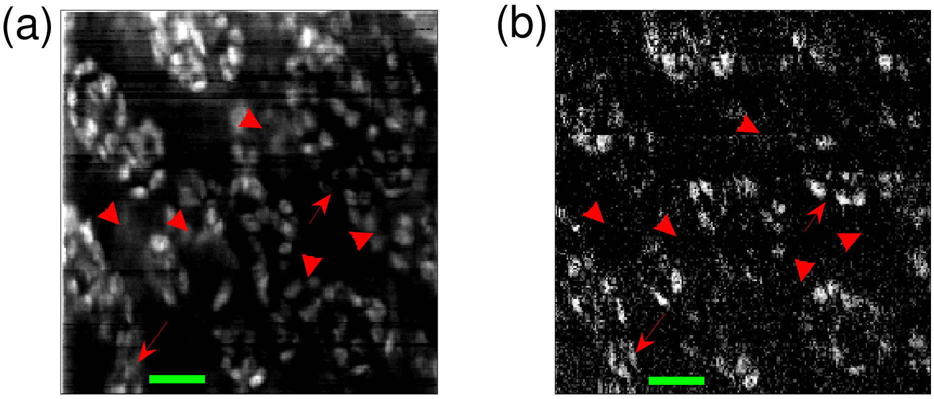

Fig. 6.8 Images of chicken cartilage at the same location acquired with (a) CFM and (b) FMM at depth of 276 μm in air. Scale bar: 30μm.

### 6.4.3 Dual-mode microscopy

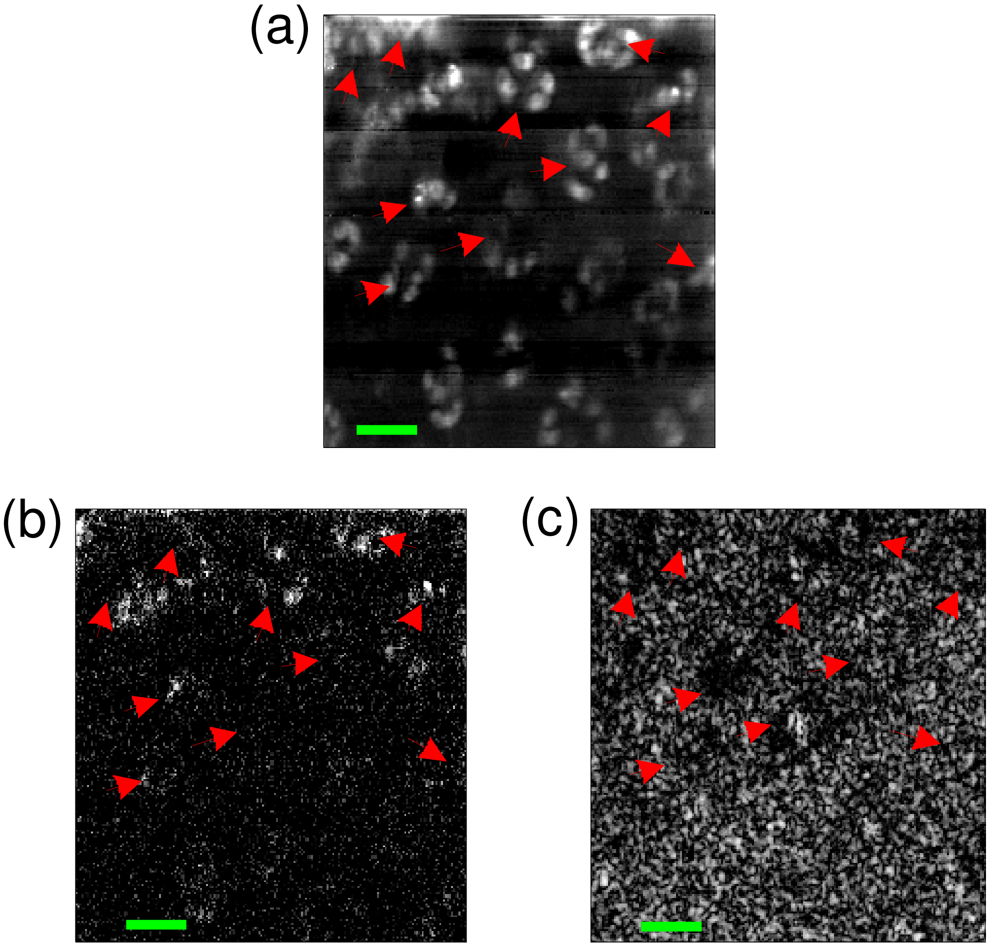

Fig. 6.9 Images of chicken cartilage at the same location acquired with (a) CFM and (b) OCM at depth of ~300 µm in air. Scale bar: 30µm.

Fig. 6.9 shows collinear CFM, FFM and OCM images of chicken cartilage at penetration depth of ~217 µm in tissue if a tissue refractive index of 1.38 is assumed. In the CFM imaging (Fig. 6.9 (a)), cells are show as bright spots since the cell membrane is stained with the lipophilic tracer, and several cells form a ring like cell cluster (indicated by the arrow); The FMM image (Fig. 6.9 (b)) shows a high spatial resolution equivalent to that of CFM, while much better background rejection is demonstrated in the FMM image. In the FMM image, the resolution and contrast of the image are restored owing to a stronger section ability of the FMM than CFM. In OCM image (Fig. 6.9 (c)), cells are identified as dark structures because the cytoplasm is non-scattering, and structures with relative high scattering coefficient appear in the center of the cell cluster. However, the depth of focus of OCM is almost twice as large as that of the FMM due to both the coherence length and confocal parameter, so that the cellular structures that are out of focus and rejected in FMM image appear in OCM image. The whole 3D volumetric OCM data can be viewed in the media 69.

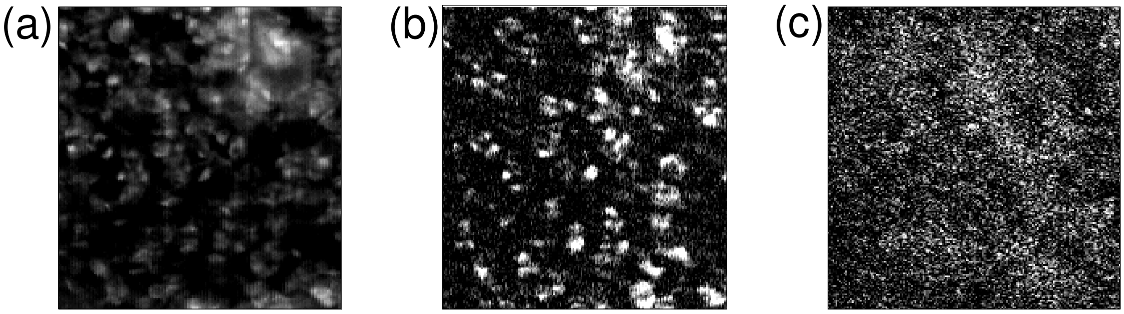

Fig. 6.10 Images of chicken cartilage at the same location acquired with (a) CFM (b) FFM and (c) OCM at depth of ~390 µm in air. Image size: 200 µm by 200 µm.

Fig. 6.10 shows collinear CFM, FFM and OCM images of chicken cartilage at penetration depth of almost 300 µm in tissue if a tissue refractive index of 1.38 is assumed. In the CFM imaging (Fig. 6.10 (a)), Cells are show as bright spots since the cell membrane is stained with the lipophilic tracer, and several cells form a ring like cell cluster. The FMM image (Fig. 6.10 (b)) shows a high spatial resolution equivalent to that of CFM, while much better background rejection is demonstrated in the FMM image. In the FMM image, the resolution and contrast of the image are restored owing to a stronger section ability of the FMM than CFM. In OCM image (Fig. 6.10 (c)), cells are identified as dark structures because the cytoplasm is non-scattering, and structures with relative high scattering coefficient appear in the center of the cell cluster. The whole 3D volumetric OCM data can be viewed in the media 610.

## 6.5 Discussions

As a pilot study, our collinear system is still in its early stage of development. For our current collinear system, individual cells in animal tissue can be clear identified *in vitro*, but detection of sub-cellular structure might need lens of higher resolving power and thus better refractive index matching and dispersion correction measures.

The FMM subsystem is the first prototype since its invention and the main problems with it are that the scanning speed is relative low (30 second per frame) and the finge signal (heterodyne signal) is not stable owning to the performances of piezo based phase modulator. The main problem with OCM subsystem is that the sample arm optics is not optimized for OCM, so that both SNR and spatial resolution are much lower than the standalone system. The specific reasons are listed as follows:

1) Due to a low transmission (one way <50%) in telecom band of the objective lens

(UPLAN Olympus 20X), there was a SNR loss of more than 4 dB solely caused by the objective lens.

2) The objective lens in use is not corrected for a broadband source, especially in telecom band (1300 nm) which is far away from its designed working wavelength range (around 400-800 nm), so that the resolution and signal strength must be degraded by  wavelength dispersion.
3) In addition, the wavelength for OCM is almost twice as that of FMM system, further degrading the resolution of the SSOCM subsystem by a factor of more ~2.

To address problems 1) and 2), a dedicated objective lens should be costumized with the above mentioned aberrations corrected properly, since there seems no suitable commercial objective lens. The problem 3) can be solved only by replacing the current light source of 1300 nm with a source of much shorter wavelength, for example 800 nm.

Of course, there are many other problems with the system and imaging procedure. For FMM, deep tissue staining might be a big issue because efficiency of deep tissue staining by diffusion is very low, so that there might be much less fluorescence molecules localized in deep locations than in shallow locations. The penetration depth can be further improved with excitation light of longer wavelength [234]. However, only can superiority of FMM over CFM be full recognized when we use a fluorescence dye which is commonly used in CFM (such as one of the green fluorescence dyes) on an established animal model, and compare the results with those produced by a standard commercial confocal microscope. For OCM, the speckle noise is a big issue since the resolution and imaging contrast is mainly degraded due to speckle noise. Incoherent averaging (also call compounding) can be adopted to suppress the speckle noise.

The system is the first prototype for the proof-of-principle study, and far from optimized. The next prototype should be built based on a commercial microscopic platform, for example, a commercial confocal microscope, and it is believed to be accomplished under a new grant. More advanced animal tissue models or engineered tissues should be adopted to test the enhanced resolution and signal strength of next prototypical system. An animal model and corresponding staining protocol is recommended in Chapter 7.

## 6.6 Conclusion

In conclusion, we have tested our OCM subsystem on some simple tissue models like onion skin, Schefflera Arboricola and PCL nano-fiber scaffold; the results indicate that the transverse resolution of OCM is as good as the confocal microscope, can be used to resolve sub-micron structures. We have also shown that OCM can resolve subsurface micro-structures of an advanced tissue model, rat liver, such as cells and small blood vessels.

It has been demonstrated on chicken cartilage the superiority of FMM over a home-made CFM in terms of sectioning ability. The resolution and contrast of the image are restored owing to a stronger section ability of the FMM than CFM.We expect the same superiority will be observed on a commercial microscope platform using commonly used fluorescent dyes.

A prototypical collinear dual-mode imaging system combining CFM/FMM and OCM has been developed. Preliminary results on chicken cartilage demonstrate the feasibility of coupling molecular-specific contrast and anatomical imaging based on independent contrast mechanisms derived from fluorescence and back-scattered light.

Simple functional and structural correlation on chicken cartilage samples has been successfully demonstrated. Both imaging techniques provide micrometer resolution and allow deep imaging of 300 µm in biological tissue.

# Chapter 7 Conclusions and Recommendations

## 7.1 Conclusions

This thesis proposes and validates a few novel methods to address fundamental and practical problems that prevent an emerging bioimaging tool from successful application *in vitro* and *in vivo*. To summarize, we have

1) Developed the double-pass RMA by including a specially designed retro-reflector and an interferometer in the optical path. The novel design presented solved the last crucial problem keeping RMA from practical use in an OCT system. A sufficient scanning range (greater than 3 mm) for OCT has been achieved with uniform optical coupling and high delay repeatability. Inheriting the original advantages such as high linearity, high repetition rate, constant scanning speed, and minimal dispersion, the double-pass RMA has become nearly ideal as a fast scanning optical delay line.
2) Developed a simple, high-speed, high-efficiency, high-duty-cycle, path-length maintaining and linear beam scanner is proposed for *en face* scanning optical coherence microscopes. A line scanning rate of 30 kHz and a scanning range of ±1.2° can be readily achieved with a DC motor of 60,000 rpm, a mirror pair number of 30 and a scanner diameter of 100 mm. The proposed scanner facilitates dual-mode imaging, for instance, optical coherence / multi-photon microscopy or optical

coherence / focal modulation microscopy to achieve real-time simultaneous molecular-specific and morphological contrast deep tissue imaging *in vivo*.

3) Presented a simple method to optimize the focusing condition using BPSF. In the paraxial Debye regime, the dependence of filter performances on the Gaussian distribution in the pupil plane is characterized. Optimal filter designs are proposed for either high-resolution or ultra-large-DOF applications followed by experimental verifications. A BPSF is designed to optimize the focusing condition of a fiber-based real-time SS-OCM system, and the DOF is increased by a factor of 10.5 with a lateral resolution of 5.0 μm. Since binary phase masks can be easily fabricated and miniaturized, the merits of the proposed method should facilitate the development of high performance systems for in vivo imaging applications.
4) Developed a prototypical collinear dual-mode imaging system combining CFM/FMM and OCM has been developed. Preliminary results on chicken cartilage demonstrate the feasibility of coupling molecular-specific contrast and anatomical imaging based on independent contrast mechanisms derived from fluorescence and back-scattered light. Simple functional and structural correlation on chicken cartilage samples has been successfully demonstrated. Both imaging techniques provide micrometer resolution and allow deep imaging of 300 μm in biological tissue.

As prescribed in the scope of the study in Chapter 1, this thesis has completed the fundamental studies to demonstrate technical feasibility, basic laboratory prototype development and preliminary feasibility studies on the established tissue models. Advanced laboratory prototypes with commercial grade performances may require advanced system design, component fabrication and instrumentation. Feasibility studies on advanced tissue models are expected to evaluate the potential challenges with the proposed methods for widespread applications.

## 7.2 Recommendations

### 7.2.1 Spectrally dispersing detection scheme for ultra-fast en face scanning OCM

As is identified in Chapter 1, the third drawbacks of FD-OCT is not capable of fast *en face* scanning OCM, since the A-line scanning rate is eventually limited by the acquisition speed of available linear CCD; it is also identified in Chapter 2 that the sensitivity advantage of FD-OCT over TD-OCT is use of spectrally dispersing detection scheme. It is wise to replace single element detection scheme of a TD-OCM with spectrally dispersing detection scheme. As Fig. 7.1 shows, interference signal from the interferometer (not shown here) is spectrally dispersed by a pair of identical gratings or optical de-multiplexers [235], and each element of the photodiode array only detects the signal within a narrow bandwidth. Since the signal in each channel is band-pass filtered separately, so that theoretically the shot noise can be reduced to $1/n$, in which $n$ are element number of multi-element detector [24]. Since for each element in the photo-detector array is equivalent to the single element one, essentially, the imaging acquisition speed can be as fast as the typical TD-OCM and the SNR improvement can be as good as FD-OCM with equal photo-detector array size.

Spectrally dispersing detection scheme is a natural part of FD-OCT, that is, the system which employs such a scheme is a Fourier domain system. Using of such a high speed detection scheme in FD-OCT makes possible fast three-dimensional imaging, or four-dimensional (time lapsed three spatial dimensions) imaging. However, such a scheme can be used in time domain system if the reference light beam is phase modulated at the optical path-length equivalent to that of the sample in question.

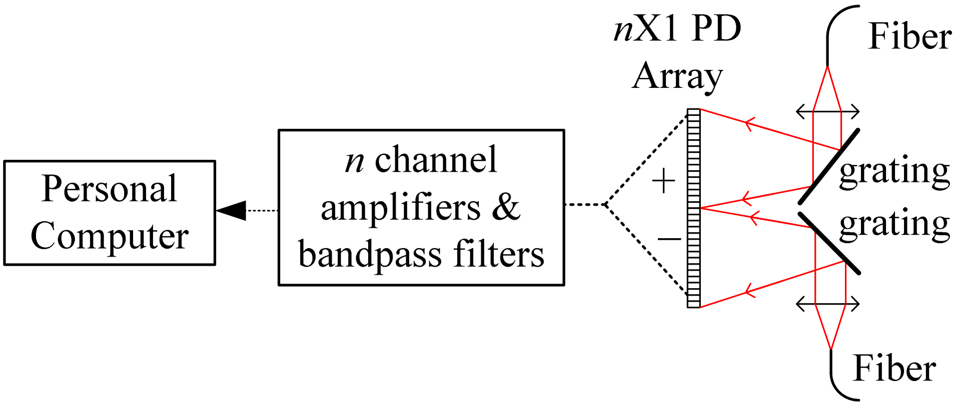

Fig. 7.1 spectrally dispersing detection scheme

### 7.2.2 Improved design for super-resolution along extended DOF

As is discussed in Chapter 5, one of the possible drawbacks of focus optimization with BPSF is much lower power efficiency compared to the conventional focusing scheme. This drawback can be relieved by decoupling the illumination and detection path in the sample arm. Shown in Fig. 7.2, in the sample arm optics the illumination path and the detection path is decoupled by a polarizing beam splitter, so that only the illumination beam is spatially phase modulated. The theoretical intensity point-spread function will be the product of the binary-phase spatial filtered illumination field and a Gaussian detection field. As a result, the SNR loss due to the binary-phase spatial filtering in the detection path is avoided and the total SNR loss is square root of the double-pass case. In addition, the side lobes caused by the spatial filtering can be effective suppressed by the Gaussian pinhole of the fiber entrance in the detection path [5.23].

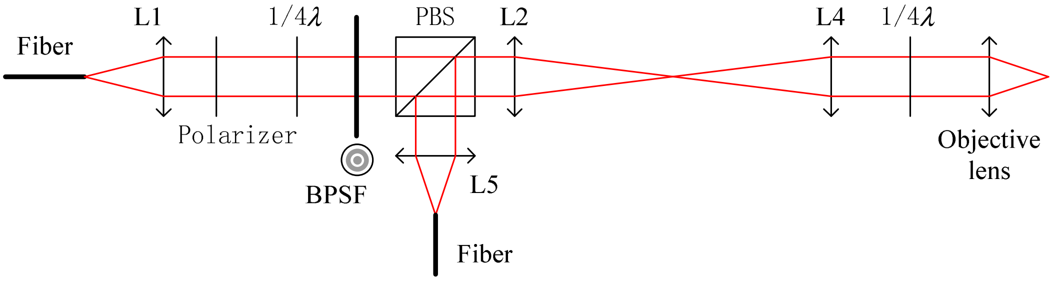

Fig. 7.2 decoupling the illumination and detection path in the sample arm in the sample arm of a BPSF optimized OCT system. PBS: polarizing beam splitter; 1/4λ: quarter wave plate.

### 7.2.3 Technical recommendations

Use of board-band light source

An ideal light source should have enough output power (more than a few mW) and operates in the near-IR region. The key parameters also include a board bandwidth, typically 1/4 of the wavelength. The pulsed lasers at 800 nm are common choices for a high axial resolution. However, they are expensive especially for application purpose. There are also commercially available ultra-broad bandwidth SLDs, such as superluminescent diode array which has a bandwidth of 1/4 wavelength at ~870 nm.

Coated APC pigtailed fiber tip for the highest SNR and energy efficiency

Optimal interferometers should utilize all available optical power for imaging while controlling the intensity on the detector by redirecting, rather than attenuating, light. Because there is around power loss of several percents at each fiber tip due to reflection, coating on all the fiber tips of the interferometer helps maximize the light transmission and thus signal to noise ratio.

Optical power incident upon the photodetector reflected from the sample arm of the interferometer which is incoherent with the reference light contributes to the total excess noise. This portion of incoherence optical power mainly comes from the light back-reflected from the fiber tip if a FC/PC pigtail is used. Angled polish (APC) fiber can be used to remove the incoherent optical power from the detector, so that the excess noise can be minimized.

### 7.2.4 Animal tissue modal for dual-mode microscopy

The superiority of dual-mode microscopy cannot be fully demonstrated unless it is verified using an appropriate animal modal. The purpose of this section is to recommend an established animal model for dual-mode micrscopy combining FMM and OCM. This animal modal is recommended also because the tissue is available at Prof. Hanry Yu's lab in IBN.

Normal and fibrosis Wistar rat liver tissues (fixed) can be obtained from Prof. Hanry Yu's lab at Institute of Bioengineering and Nanotechnology. Tissues are stain with Sirius red F3BA (Direct Red 80, #36-554-8, Sigma-Aldrich) which binds to the collegan fibers. The fluorephore typically can be excited at 565 nm and has an emission peak > 590 nm [236, 237]. The result of dual-mode imaging can be verified with the second harmonic generation microscopy. The following sample preparation protocol was obtained from Prof. Hanry Yu's lab at Institute of Bioengineering and Nanotechnology.

Solution A. Picro-sirius red

Sirius red F3B (C.I. 35782) ------------------------- 0.5 g

Saturated aqueous solution of picric acid ---------500 ml

Add a little solid picric acid to ensure saturation (This is important, so that it can be kept for at least 3 years and can be used many times)

Solution B. Acidified water

Add 5 ml acetic acid (glacial) to 1 litre of water (tap or distilled).

Procedure:

1) De-wax and hydrate paraffin sections.
2) (Optional, and not usually done) Stain nuclei with Weigert's haematoxylin
3) Stain in picro-sirius red (Solution A) for one hour (This gives near-equilibrium staining, which does not increase with longer times. Shorter times should not be used, even if the colours look OK.)
4) Wash in two changes of acidified water (Solution B).
5) Physically remove most of the water from the slides by vigorous shaking or (for a few slides only) blotting with damp filter paper.
6) Dehydrate in three changes of 100% ethanol.
7) Clear in xylene and mount in a resinous medium.
8) Tissue samples were sectioned by use of a scalpel, so that the size of the specimens is 8 mm×8 mm×0.5 mm. The tissue specimens were mounted with Gel Mount$^{TM}$ Aqueous Mounting Medium (G0918, Sigma) in specially made glass-slide chambers underneath glass-coverslips.

# Bibliography

[1]. B. Alberts, A. Johnson, J. Lewis, M. Raff, K. Roberts and P. Walter, “Cell Communication” p833 In *Molecular Biology of the Cell, fourth edition*. Garland Science (2002).

[2]. W. Tan, A. Sendemir-Urkmez, et al., “Structural and functional optical imaging of three-dimensional engineered tissue development,” *Tissue Engineering* **10**, 1747-1756 (2004).

[3]. S. A. Al-Chalabi, B. Culshaw, DEN Davies, “Partially coherent sources in interferometric sensors,” *First Internat. Conf. Optical Fibre Sensors I.E.E. London*, 132–135 (1983).

[4]. R. C. Youngquist, S. Carr, DEN Davies, “Optical coherencedomain reflectometry: a new optical evaluation technique,” *Opt. Lett.* **12**, 158–160 (1987).

[5]. A. F. Fercher, K. Mengedoht, W. Werner, “Eye length measurement by interferometry with partially coherent light. *Opt. Lett.* **13**, 186–189 (1988).

[6]. D. Huang, E. A. Swanson, C. P. Lin, J. S. Schuman, et al., “Optical coherence tomography,” *Science* **254**, 1178-1181 (1991).

[7]. T. Sawatari, “Optical heterodyne scanning microscope,” *Appl. Optics* **12,** 2766–2772 (1973).

[8]. L. Mandel, E. Wolf, “Optical coherence and quantum optics,” *Cambridge University Press*: Cambridge, 148–150 (1995).

[9]. A. Gh PODOLEANU, “Optical coherence tomography”, *British Journal of Radiology* **78**, 976–988 (2005).

[10]. B. Povazay, K. Bizheva, A. Unterhuber, B. Hermann, H. Sattmann, A. F. Fercher, W. Drexler, A. Apolonski, W. J. Wadsworth, J. C. Knight, and P. St. J. Russell, M. Vetterlein and E. Scherzer, “Submicrometer axial resolution optical coherence tomography”, *Opt. Lett.* **27**, 1800-1802 (2002).

[11]. G. J. Tearney, B. E. Bouma, and G. J. Fujimoto, “High-speed phase- and group-delay scanning with a grating-based phase control delay line,” *Opt. Lett.* **22**, 1811–1813 (1997).

[12]. M. A. Rollins, M. D. Kulkarni, S. Yazdanfar, R. Ung-arunyawee, and J. A. Izatt, “In vivo video rate optical coherence tomography,” *Opt. Express* **3**, 219–229 (1998).

[13]. L. Liu, N. Chen, “Double-Pass Rotary Mirror Array for Fast Scanning Optical Delay Line”, *Appl. Opt.*, **45**, 5426-31 (2006).

[14]. Yang, V. X. D. et al. High speed, wide velocity dynamic range Doppler optical coherence tomography (Part I): System design, signal processing, and performance. *Opt. Express* 11, 794–809 (2003).

[15]. A. L. Oldenburg, J. J. Reynolds, D. L. Marks, and S. A. Boppart, “Fast-Fourier-domain delay line for in vivo optical coherence tomography with a polygonal scanner,” *Appl. Opt.* **42**, 4606–4611 (2003).

[16]. A. M. Rollins and J. A. Izatt, “Optimal interferometer designs for optical coherence tomography,” *Opt. Lett.* **24**, 1484-1486 (1999).

[17]. A. F. Fercher, C. K. Hitzenberger, G. Kamp, S. Y. El-Zaiat, “Measurements of intraocular distances by backscattering spectral interferometry,” *Optics Communications* **117**, 43-48 (1995).

[18]. G. Hausler, M. W. Lindner, “Coherence radar and spectral radar - new tools for dermatological diagnosis,” *J. Biomed. Optics* **3**, 21–31 (1998).

[19]. L. M. Smith, C. C. Dobson, “Absolute displacement measurements using modulation of the spectrum of white light in a Michelson interferometer,” *Appl. Opt.* **28**, 3339–3342 (1981).

[20]. N. A. Nassif, B. Cense, B. H. Park, M. C. Pierce, et al., “*In vivo* high-resolution video-rate spectral-domain optical coherence tomography of the human retina and optic nerve,” *Opt. Express* **12**, 367-376 (2003).

[21]. N. A. Nassif, B. Cense, B. H. Park, et al., “*In vivo* human retinal imaging by ultrahigh-speed spectral domain optical coherence tomography,” *Opt. Lett.* **29**, 480-482 (2004).

[22]. M. A. Choma, M. V. Sarunic, C. Yang, J. A. Izatt, “Sensitivity advantage of swept source and Fourier domain optical coherence tomography,” *Opt. Express* **11**, 2183–2189 (2003).

[23]. R. Leitgeb, C. K. Hitzenberger, and A. F. Fercher, “Performance of Fourier domain vs. time domain optical coherence tomography”, *Opt. Express* **11**, 889-894 (2003).

[24]. J. F. de Boer, B. Cense, B. H. Park, M. C. Pierce, G. J. Tearney, B. E. Bouma, “Improved signal-to-noise ratio in spectral-domain compared with time-domain optical coherence tomography,” *Opt. Lett.* **28**, 2067-2069 (2003).

[25]. P. Targowski, M. Wojtkowski, A. Kowalczyk A, et al., “Complex spectral OCT in human eye imaging *in vivo*,” *Opt. Commun.* **229**, 79–84 (2004).

[26]. H. Barfuss, and E. Brinkmeyer, “Modified optical frequency-domain reflectometry with high spatialresolution for components of integrated optic systems,” *J. Lightwave Technol.* **7**, 3–10 (1989).

[27]. U. Glombitza, and E. Brinkmeyer, “Coherent frequency-domain reflectometry for characterization of single-mode integrated-optical wave-guides,” *J. Lightwave Technol.* **11**, 1377–1384 (1993).

[28]. R. Passy, Gisin, N., Vonderweid, J. P. & Gilgen, H. H. Experimental and theoretical investigations of coherent OFDR with semiconductor-laser sources. J. Lightwave Technol. 12, 1622–1630 (1994).

[29]. J. P. Vonderweid, R. Passy, and N. Gisin, “Midrange coherent optical frequency-domain reflectometry with a DFB laser-diode coupled to an external cavity,” *J. Lightwave Technol.* **13**, 954–960 (1995).

[30]. S. H. Yun, G. J. Tearney, J. F. de Boer, N. Iftimia, and B. E. Bouma, “High-speed optical frequency domain imaging,” *Opt. Express* **11**, 2953–2963 (2003).

[31]. W. Y. Oh, S. H. Yun, B. J. Vakoc, G. J. Tearney, and B. E. Bouma, “Ultrahigh-speed optical frequency domain imaging and application to laser ablation monitoring,” *Appl. Phys. Lett.* **88**, 103902 (2006).

[32]. S. H. Yun, et al., “Comprehensive volumetric optical microscopy *in vivo*,” *Nature Med.* **12**, 1429–1433 (2006).

[33]. H. Lim, J. F. de Boer, B. H. Park, E. C. Lee, R. Yelin, and S. H. Yun, "Optical frequency domain imaging with a rapidly swept laser in the 815-870 nm range," *Opt. Express* **14**, 5937-5944 (2006).

[34]. R. Huber, M. Wojtkowski, K. Taira, J. G. Fujimoto, and K. Hsu, “Amplified, frequency swept lasers for frequency domain reflectometry and OCT imaging: design and scaling principles,” *Opt. Express* **13**, 3513–3528 (2005).

[35]. R. Huber, M. Wojtkowski, and J. G. Fujimoto, “Fourier domain mode locking (FDML): A new laser operating regime and applications for optical coherence tomography,” *Opt. Express* **14**, 3225–3237 (2006).

[36]. R. Huber, D. C. Adler, and J. G. Fujimoto, “Buffered Fourier domain mode locking (FDML): Unidirectional swept laser sources for OCT imaging at 370,000 lines per second,” *Opt. Lett.* **31**, 2975–2977 (2006).

[37]. D. C. Adler, R. Huber, and J. G. Fujimoto, “Phase-sensitive optical coherence tomography at up to 370,000 lines per second using buffered Fourier domain mode locked lasers,” *Opt. Lett.* **32**, 626–628 (2007).

[38]. D. C. ADLER, Y. CHEN, R. HUBER, J. SCHMITT, J. CONNOLLY AND J. G. FUJIMOTO, "Three-dimensional endomicroscopy using optical coherence tomography", *Nat. Photonics* **1**, 709-716 (2007).

[39]. Y. Chen, D. M. de Bruin, C. Kerbage, and J. F. de Boer, **"**Spectrally balanced detection for optical frequency domain imaging," *Opt. Express* **15**, 16390-16399 (2007).

[40]. E. Beaurepaire, A. C. Boccara, M. Lebec, L. Blanchot, and H. Saint-Jalmes, "Full-field optical coherence microscopy," *Opt. Lett.* **23**, 244–246 (1998).

[41]. A.F. Fercher, C.K. Hitzenberger, M. Sticker, E. Moreno-Barriuso,R. Leitgeb, W. Drexler, H. Sattmann, "A thermal light source technique for optical coherence tomography", *Opt. Comm.* **185** 57-64 (2000).

[42]. A. Dubois, L. Vabre, A. C. Boccara, and E. Beaurepaire, "High resolution full-field optical coherence tomography with a Linnik microscope," *Appl. Opt.* **41**, 805–812 (2002).

[43]. A. Dubois, G. Moneron, K. Grieve, and A. C. Boccara, "Three-dimensional cellular-level imaging using full-field optical coherence tomography," Phys. Med. Biol. 49, 1227–1234 (2004).

[44]. A. Dubois, K. Grieve, G. Moneron, R. Lecaque, L. Vabre, and C. Boccara, "Ultrahigh-resolution full-field optical coherence tomography," *Appl. Opt.* **43**, 2874–2883 (2004).

[45]. L. Vabre, A. Dubois, and A. C. Boccara, "Thermal-light full-field optical coherence tomography," *Opt. Lett*. **27**, 530-532 (2002).

[46]. B. Laude, A. De Martino, B. Drevillon, L. Benattar, and L. Schwartz, "Full-field optical coherence tomography with thermal light," *Appl. Opt.* **41**, 6637-6645 (2002)

[47]. E. Bordenave, E. Abraham, G. Jonusauskas, N. Tsurumachi, J. Oberle, C. Rulliere, P. E. Minot, M. Lassegues, and J. E. Surleve Bazeille, "Wide-field optical coherence tomography: imaging of biological tissues," *Appl. Opt.* **41**, 2059-2064 (2002).

[48]. M. Akiba, K. P. Chan, and N. Tanno, "Full-field optical coherence tomography by two-dimensional heterodyne detection with a pair of CCD cameras," *Opt. Lett.* **28**, 816-818 (2003).

[49]. L. Yu and M. K. Kim, "Full-color three-dimensional microscopy by wide-field optical coherence tomography," *Opt. Express* **12**, 6632-6641 (2004).

[50]. Y. Watanabe, Y. Hayasaka, M. Sato, and N. Tanno, “Full-field optical coherence tomography by achromatic phase shifting with a rotating polarizer,” *Appl. Opt.* **44**, 1387-1392 (2005).

[51]. G. Moneron, A. C. Boccara, and A. Dubois, “Stroboscopic ultrahigh-resolution full-filed optical coherence tomography,” *Opt. Lett.* **30**, 1351-1353 (2005).

[52]. K. Grieve, A. Dubois, M. Simonutti, M. Paques, J. Sahel, J. F. Le Gargasson, C. Boccara, “In-vivo anterior segment imaging in the rat eye with high speed white light full-field optical coherence tomography,” *Opt. Express* **13**, 6286-6295 (2005).

[53]. W. Y. Oh, B. E. Bouma, N. Iftimia, S. H. Yun, R. Yelin, and G. J. Tearney, “Ultrahigh-resolution full-field optical coherence microscopy using InGaAs camera,” *Opt. Express* **14**, 726–735 (2006).

[54]. S. Yazdanfar, M. D. Kulkarni, J. A. Izatt, “High resolution imaging of in vivo cardiac dynamics using color Doppleroptical coherence tomography,” *Opt Express* **1**, 424–431 (1997).

[55]. Y. Zhao, Z. Chen, C. Saxer, S. Xiang, J. F. de Boer, J. S. Nelson, “Phase-resolved optical coherence tomography and optical Doppler tomography for imaging blood flow in human skin with fast scanning speed and high velocity sensitivity,” *Opt. Lett.* **25**,114–116 (2000).

[56]. A. M. Rollins, S. Yazdanfar, J. K. Barton, J. A. Izatt, “Real-time *in vivo* color Doppler optical coherence tomography,” *J. Biomed. Opt.* **7**, 123–129 (2000).

[57]. B. Cense, T. C. Chen, B. H. Park, M. C. Pierce, J. F. de Boer, “In vivo birefringence and thickness measurements of the human retinal nerve fiber layer using polarization-sensitive optical coherence tomography,” *J. Biomed. Opt.* **9**, 121–125 (2004).

[58]. M. R. Hee, D. Huang, E. A. Swanson, J. G. Fujimoto, “Polarizationsensitive low-coherence reflectometer for birefringence characterization and ranging,” *J. Opt. Soc. B* **9**, 903–908 (1992).

[59]. J. F. de Boer, T. E. Milner, “Review of polarization sensitive optical coherence tomography and Stokes vector determination,” *J. Biomed. Opt.* **7**, 359–371 (1992).

[60]. T. S. Ralston, D. L. Marks, S. A. Boppart, and P. S. Carney, “Inverse scattering for high-resolution interferometric microscopy,” *Opt. Lett.* **31**, 3585-3587 (2006).

[61]. T. S. Ralston, D. L. Marks, P. S. Carney, and S. A. Boppart, “Interferometric synthetic aperture microscopy,” *Nat. Phys.* **3**, 129-134 (2007).

[62]. T. S. Ralston, D. L. Marks, P. S. Carney, and S. A. Boppart, "Inverse scattering problem for optical coherence tomography," J. Opt. Soc. Am. A 23, 1027-1037 (2006).

[63]. E. A. Swanson, J. A. Izatt, M. R. Hee, D. Huang, C. P. Lin, J. S. Schuman, C. A. Puliafito, and J. G. Fujimoto, "In-vivo retinal imaging by optical coherence tomography," *Opt. Lett.* **18**, 1864-1866 (1993)

[64]. A. F. Fercher, C. K. Hitzenberger, W. Drexler, G. Kamp, and H. Sattmann, "In-Vivo Optical Coherence Tomography," *Am. J. Ophthalmol.* 116, 113-115 (1993).

[65]. J. P. Dunkers, M. T. Cicerone, and N. R. Washbern, “Collinear optical coherence and confocal fluorescence microscopies for tissue engineering,” *Optics Express* **11**, 3074 (2003).

[66]. A. T. Yeh, B. S. Kao, W. G. Jung, Z. P. Chen, J. S. Nelson, and B. J. Tromberg, “Imaging wound healing using optical coherence tomography and multiphoton microscopy in an in vitro skin-equivalent tissue model,” *J. Biomed. Opt.* **9**, 248–253 (2004).

[67]. C. Mason, J. F. Markusen, M. A. Town, P. Dunnill and R. K. Wang, “The potential of optical coherence tomography in the engineering of living tissue,” *Phys. Med. Biol.* **49**, 1097–1115 (2004).

[68]. K. HAN-JO, et al., “Optical Coherence Elastography of Engineered and Developing Tissue,” *TISSUE ENGINEERING* **12,** 63-73 (2006).

[69]. W. Tan, A. L. Oldenburg, J. J. Norman, T. A. Desai, S. A. Boppart, “Optical coherence tomography of cell dynamics in three-dimensional tissue models,” *Opt. Express* **14**, 7159-7171 (2006).

[70]. J. G. Fujimoto, M. E. Brezinski, G. J. Tearney, S. A. Boppart, B. E. Bouma, M. R. Hee, J. F. Southern, and E. A. Swanson, “Optical biopsy and imaging using optical coherence tomography” *Nature Med.* **1** 970–972 (1995).

[71]. J. G. Fujimoto, S. A. Boppart, G. J. Tearney, B. E. Bouma, C. Pitris, and M. E. Brezinski, “High resolution in vivo intra-arterial imaging with optical coherence tomography” *Heart* **82**, 128–133 (1999).

[72]. B. E. Bouma, and G. J. Tearney, eds, *Handbook of Optical Coherence Tomography,* New York: Marcel Dekker (2002).

[73]. A. F. Fercher, W. Drexler, C. K. Hitzenberger and T Lasser, “Optical coherence tomography - principles and applications,” *Rep. Prog. Phys.* **66** (2003) 239–303.

[74]. C. A. Puliafito, M. E. Hee, J. Schuman, and J. G. Fujimoto, *Optical Coherence Tomography of Ocular Disease,* Thorofare: Slack Inc (1995)

[75]. H. Hoerauf, and R. Birngruber, *Handbook of Optical Coherence Tomography* G. J. Tearney and B. E. Bouma, edsf, New York: Marcel Dekker, 487–503 (2002).

[76]. S. N. Bagayev, V. M. Gelikonov, G. V. Gelikonov, E. S. Kargapoltsev, R. V. Kuranov, A. M. Razhev, I. V. Tuchin, and A. A. Zhupikov, "Optical coherence tomography for *in situ* monitoring of laser corneal ablation,“ *J. Biomed. Opt.* **7** 633–642 (2002).

[77]. N.D. Gladkova, G.A. Petrova and N.K. Nikulin et al., "In vivo optical coherence tomography imaging of human skin: norm and pathology," *Skin Res. Technol.* **6**, 6–16 (2000).

[78]. J. Welzel, "Optical coherence tomography in dermatology: a review," *Skin. Res. Technol.* **7,** 1–9 (2001).

[79]. J. A. Izatt, M. D. Kulkarni, K. H. Wang, K. Kobayashi, and M. V. Sivak, "Optical Coherence Tomography and Microscopy in Gastrointestinal Tissues," *IEEE J. Select. Top. Quant. Electron.* **2,** 1017–28 (1996).

[80]. B. E. Bouma, G. J. Tearney, C. Compton, N. Nishioka, "Endoscopic Optical Coherence Tomography of the Gastrointestinal Tract," *Gastrointestinal Endoscopy* **49**, AB152 (1999).

[81]. A. M. Rollins and R.Ung-arunyawee, A. Chak, R. C. K. Wong, K. Kobayashi, M. V. Sivak, Jr. and J. A. Izatt, "Real-time *in vivo* imaging of human gastrointestinal ultrastructure by use of endoscopic optical coherence tomography with a novel efficient interferometer design," *Opt. Lett.* **24**, 1358-1360 (1999).

[82]. J. A. Evans, J. M. Poneros, B. E. Bouma, et al., "Optical coherence tomography to identify intramucosal carcinoma and high grade dysplasia in Barrett's esophagus," *Clinical Gastroenterology and Hepatology* **4**, 38-43 (2006).

[83]. J. M. Poneros, S. Brand, B. E. Bouma, G. J. Tearney, C. C. Compton, N. S. Nishioka, "Diagnosis of specialized intestinal metaplasia by optical coherence tomography," *Gastroenterology* **120**, 7-12 (2001).

[84]. B. J. Vakoc, M. Shishko, S. H. Yun, et al., "Comprehensive esophageal microscopy by using optical frequency-domain imaging," *Gastrointest. Endosc.* **65**, 898-905 (2007).

[85]. J. M. Poneros, G. J. Tearney, M. Shiskov, et al., "Optical coherence tomography of the biliary tree during ERCP," *Gastrointestinal Endoscopy* **55**, 84-88 (2002).

[86]. I. K. Jang, B. E. Bouma, D. H. Kang, et al., "Visualization of coronary atherosclerotic plaques in patients using optical coherence tomography," *Journal of the American College of Cardiology* **39**, 604-609 (2002).

[87]. I. K. Jang, G. J. Tearney, B. MacNeill, et al., “In vivo characterization of coronary atherosclerotic plaque by use of optical coherence tomography,” *Circulation* **111**, 1551-1555 (2005).

[88]. H. Yabushita, B. E. Bouma, S. L. Houser, et al., “Characterization of human atherosclerosis by optical coherence tomography,” *Circulation* **106**, 1640-1645 (2002).

[89]. B. D. MacNeill, I. K. Jang, B. E. Bouma, et al., “Focal and multi-focal plaque macrophage distributions in patients with acute and stable presentations of coronary artery disease,” *J. Am. Coll. Cardiol.* **44**, 972-979 (2004).

[90]. G. J. Tearney, H. Yabushita, S. L. Houser, H. T. Aretz, I.-K. Jang, K. H. Schlendorf, C. R. Kauffman, M. Shishkov, E. F. Halpern, B. E. Bouma, “Quantification of macrophage content in atherosclerotic plaques by optical coherence tomography,” *Circulation* **107**, 113-119 (2003).

[91]. J. M. Schmitt, "Optical Coherence Tomography (OCT): A review," *IEEE J. Sel. Top. Quantum Electron.* **5**, 1205-1215 (1999).

[92]. P. H. Tomlins, and R. K. Wang, **“**Theory, developments and applications of optical coherence tomography,” *J. Phys. D: Appl. Phys.* **38,** 2519–2535 (2005).

[93]. J. W. Goodman, *Statistical Optics*. New York, NY: John Wiley and Sons, 164–169 (1985).

[94]. J. G. Fujimoto, “Optical coherence tomography for ultrahigh resolution *in vivo* imaging,” *Nature Biotechnology* **21**, 1361-1367 (2003).

[95]. C. J. R. Sheppard, "Scanning optical microscopy," in *Advances in Optical and Electron Microscopy,* R. Barer and V. E. Cosslett, eds., Academic, London, **10**, 1-98 (1987).

[96]. C. J. R. Sheppard and A. Choudhury, "Image formation in the scanning microscope," *Opt. Acta* **24**, 1051-1073 (1977).

[97]. T. Wilson and C. J. R. Sheppard, *Theory and Practice of Scanning Optical Microscopy,* Academic London, (1984).

[98]. T. Wilson, "Optical sectioning in confocal fluorescence microscopes," *J. Microsc.* **154,** 143-156 (1988).

[99]. C. J. R. Sheppard and T. Wilson, “Depth of field in the scanning microscope,” *Opt. Lett.* **3**, 115–117 (1978).

[100]. H. Wang, G. Yuan, W. Tan, L. Shi, and T. Chong, “Spot size and depth of focus in optical data storage system,” *Opt. Eng.* **46**, 065201 (2007).

[101]. J. A. Izatt, M. R. Hee, G. M. Owen, E. A. Swanson, and J. G. Fujimoto, "Optical coherence microscopy in scattering media," *Opt. Lett.* **19**, 590-592 (1994)

[102]. A. M. Rollins and J. A. Izatt, "Optimal interferometer designs for optical coherence tomography," *Opt. Lett.* **24**, 1484-1486 (1999).

[103]. K. Takada, “Noise in Optical Low-Coherence Reflectometry,” *IEEE J. Quantum Electron.* **34,** 1098 (1998).

[104]. G. Häusler, and M. W. Lindner, ‘‘COHERENCE RADAR’’ AND ‘‘SPECTRAL RADAR’’—NEW TOOLS FOR DERMATOLOGICAL DIAGNOSIS,” *J. Biomed. opt.* **3** 21-32 (1998).

[105]. Maciej Wojtkowski, Vivek Srinivasan, Tony Ko, James Fujimoto, Andrzej Kowalczyk, and Jay Duker, "Ultrahigh-resolution, high-speed, Fourier domain optical coherence tomography and methods for dispersion compensation," Opt. Express **12**, 2404-2422 (2004)

[106]. Barry Cense, Nader Nassif, Teresa Chen, Mark Pierce, Seok-Hyun Yun, B. Park, Brett Bouma, Guillermo Tearney, and Johannes de Boer, "Ultrahigh-resolution high-speed retinal imaging using spectral-domain optical coherence tomography," Opt. Express **12**, 2435-2447 (2004)

[107]. E. Choi, J. H. Na, Y. Ryu, G. Mudhana, B. H. Lee, “All-fiber variable optical delay line for applications in optical coherence tomography: feasibility study for a novel delay line,” *Opt. Express* **13**, 1334-1345 (2005).

[108]. D. Piao, Q. Zhu, “Power-efficient grating-based scanning optical delay line: time-domain configuration,” *Electronics Letters* **40**, 97-98 (2004).

[109]. X. M. Liu, M. J. Cobb, X. D. Li, “Rapid scanning all-reflective optical delay line for real-time optical coherence tomography,” *Opt. Lett.* **29**, 80-82 (2004).

[110]. P. L. Hsiung, X. D. Li, C. Chudoba, I. Hartl, T. H. Ko, and J. G. Fujimoto, “High-speed path-length scanning with a multiple-pass cavity delay line,”*Applied Optics*. **42**, 640-648 (2003).

[111]. A. L. Oldenburg, J. J. Reynolds, D. L. Marks, S. A. Boppart, “Fast-Fourier-domain delay line for in vivo optical coherence tomography with a polygonal scanner,” *Applied Optics* **42**, 4606-4611 (2003).

[112]. N. A. Riza, Z. Yaqoob, “Submicrosecond speed optical coherence tomography system design and analysis by use of acousto-optics,” *Applied Optics* **42**, 3018-3026 (2003).

[113]. B. H. Lee, T. J. Eom, E. Choi, G. Mudhana, C. Lee, “Novel optical delay line for optical coherence tomography system,” *Optical Review* **10**, 572-575 (2003).

[114]. N. G. Chen and Q. Zhu, “Rotary mirror array for high-speed optical coherence tomography,” *Optics Letters* **27**, 607-609 (2002).

[115]. K. K. M. B. D. Silva, A. V. Zvyagin, and D. D. Sampson, “Extended range, rapid scanning optical delay line for biomedical interferometric imaging,” *Electronics Letters* **35**, 1404-1406 (1999).

[116]. G. J. Tearney, B. E. Bouma, and J. G. Fujimoto, “High-speed phase- and group-delay scanning with a grating-based phase control delay line,” *Opt. Lett.* **22**, 1811-1813 (1997).

[117]. R. Windecker, M. Fleischer, B. Franze, and H. J. Tiziani, “Two Methods for Fast Coherence Tomography and Topometry,” *Journal of Modern Optics* **44**, 967-977 (1997).

[118]. D. J. Faber, E. G. Mik, M. C. G. Aalders, T. G. van Leeuwen, “Toward assessment of blood oxygen saturation by spectroscopic optical coherence tomography,” *Opt. Lett.* **30**, 1015-1017 (2005).

[119]. C. Y. Xu, D. L. Marks, M. N. Do, S. A. Boppart, “Separation of absorption and scattering profiles in spectroscopic optical coherence tomography using a least-squares algorithm,” *Opt. Express* **12**, 4790-4803 (2004).

[120]. C. H. Yang, M. A. Choma, L. E. Lamb, J. D. Simon, J. A. Izatt, “Protein-based molecular contrast optical coherence tomography with phytochrome as the contrast agent,” *Opt. Lett.* **29**, 1396-1398 (2004).

[121]. U. Morgner, W. Drexler, F. X. Kartner, X. D. Li, C. Pitris, E. P. Ippen, J. G. Fujimoto, “Spectroscopic optical coherence tomography,” *Opt. Lett.* **25**, 111-113 (2000).

[122]. J. M. Schmitt, S. H. Xiang, K. M. Yung, “Differential absorption imaging with optical coherence tomography,” *J. Opt. Soc. A* **15**, 2288-2296 (1998).

[123]. N. Chen, Q. Zhu, “Rotary mirror array for fast optical tomography,” U.S**.** Pat. No**.** 6813050 (2004).

[124]. N. G. Chen and L. Liu, "Improved Optical Design for Fast Scanning RMA," in *Biomedical Optics*, Technical Digest (CD) (Optical Society of America, 2006), paper TuI42.

[125]. L. Liu, N. Chen, “Double-Pass Rotary Mirror Array for Fast Scanning Optical Delay Line”, *Appl. Opt.*, **45**, 5426-31 (2006).

[126]. T. Wilson, C. J. R. Sheppard, Theory and Practice of Scanning Optical Microscopy, Academic Press, London (1984).

[127]. J. A. Izatt, M. D. Kulkarni, H. W. Wang, K. Kobayashi, M. V. Sivak, Jr., “Optical coherence tomography and microscopy in gastrointestinal tissues,” *IEEE J. of Sel. Top. Quantum Electron.* **2**, 1017-1028 (1996).

[128]. L. Liu and N. G. Chen, "Double-pass rotary mirror array for fast scanning optical delay line," *Appl. Opt.* **45**, 5426-5431 (2006).

[129]. W. Drexler, U. Morgner, F.X. Kartner, C. Pitris, S.A. Boppart, X.D. Li, E.P. Ippen, and J.G. Fujimoto, "*In vivo* ultrahigh-resolution optical coherence tomography," *Opt. Lett.* **24**, 1221-1223 (1999).

[130]. L. Liu, C. Liu, W. C. Howe, C. J. R. Sheppard, and N. Chen, "Binary-phase spatial filter for real-time swept-source optical coherence microscopy," *Opt. Lett.* **32**, 2375-2377 (2007).

[131]. M. Petran and M. Hadravsky, "Tandem-Scanning Reflected-Light Microscope," *J. Opt. Soc. A* **58**, 661-664 (1968).

[132]. H. Buist, M. Muller, J. Squier, and G. J. Brackenhoff, "Real time two-photon absorption microscopy using multi point excitation," *J. Microsc.* **192**, 217-226 (1998).

[133]. D. Aguirre, P. Hsiung, T. H. Ko, I. Hartl, and J. G. Fujimoto, "High-resolution optical coherence microscopy for high-speed, *in vivo* cellular imaging," *Opt. Lett.* **28**, 2064-2066 (2003).

[134]. M. Rajadhyaksha, R. R. Anderson, and R. H. Webb, "Video-Rate Confocal Scanning Laser Microscope for Imaging Human Tissues *In Vivo*," *Appl. Opt.* **38**, 2105-2115 (1999).

[135]. K. H. Kim, C. Buehler, and P. T. C. So, "High-Speed, Two-Photon Scanning Microscope," *Appl. Opt.* **38**, 6004-6009 (1999).

[136]. Wayne R. Johnson, “High speed, high intensity optical recording system,” U.S. Pat. No. 3154371 (1964)

[137]. Herbert M. Runciman, “Optical scanning system with two sequential reflection stations,” U.S. Pat. No. 4461534 (1984);

[138]. Masaru Noguchi, “Light beam scanner with parallelism error correction,” U.S. Pat. No. 4129355 (1978);

[139]. Leo Beiser, “Double-reflection light scanner,” U.S. Pat. No. 5114217 (1992);

[140]. N. Chen, Q. Zhu, “Rotary mirror array for fast optical tomography,” U.S. Pat. No. 6813050 (2004).

[141]. Nanguang Chen and Quing Zhu, “Fast scanning confocal microscopy with a rotary mirror array”, *SPIE Proceedings*, **4964**, 33-40 (2003).

[142]. L. Liu, N. Chen, and C. J. R. Sheppard, "Double-reflection polygon mirror for high-speed optical coherence microscopy," *Opt. Lett.* **32**, 3528-3530 (2007)

[143]. L. Liu and N. Chen, “Double-reflection rotary parallel mirror array for fast beam scanning”. U.S. Pat. Appl. No. 60/955,469. Pending.

[144]. G. J. Tearney, M. E. Brezinski, B. E. Bouma, S. A. Boppart, C. Pitris, J. F. Southern, J.G. Fujimoto. “In vivo endoscopic optical biopsy with optical coherence tomography,” *Science* **276**, 2037-2039 (1997).

[145]. P. R. Herz, Y. Chen, A. D. Aguirre, K. Schneider, P. Hsiung, J. G. Fujimoto, K. Madden, J. Schmitt, J. Goodnow, and C. Petersen, "Micromotor endoscope catheter for in vivo, ultrahigh-resolution optical coherence tomography," *Opt. Lett.* **29**, 2261-2263 (2004).

[146]. D. Yelin, I. Rizvi, W. White, J. Motz J, T. Hasan, B. E. Bouma, and G. J. Tearney, “Three-dimensional miniature endoscopy”, *Nature* **443**, 765-765 (2006).

[147]. W. Jung, D. T. McCormick, Y. -C. Ahn, A. Sepehr, M. Brenner, B. Wong, N. C. Tien, and Z. Chen, "*In vivo* three-dimensional spectral domain endoscopic optical coherence tomography using a microelectromechanical system mirror," *Opt. Lett.* **32**, 3239-3241 (2007).

[148]. D. Y. Yu, T. Y. Zhou, X. D. Chen, K. L. Jiang, L. Liu, H. B. Xie, “Trans-endoscopic Micro-OCT-ultrasound Imaging probe,” CN1593351 (2005).

[149]. J. M. Schmitt, S. L. Lee, and K. M. Yung, “An optical coherence microscope with enhanced resolving power in thick tissue,” *Opt. Commun.* **142**, 203-207 (1997).

[150]. L. Liu and N. Chen, “Dynamic focusing with radial gratings for *in vivo* high resolution imaging," Proceedings of SPIE Vol. 6847, Coherence Domain Optical Methods and Optical Coherence Tomography in Biomedicine XII, Joseph A. Izatt, James G. Fujimoto, Valery V. Tuchin, Editors, 684718 (Feb. 18, 2008).

[151]. C. Liu and S. -H. Park, “Numerical analysis of an annular-aperture solid immersion lens,” *Opt. Lett.* **29**, 1742 (2004).

[152]. C. J. R. Sheppard, D. K. Hamilton, and I. J. Cox, "Optical microscope with extended depth field," *Proc. R. Soc. London Ser. A* **387**, 171-186 (1983).

[153]. C. J. R. Sheppard, “Synthesis of filters for specified axial properties,” *J. Mod. Opt.* **43**, 525-536 (1996).

[154]. T. S. Ralston, D. L. Marks, S. A. Boppart, and P. S. Carney, “Inverse scattering for high-resolution interferometric microscopy,” *Opt. Lett.* **31**, 3585-3587 (2006).

[155]. T. S. Ralston, D. L. Marks, P. S. Carney, and S. A. Boppart, “Interferometric synthetic aperture microscopy,” *Nat. Phys.* **3**, 129-134 (2007).

[156]. Z. Ding, H. Ren, Y. Zhao, J. S. Nelson, and Z. Chen, “High-resolution optical coherence tomography over a large depth range with an axicon lens,” *Opt. Lett.* **27**, 243 (2002).

[157]. R. A. Leitgeb, M. Villiger, A. H. Bachmann, L. Steinmann, and T. Lasser, “Extended focus depth for Fourier domain optical coherence microscopy,” *Opt. Lett.* **31**, 2450 (2006).

[158]. H. Wang and F. Gan, “High focal depth with a pure-phase apodizer,” *Appl. Optics* **40**, 5658 (2001).

[159]. H. Wang and F. Gan, “Phase-shifting apodizers for increasing focal depth,” *Appl. Optics* **41**, 5263 (2002).

[160]. H. Wang, Z. Chen, and F. Gan, “Phase-shifting apodizer for next-generation digital versatile disk,” *Opt. Eng.* **40**, 991 (2001).

[161]. H. Wang, L. Shi, G. Yuan, X. S. Miao, W. Tan, and T. Chong, “Subwavelength and super-resolution nondiffraction beam,” *Appl. Phys. Lett.* **89**, 171102 (2006).

[162]. Haifeng Wang, Luping Shi, Boris Luk’yanchuk, Colin Sheppard and Chong Tow Chong, “Creation of a needle of longitudinal polarized light in vacuum using binary optics”, *Nature Photonics*, doi:10.1038/nphoton.2008.127.

[163]. L. Liu, F. Diaz, L. Wang, B. Loiseaux, J-P. Huignard, C. J. R. Sheppard, and N. Chen, "Superresolution along extended depth of focus with binary-phase filters for Gaussian beam," *J. Opt. Soc. Am.* A **25**, 2095-2101 (2008).

[164]. L. Liu, F. Diaz, B. Loiseaux, J.-P. Huignard, N. Chen and C. J. R. Sheppard, "Focus optimization with binary wave-front coding," Conference on Lasers and Electro-Optics (Optical Society of America), paper JTua67, San Jose, California USA (2008).

[165]. L. Liu, C. Liu, W. C. Howe, C. J. R. Sheppard, and N. Chen, "Real-time High Resolution Optical Coherence Microscopy with a Phase Shifting Apodizer," *IEEE/ICME International Conference on Complex Medical Engineering*, 1105-1108 (2007).

[166]. M. Born, E. Wolf, *Principle of Optics* (Pergamon Press, Oxford 1975) 5th edition, Chapter 8.

[167]. Min Gu, C. J. R. Sheppard, and X. Gan, "Image formation in a fiber-optical confocal scanning microscope," *J. Opt. Soc. Am. A* **8**, 1755-1761 (1991).

[168]. A. W Snyder and J. D. Love, *Optical Waveguide Theory* (Chapman and Hall, London, 1983).

[169]. C. J. R. Sheppard and Z. S. Hegedus, "Axial behavior of pupil-plane filters," *J. Opt. Soc. Am. A* **5**, 643- (1988).

[170]. C. J. R. Sheppard, S. Ledesma, J. Campos, and J. C. Escalera, "Improved expressions for performance parameters for complex filters," *Opt. Lett.* **32**, 1713-1715 (2007).

[171]. N. Sanner, N. Huot, E. Audouard, C. Larat, J. -P. Huignard, and B. Loiseaux, "Programmable focal spot shaping of amplified femtosecond laser pulses," *Opt. Lett.* **30**, 1479-1481 (2005).

[172]. American National Standards Institute (2000) Safe use of lasers. In *ANSI Z 136,* pp. 1-2000. Laser Institute of America, Orlando, FL.

[173]. R. Huber, M. Wojtkowski and J. G. Fujimoto, J. Y. Jiang and A. E. Cable, "Three-dimensional and C-mode OCT imaging with a compact, frequency swept laser source at 1300 nm", *Opt. Express* **13**, 10523-10538 (2005).

[174]. Valk, P. E., D. L. Bailey, D. W. Townsend and M. N. Maisey (2003) *Positron Emission Tomography: Principles and Practice.* Springer Verlag, New York.

[175]. Femandes, P. A., A. T. P. Carvalho, A. T. Marques, A. L. F. Pereira, **A.** P. *S.* Madeira, A. S. P. Ribeiro, A. F. R. Carvalho, E. T. A. Ricardo, F. J. V. Pinto, H. A. Santos, H. D. G. Mangericao, H. M. Martins, H. D. B. Pinto, H. R. R. Santos, I. S. Moreira, M. J. V. Azeredo, R. P. S. Abreu, R. M. S. Oliveira, *S.* F. M. Sousa, R. Silva, Z. S. Mourao and M. J. Ramos, "New designs for MRI contrast agents," *J. Conaput. Aided Mol. Des.* **17,** 463473 (2003).

[176]. Changhuei Yang, "Molecular Contrast Optical Coherence Tomography: A Review," Photochemistry and Photobiology **81**, 215-237 (2005).

[177]. Duggar, K. H., D. A. Lauffenburger and P. T. C. So, "Two-photon fluorescence resonance energy transfer and its application to measurement of cell adhesion receptor binding to substratum ligands," *Biophys*. J. **76,** A98-A98 (1999).

[178]. A. Hoppe, K. Christensen and J. A. Swanson, "Fluorescence resonance energy transfer-based stoichiometry in living cells," *Biophyys. J.* **83,** 3652-3664 (2002).

[179]. Malvezzi-Campeggi, F., M. Jahnz, K. G. Heinze, P. Dittrich and P. Schwille, "Light-induced flickering of DsRed provides evidence for distinct and interconvertible fluorescent states," *Biophys. J.* **81,** 1776-1785 (2001).

[180]. Srivastava, M., H. Ow, D. Larson, D. Holowka, U. Wiesner, W**.** Webb and B. Baird, "Single particle tracking of fluorescent silica nanoparticles bound to IgE receptors on RBL mast cells," *Biophys. J.* **82,** 2436 (2002).

[181]. E. Chung, D. Kim, and P. T. So, "Extended resolution wide-field optical imaging: objective-launched standing-wave total internal reflection fluorescence microscopy," *Opt. Lett.* **31**, 945-947 (2006).

[182]. S. W. Hell and J. Wichmann, "Breaking the diffraction resolution limit by stimulated emission: stimulated-emission-depletion fluorescence microscopy," *Opt. Lett.* **19**, 780- (1994).

[183]. Denk, W., J. H. Strickler, and W. W. Webb, "Two-photon laser scanning fluorescence microscopy," *Science* **248**, 73-76 (1990).

[184]. J. R. Lakowicz, H. Szmacinski, K. Nowaczyk, K. Berndt, and. M. L. Johnson, " Fluorescence lifetime imaging", *Anal. Biochem.* **202**, 316-330 (1992).

[185]. Axelrod, D., Koppel, D.E., Schlessinger, J., Elson, E., and Webb, W.W. "Mobility measurement by analysis of fluorescence photobleaching recovery kinetics**"** *Biophys. J.* **16**, 1055-1069 (1976).

[186]. N. Panchuk-Voloshina, R. P. Haugland, J. Bishop-Stewart, M. K**.** Bhalgat, P. J. Millard, F. Mao and W. Y**.** Leung, "Alexa dyes, a series of new fluorescent dyes that yield exceptionally bright, photostable conjugates," *J. Histochem. Cytochem.* **47,** 1179-1188 (1999)**.**

[187]. H. H. Gerdes, and C. Kaether, "Green fluorescent protein: applications in cell biology," *FEBS Lett.* **389,** 44-47 (1996).

[188]. A. A. Heikal, S.T.Hessand W. W. Webb, "Multiphotonmolecular spectroscopy and excited-state dynamics of enhanced green fluorescent protein (EGFP): acid-base specificity," *Chem. Phys.* **274,** 37-55 (2001).

[189]. Jung, G., S. Mais, A. Zumbusch and C. Brauchle, "The role of dark states in the photodynamics of the green fluorescent protein examined with two-color fluorescence excitation spectroscopy," *J. Phys. Chem. A **104,*** 873-877 (2000).

[190]. R. H. Kohler, W. R. Zipfel, W. W. Webb, and M. R. Hanson, "The green fluorescent protein as a marker to visualize plant mitochondria *in vivo*," *Plant J.* **11.** 613-621 (1997).

[191]. H. Gratz, A. Penzkofer, C. Abels, R. M. Szeimies, M. Landthaler, and W. Baumler, "Photo-isomerisation, triplet formation, and photodegradation dynamics of indocyanine green solutions," *J. Photochem. Photohiol. A: Chem.* **128**, 101-109 (1999).

[192]. S. H. Yun, G. J. Tearney, B. Bouma, B. Park and J. F. de Boer, “High-speed spectral domain optical coherence tomography at 1.3 um wavelength,” *Opt. Express* **11**, 3598-3604 (2003).

[193]. H. P. Buschman, G. Deinum, J. T. Motz, M. Fitzmaurice, J. R. Kramer, A. van der Laarse, A. V. Bruschke, and M. S. Feld, "Raman microspectroscopy of human coronary atherosclerosis: Biochemical assessment of cellular and extracellular morphologic structures in situ," *Cardiovasc. Pathol.* **10**, 69-82 (2001).

[194]. H. P. Buschman, J. T. Motz, G. Deinum, M. Fitzmaurice, J. R. Kramer, A. van der Laarse, A. V. Bruschke, and M. S. Feld, “Diagnosis of human coronary atherosclerosis by morphology-based Raman spectroscopy,” *Cardiovasc. Pathol.* **10**, 59-68 (2001).

[195]. I. Freund, M. Deutsch and A. Sprecher, “Connectivetissue polarity-ptical 2nd-harmonic microscopy, crossed-beam summation, and small-angle scattering in rat-tail tendon,” *Biophys. J.* **50**, 693-712 (1986).

[196]. E. Georgiou, T. Theodossiou, V. Hovhannisyan, K. Politopoulos, G. S. Rapti and D. Yova, “Second and third optical harmonic generation in type I collagen, by nanosecond laser irradiation, over a broad spectral region,” *Opt. Commun.* **176**, 253-260 (2000).

[197]. Y. C. Guo, P. P. Ho, H. Savage, D. Harris, P. Sacks, S. Schantz, F. Liu, N. Zhadin and R. R. Alfano, “Second-harmonic tomography of tissues,” *Opt. Lett.* **22**, 1323-1325 (1997).

[198]. J. X. Cheng, A**.** Volkmer, L. D. Book and X. S. Xie, “An epidetected coherent anti-stokes raman scattering (E-CARS) microscope with high spectral resolution and high sensitivity,” *J. Phys. Chem. B* **105**, 1277-1280 (2001).

[199]. Volkmer, A., J. X. Cheng, L. D. Book and X. S. Xie, “New advances in coherent anti-Stokes Raman scattering (CARS) microscopy and spectroscopy of biological systems,” *Biophys. J.* **80,** 164A-164A (2001).

[200]. A. Zumbusch, G. R. Holtom and X. S. Xie, “Three-dimensional vibrational imaging by coherent anti-Stokes Raman scattering,” *Phys. Rev. Lett.* **82**, 4142-4145 (1999).

[201]. X. S. Gan, S. P. Schilders, and M. Gu, “Image formation in turbid media under a Microscope,” *J. Opt. Soc. Am. A* **15**, 2052-2058 (1998)

[202]. J. M. Schmitt, A. Knfittel, M. Yadlowsky, “Confocal microscopy in turbid medium,” *J. Opt. Soc. Am. A* **11**, 2226-2235 (1994).

[203]. P. T. C. So, H. Kim, I. E. Kochevar, “Two photon deep tissue *ex vivo* imaging of mouse dermal and subcutaneous structures. *Opt. Express*. **3**: 339-350 (1998).

[204]. C. H. Yang, A. Wax and M. S. Feld, "Measurement of the anomalous phase velocity of ballistic light in a random medium by use of a novel interferometer," *Opt. Lett.* **26**, 235-237 (2001).

[205]. M. R. Hee, J. A. Izatt, E. A. Swanson, D. Huang, J. S. Schuman, C. P. Lin, C. A. Puliafito and J. G. Fujimoto, "Optical coherence tomography of the human Retina," *Arch. Ophthalmol.* **113**, 325-332 (1995).

[206]. S. Yazdanfar, A. M. Rollins and J. A. Izatt, "Imaging and velocimetry of the human retinal circulation with color Doppler optical coherence tomography," *Opt. Lett.* **25**, 1448-1450 (2000).

[207]. D. Huang, M. R. Chalita, Y. Li, C. Y. Lowder, D. M. Meisler, A. M. Rollins and J. A. Izatt, "High-speed optical coherence tomography of anterior segment surgical anatomy and pathology," *Invest. Ophthalmol. Vis. Sci.* **44**, U141-Ul41 (2003).

[208]. Y. Li, M. R. Chalita, J. Goldsmith, V. Westphal, B. A. Bower, R. Shekhar, A. M. Rollins, J. A. Izatt and D. Huang, "Automated anterior chamber biometry with high-speed optical coherence tomography," *Invest. Ophthalmol. Vis. Sci.* 44, U285-U285 (2003).

[209]. S. Radhakrishnan, A. M. Rollins, J. E. Roth, S. Yazdanfar, V. Westphal, D. S. Bardenstein and J. A. Izatt, "Real-time optical coherence tomography of the anterior segment at 1310 nm," *Arch. Ophthalmol.* **119**, 1179-1185 (2001).

[210]. Brezinski, M. E., G. J. Tearney, B. E. Bouma, J. A. Izatt, M. R. Hee, E. A. Swanson, J. F. Southern and J. G. Fujimoto, "Optical coherence tomography for optical biopsy-properties and demonstration of vascular pathology," *Circulation* **93**, 1206-1213 (1996).

[211]. G. J. Tearney, and B. E. Bouma, "Atherosclerotic plaque characterization by spatial and temporal speckle pattern analysis," *Opt. Lett.* **27**, 533-535 (2002).

[212]. A. Das, M. V. Sivak, A. Chak, R. C. Wong, V. Westphal, A**.** M. Rollins, J. Izatt, G. A. Isenberg and J. Willis, "Role of high resolution endoscopic imaging using optical coherence tomography (OCT) in patients with Barrett's esophagus (BE). *Gastrointest. Endosc.* **51**, AB93-AB93 (2000).

[213]. M. V. Sivak, K. Kobayashi, J. A. Izatt, A. M. Rollins, R. Ungmnyawee, A. Chak, R. C. K. Wong, G. A. Isenberg and J. Willis, "High-resolution endoscopic imaging of the GI tract using optical coherence tomography," *Gustruintest. Endosc.* **51**, 474-479 (2000).

[214]. A. M. Rollins, R. Ung-arunyawee, A. Chak, R. C. K. Wong, K. Kobayashi, M. V. Sivak and J. A. Izatt, "Real-time in vivo imaging of human gastrointestinal ultrastructure by use of endoscopic optical coherence tomography with a novel efficient interferometer design," *Opt. Lett.* **24**, 1358-1360 (1999).

[215]. K. D. Rao, M. A. Choma, S. Yazdanfar, A. M. Rollins and J. A. Izatt, “Molecular contrast in optical coherence tomography by use of a pump-probe technique,” *Opt. Lett.* **28**, 340-342 (2003).

[216]. C. Yang, M. A. Choma, L. E. Lamb, J. D. Simon and J. Izatt, “Protein based molecular contrast OCT with phytochrome as the contrast agent,” *Opt. Lett.* **29**, 1396-1398 (2004).

[217]. C. Xu, J. Ye, D. L. Marks, and S. A. Boppart, "Near-infrared dyes as contrast-enhancing agents for spectroscopic optical coherence tomography," Opt. Lett. **29**, 1647-1649 (2004)

[218]. C. Yang, L. E. Lamb, J. D. Simon, M. A. Choma, B. Applegate and J. Izatt, “Spectral triangulation molecular contrast optical coherence tomography with indocyanine green as the contrast agent,” *Opt. Lett.* 29, 2016-2018 (2004).

[219]. Morgner, U., W. Drexler, F. X. Kartner, X. D. Li, C. Pitris, E. P. Ippen and J. G. Fujimoto, “Spectroscopic optical coherence tomography,” *Opt. Lett.* **25**, 111-113 (2000).

[220]. Y. Jiang, I. Tomov, Y. Wang and Z. P. Chen, “Second-harmonic optical coherence tomography,” *Opt. Lett.* **29**, 1090-1092 (2004).

[221]. S. Yazdanfar, L. H. Laiho and P. T. C. So, “Interferometric second harmonic generation microscopy,” *Opt. Express* **12**, 2739-2745 (2004).

[222]. B. Applegate, C. Yang, A. M. Rollins and J. Izatt, “Polarization resolved second harmonic generation optical coherence tomography in collagen,” *Opt. Lett.* **29**, 2252-2254 (2004).

[223]. C. Vinegoni, J. S. Bredfeldt, D. L. Marks and S. A. Boppart, “Nonlinear optical contrast enhancement for optical coherence tomography,” *Opt. Express* **12**, 331-341 (2004).

[224]. T. M. Lee, A. L. Oldenburg, S. Sitafalwalla, D. L. Marks, W. Luo, F. J. Toublan, K. S. Suslick and S. A. Boppart, “Engineered microsphere contrast agents for optical coherence tomography,” *Opt. Lett.* **28**, 1546-1548 (2003).

[225]. A. L. Oldenburg, J. R. Gunther, and S. A. Boppart, "Imaging magnetically labeled cells with magnetomotive optical coherence tomography," *Opt. Lett.* **30**, 747-749 (2005).

[226]. E. Beaurepaire and L. Moreaux, F. Amblard, J. Mertz, “Combined scanning optical coherence and two-photon-excited fluorescence microscopy,” *Opt. Lett.* **24**, 969-971 (1999).

[227]. S. Tang, T. B. Krasieva, Z. Chen, B. J. Tromberg, "Combined multiphoton microscopy and optical coherence tomography using a 12-fs broadband source," *J. Biomed. Opt.* **11**, 20502 (2006).

[228]. C. Vinegoni, T. Ralston, W. Tan, W. Luo, D.L. Marks, S.A. Boppart, "Integrated structural and functional optical imaging combining spectral-domain optical coherence and multiphoton microscopy," *Appl. Phys. Lett.* **88**, 053901 (2006).

[229]. C. H. Wong, L. Liu, C. J. R. Sheppard and N. G. Chen, "Penetration depth extension via focal modulation", *The 3rd Tohoku-NUS Joint Symposium on Nano-Biomedical Engineering in the East Asian-Pacific Rim Region* 65-66 (2007).

[230]. N. G. Chen, C. J. R. Sheppard and C. H. Wong, "Focal modulation microscope," *US patent*, pending.

[231]. J.–R. Lukas, M. Aigner, M. Denk, H. Heinzl, M. Burian, and R. Mayr, "Carbocyanine Postmortem Neuronal Tracing: Influence of Different Parameters on Tracing Distance and Combination with Immunocytochemistry", *J. Histochem Cytochem.* **46**, 901 (1998).

[232]. Becton Dickinson Immunocytometry Systems Source Book 2.10 (1989).

[233]. L. L. Lanier, and N. L. Warner, "Paraformaldehyde Fixation of Hematopoietic Cells for Quantitative Flow Cytometry (FACS) Analysis," *Journal of Immunological Methods* **47**, 25-30 (1981).

[234]. Peter J. Dwyer, Charles A. DiMarzio, and Milind Rajadhyaksha, "Confocal theta line-scanning microscope for imaging human tissues," Appl. Opt. **46**, 1843-1851 (2007)

[235]. D. Choi, H. Hiro-Oka, H. Furukawa, R. Yoshimura, M. Nakanishi, K. Shimizu, and K. Ohbayashi, "Fourier-domain optical coherence tomography using optical de-multiplexers imaging at 60,000,000 lines/s," *Opt. Lett.*, to be published.

[236]. P. C. DOLBER and M. *S.* SPACH, "Conventional and Confocal Fluorescence Microscopy of Collagen Fibers in the Heart", *Journal of Histochemistry and Cytochemistry* **41**, 465-469 (1993).

[237]. P. J. Hanley, A. A. Young, I. J. LeGrice, S. G. Edgar and D. S. Loiselle, "3-Dimensional configuration of perimysial collagen fibres in rat cardiac muscle at resting and extended sarcomere lengths," *J. Physiol.* **517**, 831-837 (1999).

# List of publications

## Journal papers:

1. **L. Liu**, F. Diaz, L. Wang, B. Loiseaux, J.-P. Huignard, N. Chen and C. J. R. Sheppard, "Super-resolution along extended depth of focus with binary-phase filters for Gaussian beam," *J. Opt. Soc. Am. A* **25**, 2095-2101 (2008).
2. **L. Liu**, N. Chen, and C. J. R. Sheppard, "Double-reflection polygon mirror for high-speed optical coherence microscopy," *Opt. Lett.* **32**, 3528-3530 (2007).
3. **L. Liu**, C. Liu, W. C. Howe, C. J. R. Sheppard and N. Chen, "Binary-phase spatial filter for real-time swept-source optical coherence microscopy," *Opt. Lett.* **32**, 2375-2377 (2007).
4. **L. Liu**, N. Chen, “Double-Pass Rotary Mirror Array for Fast Scanning Optical Delay Line”, *Appl. Opt.*, **45**, 5426-5431 (2006).

## Pending patents:

1. US 60/955,469, N. Chen and **L. Liu**, Double-reflection rotary parallel mirror array for fast beam scanning, pending (2007).

## Conference proceedings:

1. **L. Liu** and N. Chen, “Dynamic focusing with radial gratings for *in vivo* high resolution imaging," Proc. SPIE, **6847**, 684718 (2008).
2. **L. Liu**, C. Liu, W. C. Howe, C. J. R. Sheppard, and N. Chen, "Real-time High Resolution Optical Coherence Microscopy with a Phase Shifting Apodizer," IEEE/ICME International Conference on Complex Medical Engineering, 1105-1108 (2007).

## Conference presentations:

1. **L. Liu**, F. Diaz, B. Loiseaux, J.-P. Huignard, C. J. R. Sheppard, and N. Chen "Beam shaping for optical coherence tomography," OWLS-10 (Optics Within Life Sciences-10 / Biophotonics Asia 2008), 2-4 July, Singapore (2008)

2. **L. Liu**, F. Diaz, B. Loiseaux, J.-P. Huignard, N. Chen and C. J. R. Sheppard, "Focus optimization with binary wave-front coding," Conference on Lasers and Electro-Optics (Optical Society of America), paper JTua67, San Jose, California USA (2008).

3. C. H. Wong, **L. Liu**, C. J. R. Sheppard and N. G. Chen, "Penetration depth extension via focal modulation", The 3rd Tohoku-NUS Joint Symposium on Nano-Biomedical Engineering in the East Asian-Pacific Rim Region, Singapore (2007).

4. N. G. Chen and **L. Liu**, "Improved Optical Design for Fast Scanning RMA," in *Biomedical Optics*, Technical Digest (CD) (Optical Society of America), paper TuI42, St. Petersburg, Florida, USA (2008).

# Appendices

## Appendix A: Drawings of motor mount for RMA

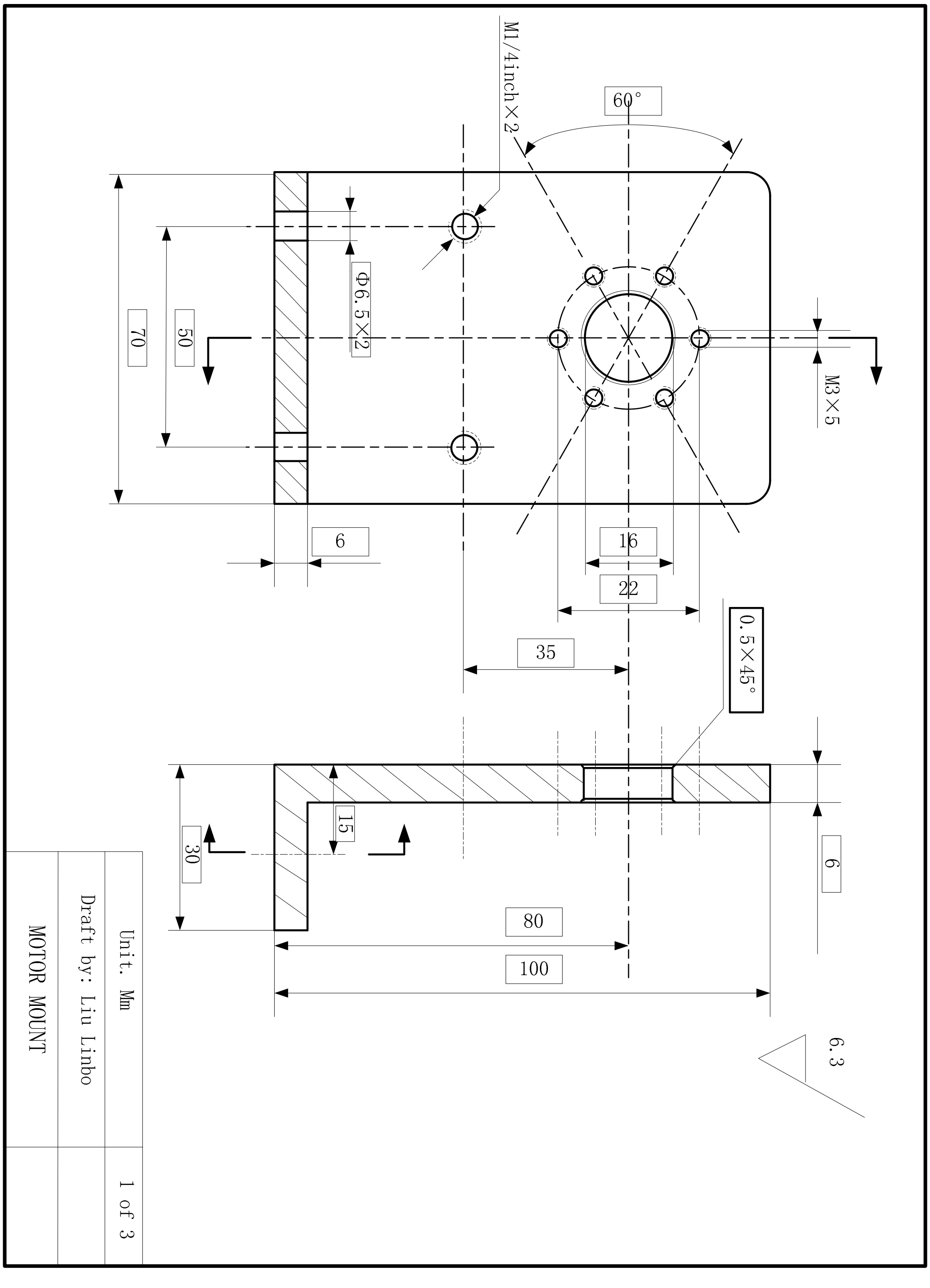

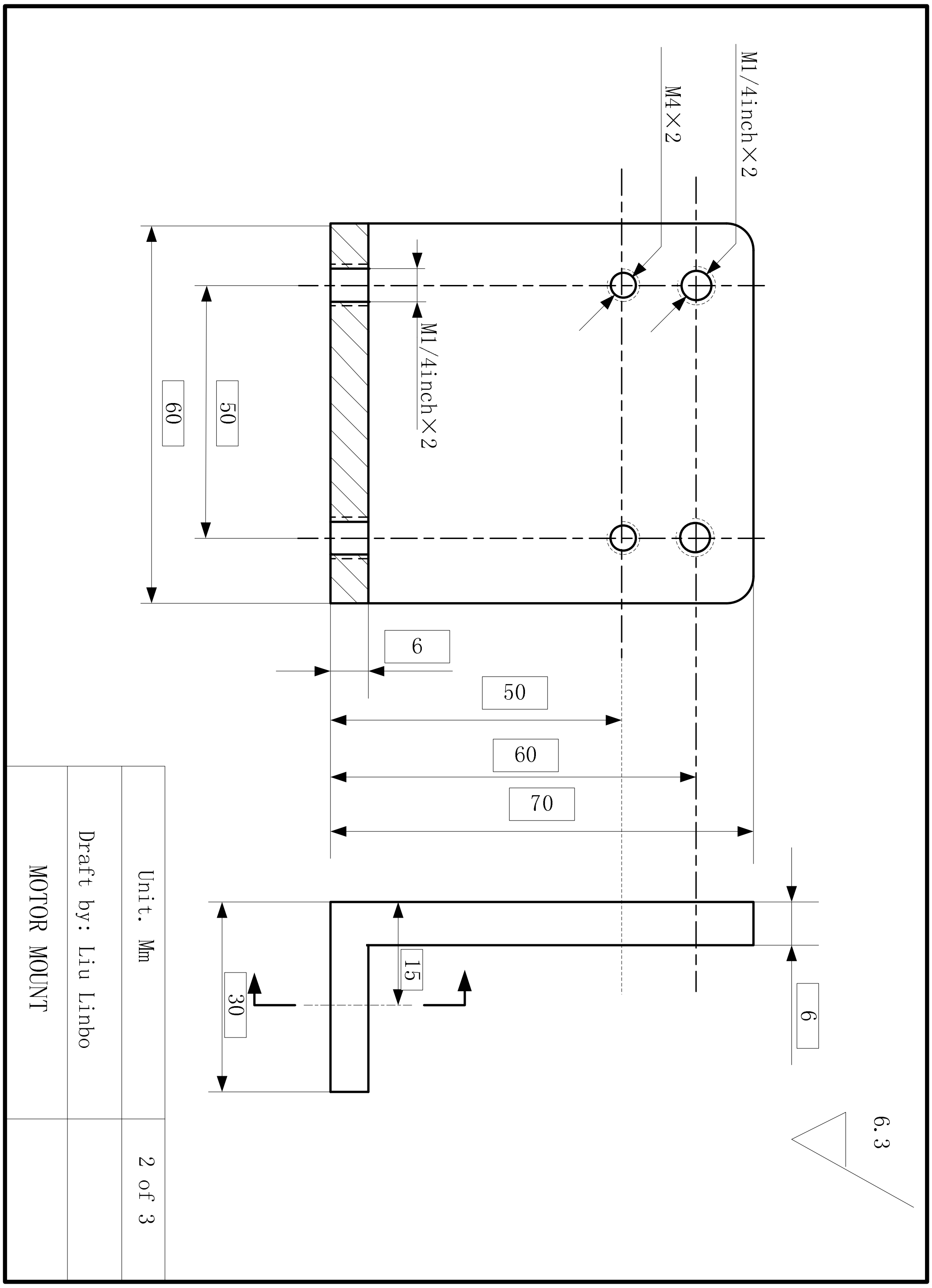
M1/4inch×2
M4×2
M1/4inch×2
60
50
6
50
60
70
15
30
6
6.3
Unit. Mm
Draft by: Liu Linbo
MOTOR MOUNT
2 of 3

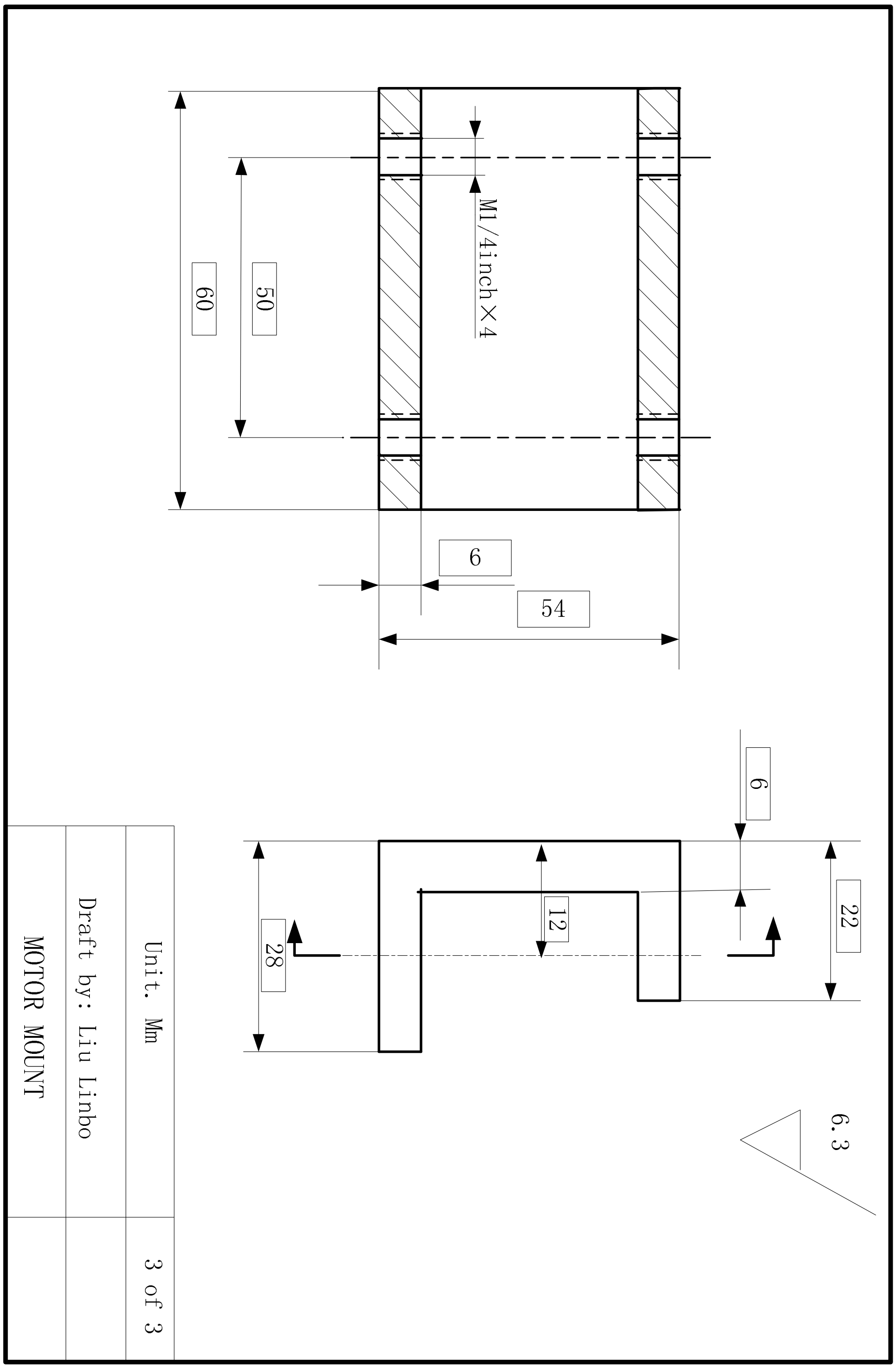
60
50
M1/4inch×4
6
54
6
22
12
28
6.3
Unit. Mm
3 of 3
Draft by: Liu Linbo
MOTOR MOUNT

# Appendix B: Drawings of DRPM based scanner

1. overview

2. base

3. mirror mount

4. scanner mounts

5. customized assembling tool for mirror positioning

6. assemble view

Overview

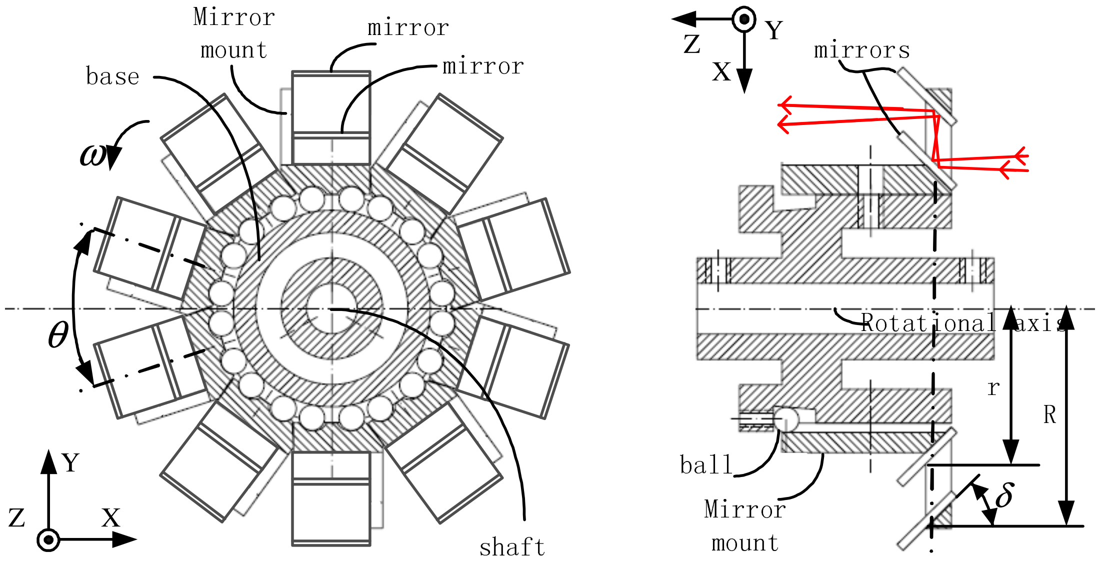

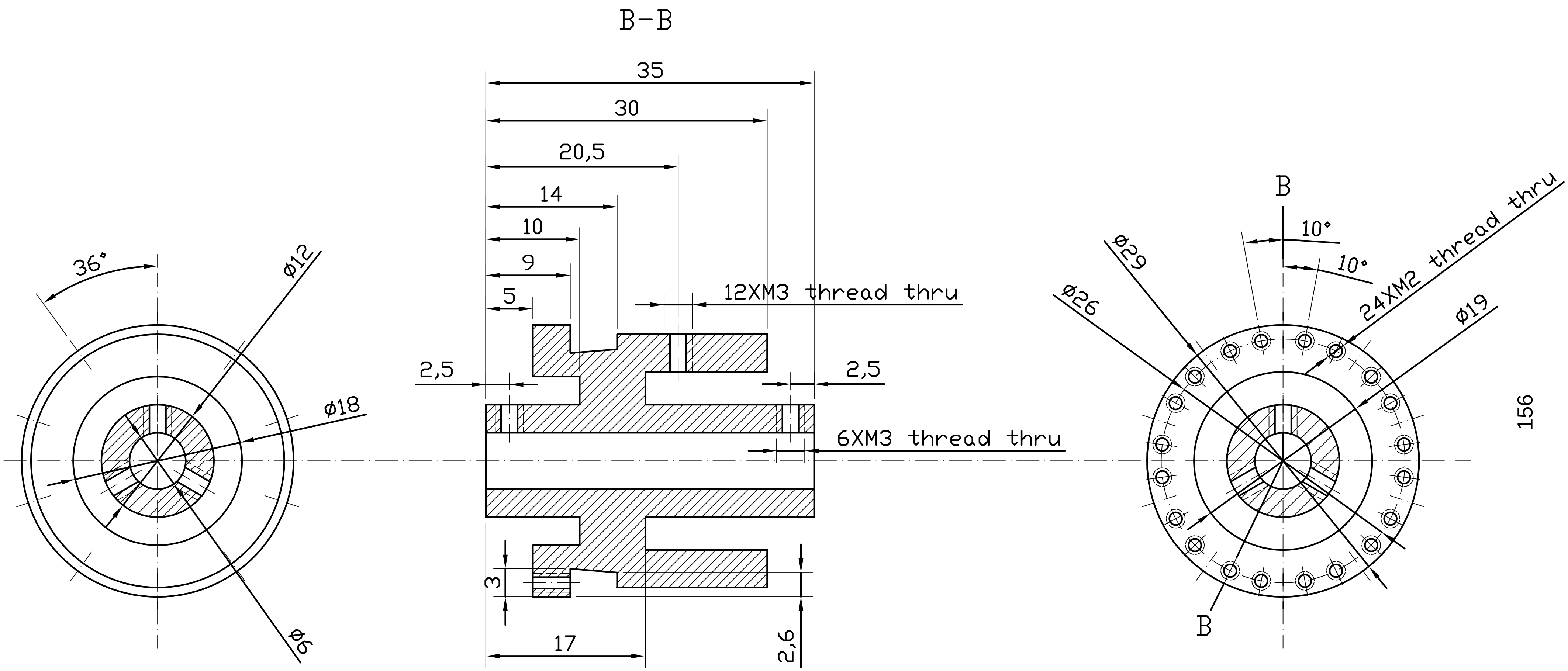

Material: AL alloy
Unit: mm

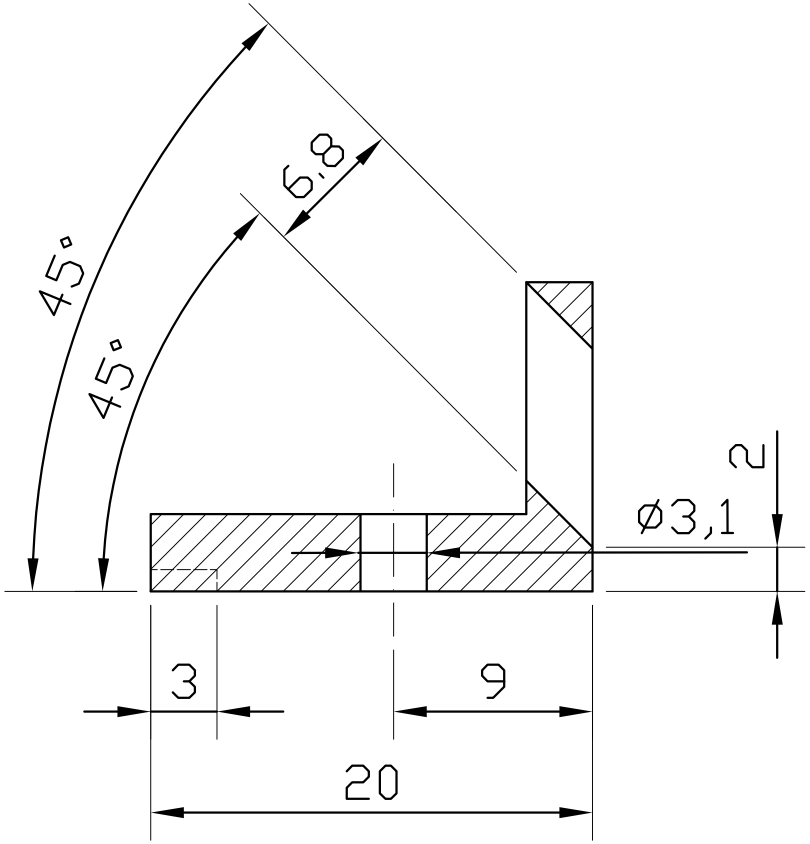

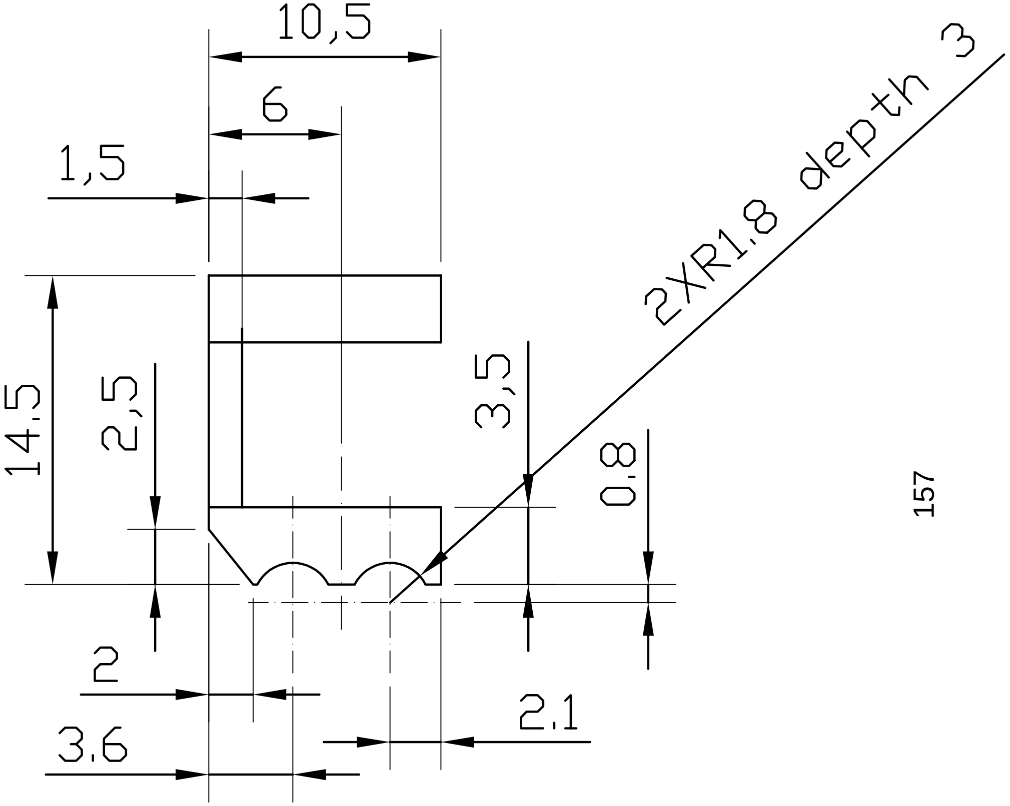

Material: AL alloy
Unit: mm

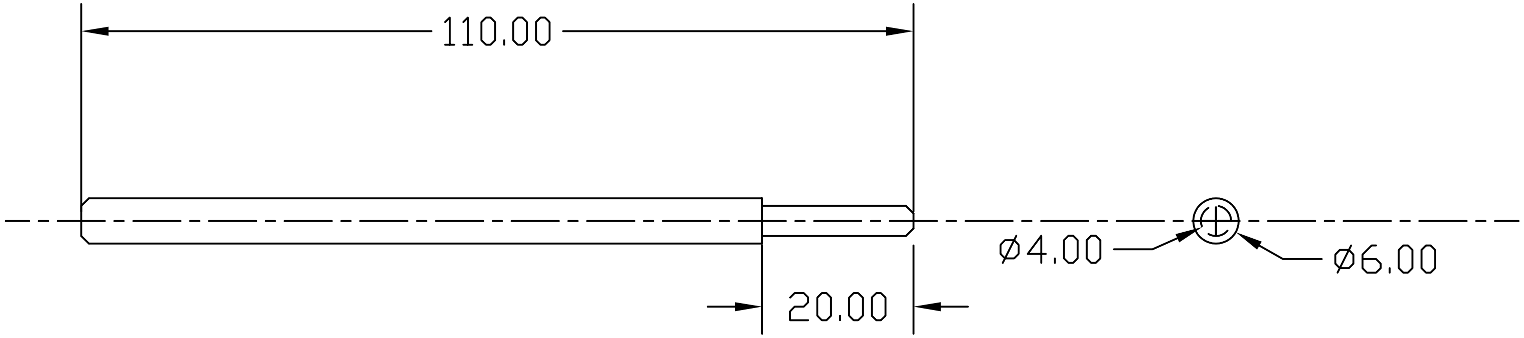

Material: stainless steel
QTY:2

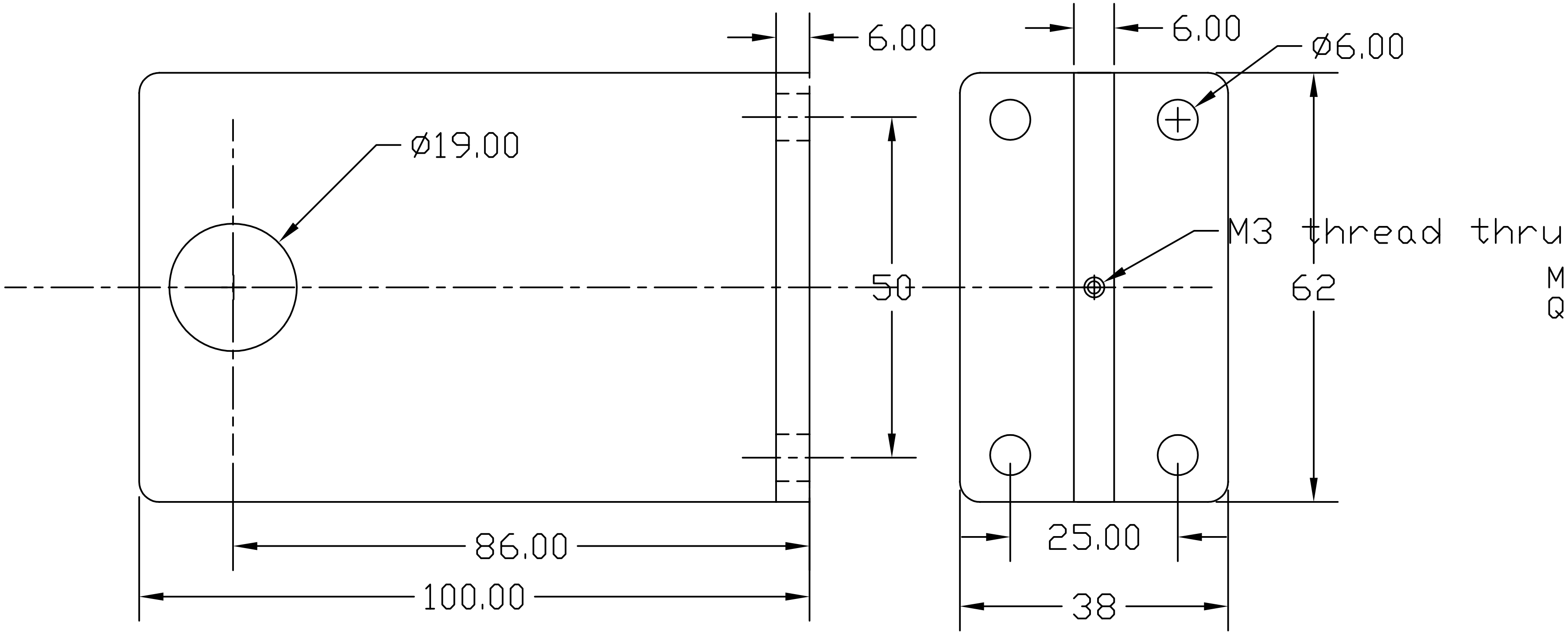

Material: AL alloy
QTY:2

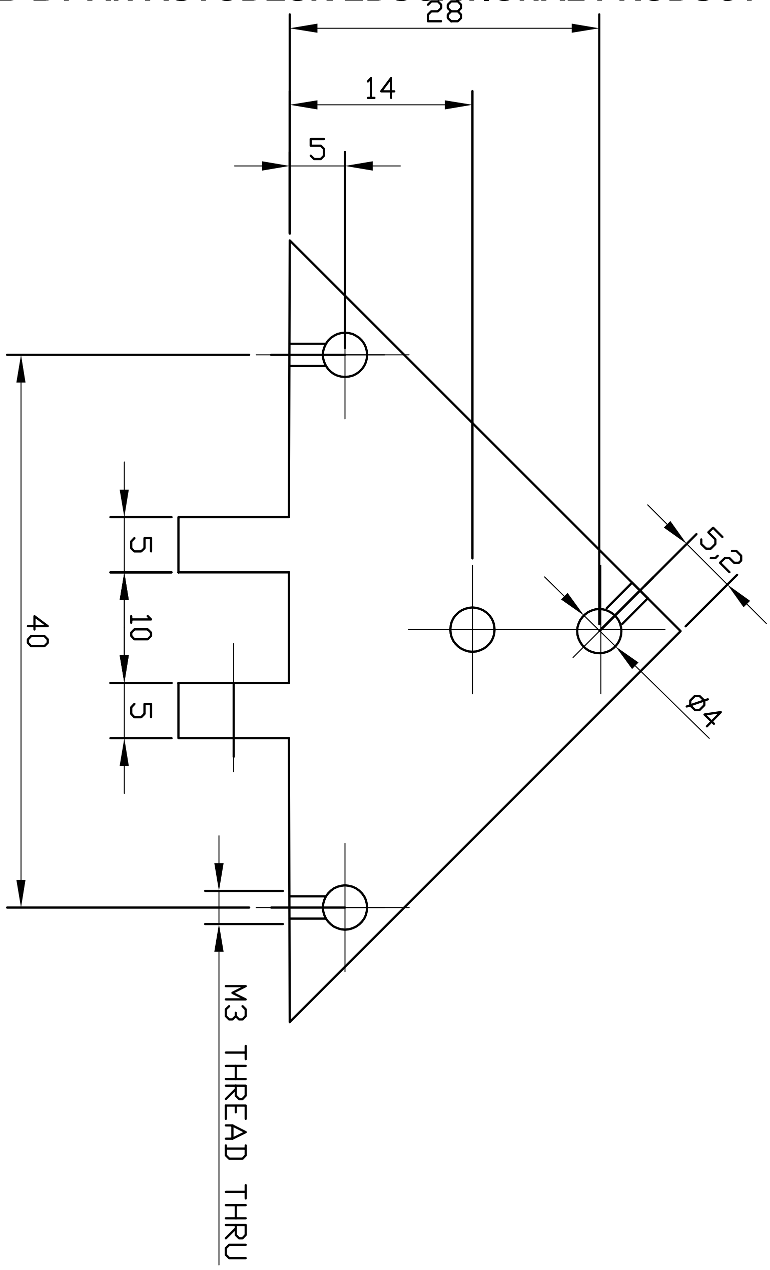

Material AL alloy
Unit mm

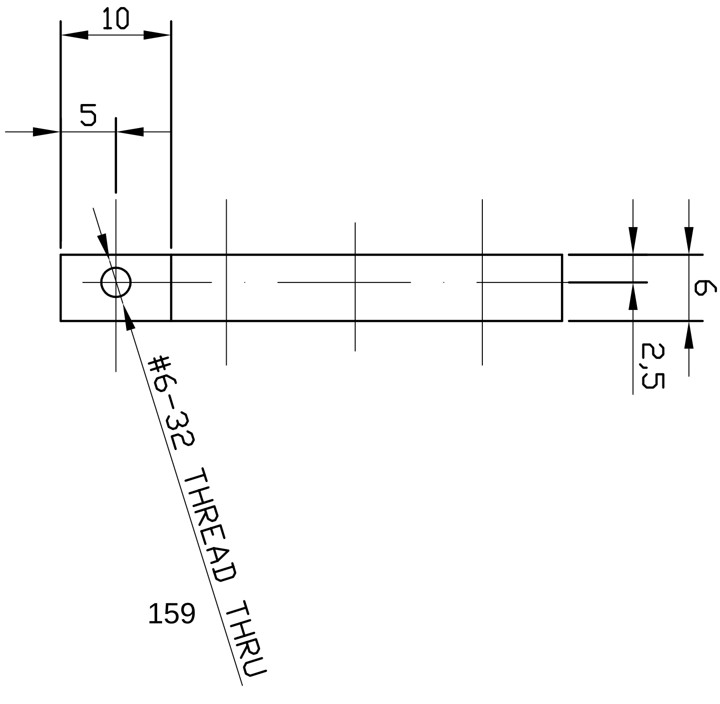

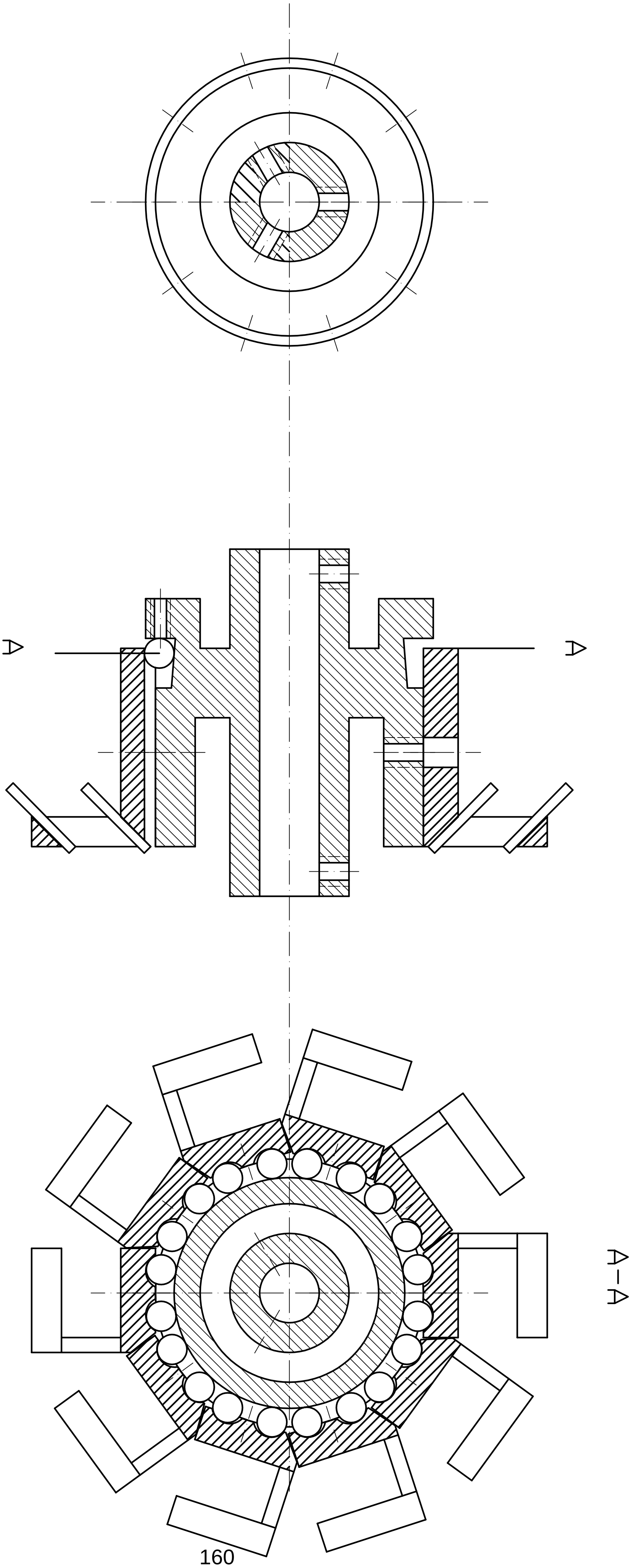
A
A
A–A